A LINEAR ALGEBRAIC BASED DIAGNOSIS METHOD FOR BROKEN ROTOR BARS OF LINE START PERMANENT MAGNET MOTORS

BY

Khalid I. Barad'ieh

A Thesis Presented to the
DEANSHIP OF GRADUATE STUDIES

KING FAHD UNIVERSITY OF PETROLEUM & MINERALS

DHAHRAN, SAUDI ARABIA

In Partial Fulfillment of the
Requirements for the Degree of

MASTER OF SCIENCE

In

ELECTRICAL ENGINEERING

DECEMBER 2016

KING FAHD UNIVERSITY OF PETROLEUM & MINERALS
DHAHRAN- 31261, SAUDI ARABIA
DEANSHIP OF GRADUATE STUDIES

This thesis, written by **KHALID IBRAHIM BARAD'IEH** under the direction his thesis advisor and approved by his thesis committee, has been presented and accepted by the Dean of Graduate Studies, in partial fulfillment of the requirements for the degree of **MASTER OF SCIENCE IN ELECTRICAL ENGINEERING.**

Thesis Committee

Dr. Ali A. Al-Shaikhi
Department Chairman

Dr. Zakariya M. Al-Hamouz
(Advisor)

Dr. Salam A. Zummo
Dean of Graduate Studies

Dr. Ibrahim M. El-Amin
(Member)

23/1/17
Date

Dr. Mohammad A. Abido
(Member)

Dedicated to my beloved Father, Mother, Brothers and Sisters

ACKNOWLEDGMENTS

My deepest gratitude to the majesty of ALLAH the most merciful, the most beneficent who gave me the ability and strength to begin and end my Master degree journey.

Acknowledgment also goes to King Fahd University of Petroleum and Minerals for the great opportunity to pursue my degree. I would like to express my sincere appreciation to my advisor **Prof. Zakariya Al-Hamouz** for giving me the opportunity of becoming one of his students. I thank him for the enormous amount of effort, time and support he gave me during the completion of my Master study and related research. His wide knowledge, continuous motivation, and immense helped me in all the time of writing my Thesis in its best form. To that generous and countless hours, in that office, where we met, discussed and accomplished the work. I say thank you. In addition to my advisor, I also would like thank my thesis committee: **Prof. Ibrahim El-Amin** and **Prof. Mohammad Abido**, for their insightful comments and encouragement, and also for the fruitful questions, which incented me to widen my research from various perspectives. My sincere thanks also goes to the LSPMSM group: Mr. Abdulaziz Milhem, **Mr. Luqman Maraaba** and **Mr. Ibrahim Hussein** and a special thanks to **Mr. Abdulaziz Milhem** for his valuable help and support in building FEM model of the LSPMSM. To my dear friends for their massive help and support until the completion of my Thesis. Finally, I would like to thank my father, mother, brothers and sisters who keep supporting me physically, mentally and spiritually during working on this Thesis and my life as well.

TABLE OF CONTENTS

LIST OF TABLES

LIST OF FIGURES

LIST OF ABBREVIATIONS

ANN	:	Artificial Neural Network
FEM	:	Finite Element Method
IM	:	Induction Motor
LSPMSM	:	Line Start Permanent Magnet Synchronous Motor
MCSA	:	Motor Current Signature Analysis
MFNN	:	Multi-layer Feed-forward Neural Network
PMSM	:	Permanent Magnet Synchronous Motor
QD	:	Quadrature and Direct axes
SVD	:	Singular Value Decomposition
WFA	:	Winding Function Approach

ABSTRACT

Full Name : [Khalid Ibrahim Sobh Barad'ieh]

Thesis Title : [A linear algebraic based diagnosis method for broken rotor bars of line start permanent magnet motors]

Major Field : [Electrical Engineering]

Date of Degree : [December 2016]

Line start permanent magnet synchronous motors (LSPMSMs) combine the high efficiency of the permanent magnet synchronous motors (PMSM) with the ease of use, simplicity in design and high starting capability of induction motors (IM). Due to the rapidly growing usage of this relatively new motor, studying its performance under fault conditions is necessary. In this thesis, the coupled magnetic circuit and winding function approach have been used to develop a mathematical model for LSPMSM under broken bar fault condition. This model takes into account the rotor asymmetry due to the broken bar fault in the *qd* reference frame. The effects of the broken bars fault on the rotor resistances and inductances have been evaluated. Motor's torque, rotor speed and stator current signatures of the LSPMSM have been captured using MATLAB/SIMULINK® for both healthy and faulty cases with different numbers of broken bars at different loading levels. Results have been verified by comparison with the JMAG® FEM model results, where high level of agreement has been obtained. In addition, this thesis presents an artificial neural network (ANN) method for detecting the broken rotor bar faults based on using singular value decomposition (SVD) extracted from the stator phase current. The accuracy of the proposed diagnostics algorithm reaches 96% when applied to stator current signals of the motor under unseen load and broken bar conditions.

ملخص الرسالة

الاسم الكامل: خالد إبراهيم صبح برادعيه

عنوان الرسالة: تصميم نظام خطي للكشف عن اعطال المحركات المتزامنة دائمة المغناطيسية الناجمة عن الكسور في قضبان قفص الجزء الدوار

التخصص: الهندسة الكهربائية

تاريخ الدرجة العلمية: ديسمبر 2016

تمتاز المحركات المتزامنة دائمة المغناطيسية بجمعها لمميزات المحركات المتزامنة دائمة المغناطيسية من ناحية كفاءتها العالية مع مميزات المحركات الحثية التي تمتاز بسهولة استخدامها وتصميمها وقدرتها العالية في مرحلة التشغيل. بسبب وجود تطور ملحوظ واهتمام كبير في هذا النوع من المحركات الجديدة نسبيا، تعتبر دراسة كفاءتها وتصرفها في حالة حدوث عطل ما ضرورة ملحة. عملت هذه الدراسة على الوصول الى نموذج او وصف رياضي للأعطال الناتجة عن الكسور في قضبان الجزء الدوار للمحركات المتزامنة دائمة المغناطيسية، هذا النموذج تم بناؤه بالاعتماد على مبدأ الدائرة المغناطيسية المترابطة ومفهوم اقتران الملفات، مع الأخذ بعين الاعتبار عدم التناسق الذي يحصل بسبب هذه الأعطال على تركيب المقاومات والملفات التي تكون الجزء الدوار. من أجل استعرض مخرجات النموذج الرياضي، تم استخدام برنامج المحاكاة MATLAB والذي تم من خلال اظهار نتائج التيار والعزم وسرعة الدوران لهذا المحرك في كلتا حالتيه الطبيعية وتحت تأثير الأعطال بأعداد مختلفة من القضبان المكسورة وباستخدام مجموعة من الأحمال.

من أجل التحقق من صحة نتائج النموذج الرياضي، تم استخدام برنامج المحاكاة JMAG والمبني على مبدأ الأجزاء المحدودة. باستخدام هذا البرنامج، تم بناء المحرك بطريقة رسومية والحصول على نتائج التيار والعزم والسرعة تحت ظروف مختلفة من الأعطال والأحمال، هذه النتائج تمت مقارنتها مع نتائج التمثيل الرياضي التي تم الحصول عليها باستخدام برنامج ال MATLAB . النتائج أظهرت بأن كلا التمثيلين الرياضي والرسومي على درجة كبيرة من التشابه والتناسق، وهذا يثبت صحة التمثيل الرياضي.

بالاعتماد على النظام الذي تم اقتراحه وتمثيله والتحقق منه، تم بناء نظام من أجل تتبع واستكشاف وجود أعطال القضبان المكسورة من خلال ملاحظة وجود تغيرات على تيار الجزء الثابت في المحرك يقوم على مبدأ الشبكات العصبية الصناعية . من أجل بناء هذا النظام، تمت محاكاة المحرك تحت مجموعة من الظروف من أجل الحصول على مصفوفة لتيارات الجزء الثابت، واخذ مجموعة القيم الفريدة لهذه التيارات واستخدامها كمدخلات من أجل تدريب الشبكة العصبية الصناعية.

CHAPTER ONE

INTRODUCTION

1.1 Background

Motors are the backbone of industry and manufacturing; tens of thousands of DC and AC motors are available in the industry. The AC class includes induction motors and synchronous motors, such as permanent magnet synchronous motors (PMSMs), as well as the recently introduced line start permanent magnet synchronous motors (LSPMSMs). Synchronous motors are characterized by their ability to control the reactive power in production as well as in consumption. They suffer from copper losses, thereby requiring additional magnetizing current on the rotor. For starting conditions, and to achieve the synchronous speed, this motor type needs to connect an additional motor (driver) to achieve the synchronous speed. Another way to obtain synchronism is to add permanent magnet (PM) materials. The importance of PM arises from the need to reduce the copper losses during current transfer from stator to rotor. However, some problems may arise, such as thermal, demagnetization and mechanical weakening problems, which decrease the reliability of this motor type [1]. On the other hand, PMSM is unable to start directly from a fixed frequency electrical source. Therefore, an additional electric circuit, such as inverters, is required to keep the motor running at synchronous speed, and to protect the motor from source transients, which will increase the losses.

To overcome the starting problems of the synchronous motors, induction motors (IMs) are used as an alternative. The rotor winding in induction motors can be squirrel-cage or wound-rotor type. The squirrel-cage rotor winding is composed of aluminum or copper bars embedded in the rotor slots and shorted at both ends by aluminum or copper end rings [2]. The wound-rotor winding has the same form as the stator winding, and the terminals of the rotor winding are connected to three slip rings. The squirrel-cage induction motor is simpler, more economical and more resilient than the wound-rotor induction motor [2]. However, this motor type is affected by higher copper losses than synchronous motors, and it needs additional current on the stator in order to cover these losses. This type of motors is characterized by its high efficiency, since it replaces the magnetizing materials by lower-loss materials, which increases its cost.

A new design of electric motors with high efficiency, high power factor and high starting capability called "Line Start Permanent Magnet Synchronous Motor (LSPMSM)" is newly developed as a replacement for the induction motors. The motor name is derived from its ability to start directly when connected to the source. It has a squirrel cage winding to develop the starting torque that pulls the motor to the synchronism and a permanent magnets for the generation of synchronous torque at steady state, thus combining the high efficiency of the PMSM with the ease of use, simplicity in design and high starting capability of the induction motors [3]. On the other hand, LSPMSM has a poor starting torque because of the opposite (braking) torque caused by the PMs, which decreases the resultant torque in the startup [4, 5]. The challenge in the LSPMSM design stems from the need to rapidly convert from high starting speed of the induction motors to the synchronous speed of the PM motors, which requires a limited load inertia and high torque-speed

characteristics at startup. The efficiency of this motor type may reach 94% for the 15 KW motor version [6].

1.2 Thesis Motivations

Motors are ubiquitous in everyday life and have wide ranging applications, such as industrial, commercial and residential utilization. Statistics indicate that electrical motors account for about two-thirds of the total industrial power consumption in each society [1]. Most of the developing countries moved from rural living and reliance on agriculture to industrialization; therefore, demand for more efficient and robust electrical motors is a challenge.

Because of the unlimited number of electric motor applications, there are over 700 million motors of various sizes in operation across the world [1]. Induction motors constitute by far the largest portion of electrical motors in the market. However, motors that are more efficient began to appear as an alternative. In the last few years, "Line Start Permanent Magnet Synchronous Motor (LSPMSM)" emerged as a powerful candidate in the motor industry, and has been promoted for industrial, commercial and residential applications. This motor has many desirable features that will likely expand its market size. In addition, LSPMSM is expected to replace the currently utilized motors, such as induction motors. In terms of efficiency, this motor achieves a much higher efficiency than the induction motor for the same power rating. Induction motors suffer from lower power factor due to their inductive behavior, which is proportional to the motor losses. As LSPMSM operates with a higher power factor than the induction motor, this will increase the efficiency and reduce

the total loss in terms of the power and cost, especially for higher-rated motors. Regarding the motor operations, it is well known that the AC motors are susceptible to many faults types. Motor failures may result in catastrophic events, including production shutdowns. Such shutdowns are costly in terms of lost production time, maintenance costs and wasted of the raw materials.

For these reasons, studying the LSPMSM and finding a reliable diagnostic and monitoring tool under faulty conditions, such as broken bars, is needed. As the first step in building a diagnostic tool, an accurate mathematical model for the motor must be developed. As modelling of the LSPMSM under broken bar fault conditions has not been attempted, thus far, this is the goal of the present study.

1.3 Thesis Objectives

The main objective of this thesis is to develop a mathematical representation of the LSPMSM, including the effect of broken rotor bars fault based on magnetic circuit theory and Winding Function approach (WFA) and verifying this model using the FEM method. MATLAB/SIMULINK® software will be used to simulate the performance of the proposed mathematical model. The results of the proposed mathematical model will be verified using JMAG® software. Moreover, a diagnosis technique based on Artificial Neural Network (ANN) will be developed to detect the broken bars fault in LSPMSM using Singular Value Decomposition (SVD) based linear algebraic method to extract a distinguishing features from the stator phase current. This distinguishing attributes are proposed to be the inputs of the built neural network. These objectives can be summarized as follows:

Objective 1: Conducting a comprehensive literature review focusing on the performance of LSPMSM in addition to the failures and diagnostics techniques associated with different types of motors with focus on LSPMSM.

Objective 2: Deriving a mathematical representation under the healthy and faulty with broken bars LSPMSM.

Objective 3: Building a MATLAB/SIMULINK® model to investigate the performance of LSPMSM under different loading levels for both healthy and faulty with different number of broken bars.

Objective 4: Verifying the MATLAB/SIMULINK® model results using a commercial FEM software namely JMAG®.

Objective 5: Designing a monitoring and diagnostic tool based artificial neural network to detect the broken bars fault in LSPMSM.

1.4 Thesis Organization

In addition to the introduction, this thesis has five chapters. Chapter Two contains a comprehensive literature review describing LSPMSM, its design and the reported analysis methods. In addition, the broken bar fault modelling and monitoring in LSPMSM and other AC machine types will be explored. In Chapter Three, the proposed mathematical modelling of the LSPMSM will be presented and simulated, along with the governing equations used for mathematical modelling. The proposed mathematical model will be verified in Chapter Four by a FEM modelling using JMAG® software program. Once the stator current is acquired, a developed broken bar diagnostic tool based on the artificial

neural network approach will be introduced in Chapter Five. Finally, conclusions and suggestions for future works are given in Chapter Six. The proposed work flowchart is shown in Figure 1.1.

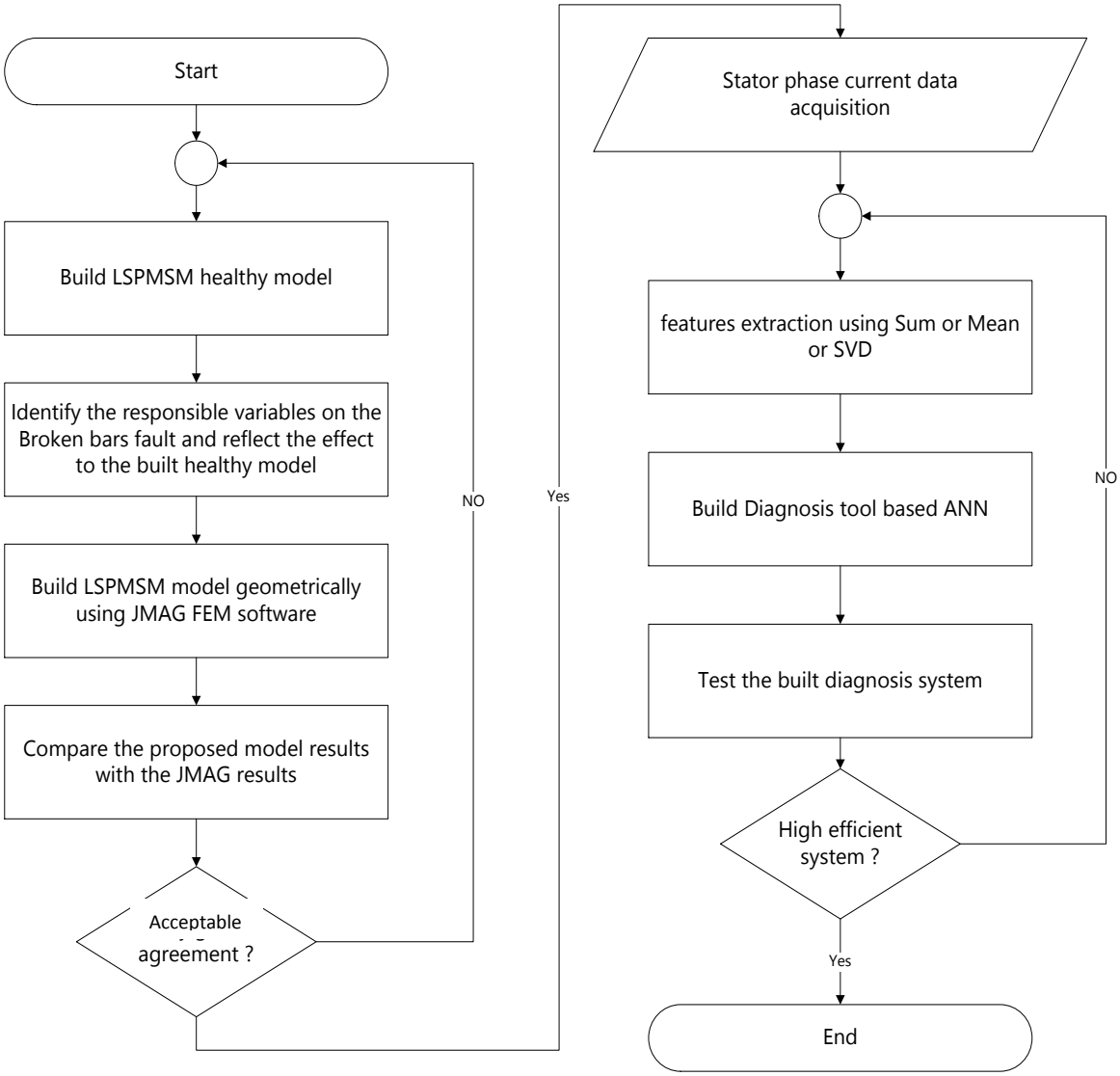

Figure 1.1: Description of the proposed work

CHAPTER TWO

LITERATURE REVIEW

In this chapter, an overview of the existing literature on the LSPMSM will be presented. This chapter has five sections. In the first one, the commonly used approaches in AC motor modelling will be presented. Followed by the general AC motor faults in section Two. A theoretical overview about the LSPMSM design and different proposed rotor topologies will be presented in sections Three and Four, respectively. The Fifth and Sixth sections are designated for a review of the existing studies related to the performance analysis and behavior of this motor in transient and steady state, respectively. Finally, a conclusion and contribution of this work will be delineated in the Seventh section.

2.1 Commonly used approaches in AC motor modelling

Modelling is a representation of the theory that can be used for prediction and control of a motor. To be useful, a model must be realistic, simple to understand and easy to manipulate. Modelling here refers to the process of analysis and synthesis aimed at providing a suitable mathematical description that encompasses the relevant dynamic characteristics of the LSPMSM, preferably in terms of parameters that can be easily determined in practice. However, different techniques can be used in AC machine modelling, which can be classified into three groups discussed in the following subsections.

2.1.1 Two axes referance frame model

In the study of AC motors, mathematical transformations are often used to decouple variables, to facilitate the solution of difficult equations with time-varying coefficients or to relate all variables to a common reference frame. However, three-phase to two-phase transformation can be used to decouple the *abc* variables of the stator phases. Such transformation is called "Park's transformation." Another transformation type, known as "Poly-phase to two-phase transformation," is the generalization of Park's transformation. This transformation can be used to decouple the *abc* variables of the rotor equations in the case of the poly-phase rotor distribution [7]. However, all variables should be related to a common reference frame. In the present study, the rotor quantities are related to the stator.

2.1.2 Equivalent circuit mathematical model

Equivalent circuit modelling of the AC machines, which is known as a "coupled circuit approach" is necessary for facilitating real-time simulations. Modelling process begins with identifying the purpose of the model and its constraints, as well as the kinds of simplifying assumptions or omissions that can be made, along with defining the available computational facilities. However, this method is less time consuming and yields satisfactory accuracy if compared with other techniques such as the Finite Element Method (FEM).

2.1.3 Finite Element Method (FEM)

FEM is a powerful numerical technique used to find approximate solutions for partial differential equations or boundary value problems based on dividing a large problem into simple problems called "finite elements." The use of a FEM is helpful in the design of AC machines. The available FEM software is relatively easy to use because of its ability to

import machine's geometry from the external CAD programs. In addition, FEM software has become automated to the point of being useful in modern machine design. It also offers flexibility in the machine geometry, boundary conditions and material properties. In order to model AC machines using FEM, Maxwell's equations should be formulated in terms of magnetic vector potentials and then solved based on boundary conditions. Unfortunately, as this approach is extremely time consuming, it is not suitable for real-time simulations. Usually, FEM is used to verify the developed mathematical models. Thus, a JMAG® based FEM software was used in the present study to verify the proposed LSPMSM mathematical model.

2.2 AC motor faults

In this section, a short summary of the most common failures that might occur in the AC motors, their causes and their effects will be discussed. In addition, the most common fault diagnosis techniques will be presented.

2.2.1 General AC motor faults

Different electrical and mechanical faults in electric motors can be classified into five types:

- **Stator winding faults:** Failures on the stator might be caused by environmental stress, as well as thermal or mechanical issues. Thermal stress causes ultimate failure and insulation degradation. Copper losses are the main source of thermal faults in electric motors; this high temperature leads to chemical reactions, which

causes damage in the insulation materials, since the conductor expansion occurs at a higher rate than in the insulations [8, 9]. Winding failures caused by electrical stress can take many forms, such as voltage transients, dielectric and corona. Mechanical stress caused by bearing failures may result in coil movement, rotor drumstick in the stator, electromagnetic vibration, temperature variations, misalignment between rotor and stator, and deflection of the shaft. Environmental stress is typically caused by oil contamination or cooling system leakage. Different types of detection and diagnostics for stator winding failures have been reported in extant literature, such as using a magnetic field, angular speed noise, air-gap torque, vibration, gas analysis, partial discharge, and motor current signature analysis (MCSA) [10].

- **Rotor Bar faults:** Failures on the rotor include broken rotor bars and end-ring faults. Broken bars shown in Figure 2.1 can be classified into two types—cast and fabricated rotor—depending on the rotor type. The cast rotor is harsher than fabricated. In general, the faults that occur on the cast rotor bars cannot be repaired.

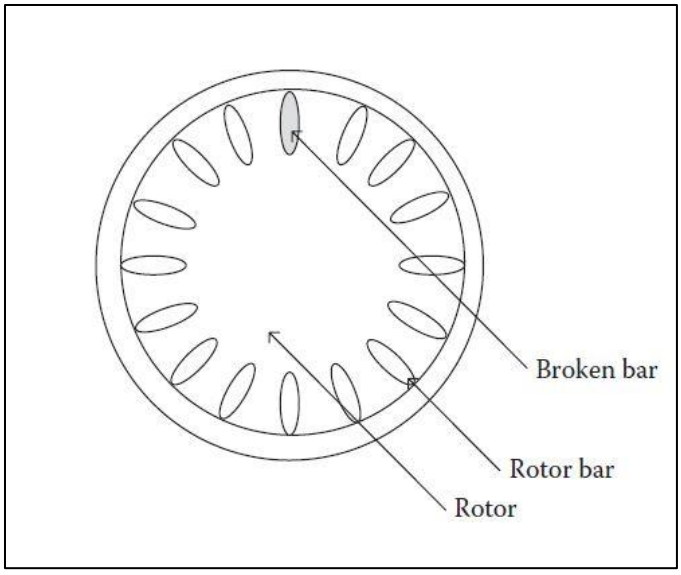

Figure 2.1: One Broken Bar in LSPMSM [11]

The common causes of rotor bar and end-ring breakage are summarized in Table 2.1. More details about this fault types will be presented in the next subsection.

Table 2.1: Causes and effects leading to the broken rotor bars and end rings faults

No.	Reason	Effect
1	Thermal stress	Imbalance, excessive losses, hot spots and sparking
2	Magnetic stress	Imbalance, magnetic pull, electromagnetic forces, vibration and electromagnetic noise
3	Dynamic stress	Cyclic stress, centrifugal forces and shaft torques
4	Residual stress	Issues induced in the manufacturing process
5	Environmental stress	Contamination on the rotor material due to some chemical reactions
6	Mechanical stress	Bearing failures and loss of lamination parts

- **Eccentricity related faults:** Airgap eccentricity fault occurs when the motor has a non-uniform airgap between the rotor and stator. This fault leads to some changes in the magnetic flux, resulting in changes in the motor inductances. Eccentricity can be classified into static and dynamic eccentricity. Static eccentricity occurs

when the shaft is in the center point of the stator. In this case, the air-gap will not change by the passage of time, as shown in Figure 2.2. Dynamic eccentricity occurs when the centerline of the shaft is located at a variable offset from the stator, and as the rotor rotates, the air-gap distance varies, as shown in Figure 2.3 [12].

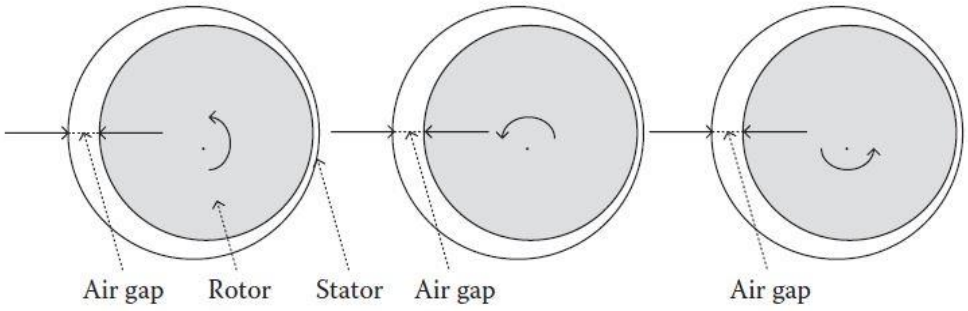

Figure 2.2: Static eccentricity

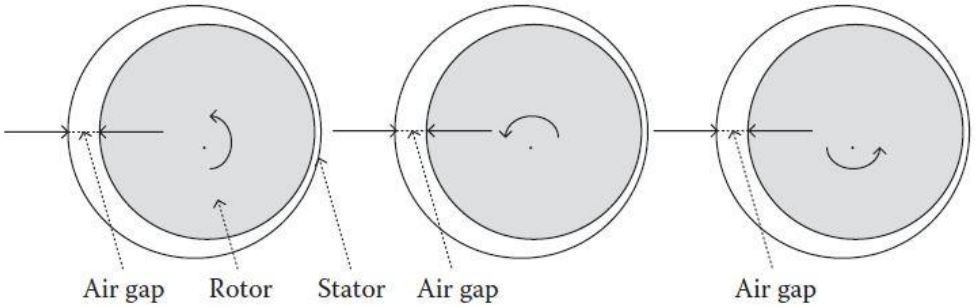

Figure 2.3: Dynamic eccentricity

Figure 2.4 shows some statistics of the most common faults in electrical motors.

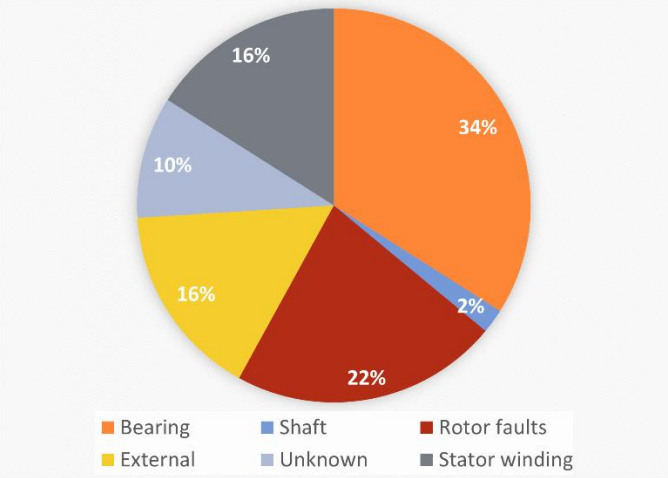

Figure 2.4: Statistics of the most common motor failures [12]

Each one of the aforementioned faults produces a particular manifestation during the operation of the motor, such as:

- Un-balancing in the airgap voltage or line current.
- Excessive noise.
- Increase in temperature.
- Growing losses and reduction in the motor efficiency.
- Decline in the average torque.

Identifying these side-effects allows distinguishing between different faults, as the key point in fault diagnosis is to determine the reliable signal source. These signals can be obtained via:

- Motor current signature analysis (MCSA).
- Electromagnetic field/flux analysis.

- Motor temperature measurements.
- Recognition using infrared technology.
- Monitoring of radio frequency emissions.
- Monitoring of the noise and vibration.
- Chemical analysis.

2.2.2 Squirrel-cage bars in electrical machine and its failure

Squirrel-cage bars in electrical machines produce adequate high starting torque when the motor runs from standstill [13]. Similar to asynchronous motors, squirrel-cage bars in LSPMSM develop the startup torque during motor run-up by enabling the rotor to have direct-on-line movement. When the load situation is unbalanced or the rotation speed is fluctuated, an important function of squirrel-cage bars is to reduce the counter-rotating fields of the air gap, which otherwise would lead to significant losses [14]. In the squirrel-cage electrical machine, two different types of squirrel-cage rotor bars are manufactured, named die-cast and fabricated. Die-cast cage rotors are used in low power rating motors, while fabricated cages are used for higher power ratings and special applications. Anyway, failures can happen in both types. In die-cast rotors, generally made from aluminum, broken bars are usually caused by porosity. Porosity is introduced to the cage when the molten aluminum is cooled and causes shrinkage of the bar surface. This condition can be aggravated by leakage of the molten aluminum between laminations or by insufficient injection of aluminum. Generally, porosity is not considered seriously in terms of reliability, because it is not likely to generate secondary damages in the motor [15]. In the fabricated rotor, made of copper, broken bar is usually caused by projection or arcing of the bar or by miss connection between end ring and bars.

Breakage of the rotor bars is usually the main serious failure in the squirrel cage motors, because it progressively increase different stresses and also brings about secondary failures in machine. These failures will also reduce the motor efficiency, threaten its safe operation, shorten its lifetime and thus increase the operational cost. Broken rotor bar generates unbalanced currents and torque pulsation, and as a result reduce the developed torque and increase the speed fluctuations of the motor [16]. Changes in the rotor current distribution due to bar breakage progressively deteriorates the condition of the neighboring bars. For instance, once a bar breaks, the current in the neighboring bars increases up to 50% of rated current and overheat them [17, 18]. The overheated bars are arcing and causing the rotor bend over that result an eccentricity, which causes basic rotor unbalance and a greater unbalanced magnetic pull [19]. Broken rotor bar also may cause a shaft vibration that results failures in bearing and eccentricity in the air gap [20]. In addition, the extra heat also can demagnetize the permanent magnets [21]. During operation of the motor, the broken rotor bar may rise out itself, or broken pieces of the rotor bar may exit the slot due to the centrifugal force and damage the stator windings or laminations [22].

On the other hand, the broken bar fault affects the rotor magneto-motive force (MMF) and consequently the stator current. The MMF of the rotor can be resolved into the forward component corresponding to the healthy case, which rotates at synchronous speed. However, when a rotor bar cracks, no current can flow through the bar and hence no magnetic flux is generated around that bar. In case there is no magnetic flux around a bar, a non-zero backward rotating field and thus an asymmetry in the rotor MMF is produced. It has to be noted that for a symmetrical rotor with no broken bar, the resultant of backward rotating field is zero. This non-zero backward MMF due to broken bar rotates at slip

frequency and induces harmonic currents in the stator windings, which are superimposed on the stator winding currents [23].

2.2.3 Fault Diagnstics and monitoring techniques in electric motors

Motors often operate in hostile environments, such as corrosive and dusty places. They are also exposed to a variety of undesirable conditions and situations. These unwanted conditions can cause the motor to experience failure, which may result in an unserviceable condition of the motor, if failure is not detected early. Therefore, early detection of the incipient motor fault is of great concern and has been the subject of extensive research. Monitoring of the motor faults allows assessing the motor health by analyzing the data collected from the running motor. Accurate monitoring and diagnosis of the motor signals results in reduction in the downtime and increased motor efficiency.

A wide range of techniques are presently used in failure monitoring and detection. Such techniques are usually classified via one of the following strategies [24]:

- Techniques based on signal processing, including noise analysis, infrared analysis, gas analysis and motor current signature analysis (MCSA) in time or in frequency domain.
- Techniques based on modelling, including neural network, fuzzy logic, genetic algorithm, finite element circuits and artificial intelligent.
- Techniques based on machine theory, including winding function approach, modified winding function approach, and magnetic equivalent circuit.

However, Fault diagnosis usually involves the following three steps:

- Detection step; aimed at identifying the wrong behavior of the system and fault causes.
- Isolation step; aimed at determining the characteristics of different faults, i.e. the fault type.
- Analysis step; designed for analyzing the coming data obtained in the previous two steps and aimed at determining the cause of the fault, fault size and its effect on the overall system.

A good diagnostic technique will allow a fault to be diagnosed quickly, with the minimum amount of collected data.

However, the squirrel-cage bars are only working in transient condition in the LSPMSM and in both transient and steady state conditions in induction motor. The frequency domain methods are not suitable for this aspect. This is because the features related to broken rotor bar fault which are conserved in the back rotating fields mentioned in the section 1.3.2 are cyclically repeated at a rate equal to twice the slip frequency (2sf) on the three phase stator current. Therefore, the stator current harmonics are changing from the fundamental frequency to zero and again to the fundamental frequency in LSPMSM. Squirrel-cage bars in LSPMSM develop the startup performance during motor run up by enabling the rotor to have direct on-line movement. In addition, at steady state, there is no current flow in the cage and the amplitude of the backward harmonic become zero. [17, 18] Accordingly, a Neural Network based diagnosis method-using MCSA in time domain and benefits from the stator starting current will be used in this research work.

2.3 LSPMSM design - Theoretical background

The first design of the LSPMSM was proposed in 1955 by F.W. Merrill [25], with the permanent magnets made of alnico and ferrites. Alnico suffered from low coercivity, i.e., it took a long time to magnetize and demagnetize, in addition to its stability requirements at low temperatures. On the other hand, ferrites suffered from low remanence. Because of these issues, this model failed to conserve its magnetization, which was the main obstacle to converting this model into an industrial product.

The works that followed typically focused on enhancing the behavior of the Merrill model until early 1980s. This was the turning point, as a high-performance earth magnet material was developed, referred to as "the neodymium iron boron (NdFeB)." This advancement allowed designing models with good performance and high efficiency. Therefore, the interest in LSPMSM was boosted again, resulting in many valuable papers being published in this field between the 1980s and 1990s. Such studies tended to focus primarily on the steady-state performance of the motor, as the researchers were interested in increasing the motor efficiency. Other studies incorporated the transient analysis of the LSPMSM based on *qd*-model analysis. Finite Element Method (FEM) and parameters estimation methods were also used in the late of 1990s to study the starting and synchronization performance of the LSPMSM. In the last 20 years, interest in LSPMSM increased, both in the industry and in academia. These trends have prompted the introduction of international regulations to specify the minimum acceptable requirements of the motor accuracy and energy, such as energy policy introduced in 1992, 1997 and 2008 in United States, Canada, and the European Union, respectively [26].

2.4 Rotor design and topologies

As previously mentioned, Merrill [25] developed the first design of the LSPMSM, where the design performance was comparable with the induction motor performance. Rotor configuration under different operating conditions is shown in Figure 2.5. Where A is the flux distribution on air-exposed rotor, B is the flux distribution in the open circuit, C is the flux distribution on rated voltage and no load, and D is the flux distribution under raised voltage and no load.

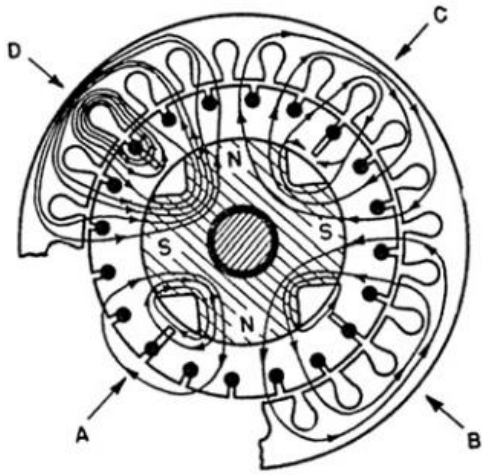

Figure 2.5: Rotor design of the first LSPMSM by Merrill

However, this design did not address the reluctance torque components, and because of the used alnico magnet material, it was unable to conserve the magnet's power for a long time, according to Douglas [26]. Douglas derived the current position of Merrill's design using reactance theory and identified the requirements for improving magnet materials in order to enhance the motor performance. Adkins and Cahill [27] based their study on Douglas's work and were successful in building a 0.5 hp, 2-pole LSPMSM based on Merrill's

guidelines. Because of the lower value of the air-gap flux density, these researchers found that the rated torque of this motor was lower than the IM for the same motor size. In addition, they reported that this motor had a lower power factor than IM. Moreover, they concluded that, for this motor type with interior permanent magnets, the magnet thickness should be greater than the air-gap for the *d-axis* magnetic flux, and the *q-axis* magnetic flux should pass the pole faces without crossing the magnets. This resulted in the *d-axis* stator inductances being lower than the *q-axis* inductances.

Volkrodt [28] proposed multiple geometries for the rotor. However, as his work was conducted in Siemens, these designs have either his name or are credited to Siemens. Each layer of the rotor lamination is made of three pieces of oriented iron-silicon (Fe-Si) sheets, ordered to specify the position of the four magnets and gaps for non-magnetic material, including a shaft, which was also non-magnetic. The rotor bars are combined together by a cast aluminum cage to make an integral rotor structure, since the rotor is made of discrete slices, as mentioned previously.

In addition, simple calculation procedures for evaluating motor parameters were proposed by Chalmers *et al.* [29] as a replacement for numerical methods like FEM in studying the high field PMSM by defining the two-axis theory. Rodger [30] proposed a double LSPMSM rotor design, i.e., two-part rotor mounted on the same shaft. One part was fixed around the shaft, while the other part rotated around the shaft by means of a centrifugal concept. Around 30% of the rotor losses were reduced relative to the same size IM, and its efficiency was 93%.

In 1980, Hitachi® Company developed the highest speed PMSM [31] with the rated output power of 1 KW, and 12,000 rpm rated speed. Magnetic circuit approach was used to calculate reactance, in addition to using FEM to calculate the magnetic fields.

Many rotor topologies and designs have also been developed by researchers in the US, Japan and China between 1985 and 2004. These studies aimed at enhancing the magnet characteristics and distribution on the rotor core in order to attain the highest performance, as summarized in Table 2.2.

Table 2.2: Summary of the most important LSPMSM rotor topologies between 1985 and 2004

No.	Year	Researcher	Proposed design
1	1985	Ishizaki *et. al.* [32]	Interior type PMSM using ferrite magnets located inside the rotor for 0.75 KW, 4-pole motor
2	1980s	Reneyuan [33]	Proposed three rotor configurations for three different applications (fan, oil pump and spindle drive), which were analyzed using FEM to study the starting characteristics of each application
3	1999	Knight and Salmon [34]	Studied the dynamic behavior of the single-phase, 2-pole LSPMSM for different rotor topologies. According to the study findings, the analysis of a single-phase rotor is more complex than that of the 3-phase, because of the appearance of backward rotating fields in the stator for the 1-phase motors
4	2000	Knight and McClay [35]	Developed a new LSPMSM design by optimizing the rotor and stator slots. The motor efficiency has been increased by 4%.
5	2004	Rahman and Kurihara [36]	Proposed a new configuration of the interior magnets on the rotor, taking into consideration a load with high inertia.

6	2011	Peralta *et al.* [37]	Presented a steady-state analysis of a special purpose, cylindrical structure canned LSPMSM used in chemical applications. This motor had separate rotor and stator. The PM was surface mounted type. This motor was tested at full load, and it gave an enhanced performance.
7	2011-2012	Beak *et al*. [38]	One-phase LSPMSM has been proposed based on indenting the minimum copper losses and magnetic balance, in addition to increasing the maximum torque and enhanced output torque.
8	2009 2011 2012	Isfahani [39] Marcic [40] Rahman *et al.* [41]	A comprehensive review of 98 extant studies on the LSPMSM and its development in the last 25 years. A detailed comparison between the enhancement methods used for LSPMSMs has been reported.
9	2013	Mirsalim and others [42]	A pole-changing technique was used in order to enhance the motor performance in starting and steady-state. In addition, motor synchronization capabilities were improved using a slotted-solid rotor, which improved the distribution of the magnetic flux.

To date, approximately 10−12 rotor geometries have been developed. Each design aimed to enhance the motor efficiency and power density by reducing the armature reaction or by enhancing the flux distribution. It can be noted that there is no proposed model included the asymmetry that may happened on the motor structure due to different faults such as broken rotor bars; which is the goal of the present study.

2.5 Performance Analysis of the LSPMSM

Steady state analysis of LSPMSM started in the 1980s. Honsinger [43] studied the steady-state performance of the LSPMSM in 1980 by two methods, one of which was the phasor

diagram including core losses, which was used for the first time in that study. The other method was based on the whole machine admittance calculation, which was adjusted to include the core losses. The reactance values were recalculated to include the effect of the magnetizing and demagnetizing reaction because of the PMs on the motor armature. In these two methods, the behavior of the current with the torque angle was also assessed. This approach later became the standard for measuring the synchronous performance and is still used for most of the commercial motors.

Wong and Binns [44] analyzed a 4-pole LSPMSM, attempting to adjust a number of parameters to reduce the cost of the magnet materials. In this work, 2-D and 3-D FEM analysis methods were used with non-linear magnetic circuit representation to analyze the magnetic field of the motor. As the rotor configuration was asymmetric about the rotation axis, there was a difference in motor performance in the two rotation directions. One direction gave a high leading pf, which was 0.994 with 86% performance, while the other gave a high lagging pf, which was 0.96 with 84% performance.

Chalmers *et al*. [45] studied the performance of LSPMSM under variable frequency source. The motor was presented using two axes phasor representation. The results were tested experimentally on a 3-phase, 4-pole, star connected PMSM with SmCo5 ferrite magnets. In addition, McClay and Knight [46] conducted a steady-state and dynamic FEM analysis to optimize the performance of the LSPMSM. An improved efficiency of 4% was achieved at the starting of a 1.5 KW motor with a full load.

Sorgdrager et al. [47] proposed a method to study the steady state performance of LSPMSM by dividing the motor into sub-motors, *i.e*., induction motor (IM), and permanent

magnet synchronous motor (PMSM). Then, each sub-motor was designed using a classical method before combining the designs to achieve a LSPMSM. This work was verified by comparing the flux density of the motor with the results of the FEM design, as well as by comparing the synchronous and asynchronous speeds of the motor with the results of commercial package software. This work has been experimentally verified.

Many researchers are also interested in enhancing the steady state performance of the LSPMSM, and these studies are summarized in Table 2.3.

Table 2.3: Most important LSPMSM steady-state analysis between 2008 and 2012

No.	Year	Researcher	Study
1	2008	Lu and Ye [48]	A steady state behavior of a large-scale LSPMSM was studied, which was 250 KW. A high efficiency at synchronous speed was achieved, with good starting ability at high load inertia.
2	2009	Kim *et al.* [49]	A new optimization method was proposed to optimize steady state performance of 1-phase LSPMSM, taking into consideration the nonlinear characteristics of the motor. A good enhancement of the motor performance was achieved relative to the same-sized IM.
3	2009 2010	Fei *et al.* [50] Aliabad [51]	These authors studied the steady-state performance of a small-sized LSPMSM and its synchronization ability.
4	2011	Peralta Sanchez *et al.* [52]	Predicted the steady state response of a LSPMSM using coupled linear circuit method
5	2012	Marcic *et al.* [53]	The researchers compared the steady-state performance of the IM with the same-sized LSPMSM using variable speed drives.

In his thesis, Taylor [54] examined the effect of replacing induction motors by an LSPMSM on the network performance. This work revealed the difference between IM and LSPMSM in starting, harmonic impedances and regeneration during faults. The author was interested in studying the consumed active and reactive power, and the occurrence of voltage change, where the reactive power of LSPMSM increased as a supply voltage decreased due to the synchronism and permanent field.

Aliabad [55] aimed to improve the performance of LSPMSM for synchronization and starting torque, based on a pole with changing winding method in order to eliminate pulsating and braking torques, as well as to enhance the starting torque. The proposed method also solved the synchronization problem. The results were verified using the FEM method. This work yielded very good results regarding synchronization, high starting torque, and high steady state performance.

Miller [56] studied the effect of the LSPMSM rotor resistance on the synchronization of the motor. In addition, this author investigated the effect of the load moment of inertia. The same author [57] studied and analyzed the starting performance of single-phase LSPMSM by applying an average electromagnetic torque, before examining the performance of the motor for different components of torque. Finally, this concept was generalized to include *m*-phase LSPMSM with unbalanced voltage on the stator.

2.6 Broken rotor bars fault and Non-Intrusive methods of detection in LSPMSM and other AC motors

Broken rotor bars are a common fault in AC machine rotors. Dedicated diagnostic techniques and systems are demanded to detect an upcoming machine defect as early as possible. In this section, features and facts of this fault and their use in diagnosis are detailed. Up to date research in fault severity prediction is also reported.

As mentioned in the previous sections, several researchers were interested in studying and analyzing the design, construction, performance and behavior of the line start permanent magnet synchronous motor. However, there is paucity of studies on the fault monitoring and diagnosis of the motor failures. Still, there is an extensive body of work on the effects, monitoring and detection techniques of the broken rotor bars in induction motors. For example, Hwang [58] proposed an algorithm for detecting the broken bar faults in induction motors based on the dimension order of the frequency signal, which was called FSDO (Frequency Signal Dimension Order). FSDO was used to analyze the stator current signal, as well as estimate the fault type based on the resultant frequency. The fault decision model analyzed the data derived from FSDO to decide whether there is a fault or not based on certain indices. This work was verified by comparing simulation and experimental results pertaining to a 3-phase, squirrel cage induction motor. The main disadvantage of this work was FSDO estimator, which gave a good performance for steady-state operations only.

Carlos [59] demonstrated the effect of the broken bar fault on the stator current signature in the induction motor, and then used the "zero setting protection element" method to detect the occurrence of the broken bar fault under different loading levels. This author has successfully detected the broken rotor bar fault under different loading levels with high accuracy.

Another method for diagnostics of broken rotor bar in induction motors was introduced by Zarei *et al.* [60], who monitored the broken rotor bar in induction motors based on the artificial neural network using "particle swarm optimization" in training process. that work was performed in two stages, commencing with designing a filter to remove noise components from the faulty motor current. The least squares algorithm was also used to find the filter coefficients. In the second stage, a neural network was trained to extract the fault classifications. The output of this network was utilized to classify the state of the motor into four types: healthy bar, cracked on the bar, one and two broken bars.

Guo-Liang [61] proposed a method to diagnose the broken bar faults in induction motors based on "empirical decomposition method". In that work, several intrinsic mode functions (IMF) were used to decompose and analyze the starting current, before applying Hilbert transform for frequency analysis. As a result of this work, and because of the symmetry in the rotor, broken bar fault caused a frequency component *(1-2s)f*, where *s* denotes slip and *f* pertains to source frequency.

Using Hilbert transform, several researchers attempted developing diagnostics methods for broken rotor bar in induction motors under no load conditions. For example, Aydin [62] utilized sliding window for several periods. That method to detect one or two broken bars

only, under no load and with a supply voltage greater than 260 V. The entropy of the incoming data was calculated and compared with some threshold as the first stage. In the second stage, the fault size was determined, *i.e.*, the number of faulty bars. Highly accurate results were obtained using this method with little computation cost in short time, which were tested under limited conditions. On the other hand, this method failed to detect broken bar faults when supply voltage was set to 220 V. Wang [63] applied Hilbert transform and the ensemble empirical mode decomposition (EEMD). First, Hilbert transform was used to extract the motor current envelope, which contains frequency information related to the broken bar fault, and then EEMD algorithm was used to decompose the envelope of the signal into a number of intrinsic mode functions (IMS).

Authors of many previous studies have found that the faulty motors contain two sideband frequencies on the stator current spectrum. Thus, transformation methods such as Fourier, Fast Fourier, Discrete-time Fourier and Wavelet transform have been used to achieve that frequency band. Chen [64] utilized these findings to detect these frequency bands, but because of the limitations in the previously mentioned transformation—where the detection accuracy of broken rotor bar would be affected depending on the loading condition, or even the length of the processed data records—the author used Prony spectrum analysis method to overcome these limitations. The main advantage of that method was its ability to overcome the length restriction of the data window, along with its reliability under light or varying loads. Both mathematical and simulation models were built to implement the effect of broken rotor bars in induction motors by relating its effect to the stator current, which was represented by two sideband frequencies. The author

reported that the amplitude of the frequency component increased as the number of broken bars increased, resulting in a series of harmonies.

Shashi [65], Dhara [66] and Siddiqui [67] proposed methods to detect broken bars fault based on the "Wavelet transform" using different mother wavelet. These models received the phase stator current as an input, after which the authors applied daubechies (db8, db9, db10), and symlet (sym7, sym8) mother wavelets to analyze the stator current components. The results were compared to determine the optimal mother wavelet in detecting the broken rotor bars, and to determine the number of faulty bars in the motor. It can be concluded from these studies that, as the load or the number of broken bars increases, the harmonic components will be increased.

On the other hand, there has been relatively little research on the LSPMSM under faulty conditions such as broken bars. Recently, four research articles addressed the behavior of LSPMSM under broken bar conditions. Mehrjou *et al*. [68, 69] used ANSYS Maxwell® software to study the performance of the motor under broken bar fault condition. The authors concentrated on the stator current and air-gap signatures in order to investigate the possibility of broken bar occurrence because of its easy measurability, reliability and high accuracy. Hilbert transform which is the convolution between the original signal (real time stator current) and the function $1/\pi t$ were applied to extract the envelop of the stator current signals. Fourier Transform has been applied on the function $1/\pi t$, which can be viewed as a filter for unity amplitude and ±90 phase depending on the frequency sign of the input signal. The analytic signal, which is created by adding both real and its Hilbert transform signals has been used to filter the negative frequencies of the stator current signals. After the signal envelops at different conditions were obtained, twelve different statistical

features were examined on the obtained envelops for broken bar fault detection. Such features are the Mean, RMS, Energy, Peak index, Tolerance index, etc. The statistical features compared for healthy and faulty motor. The authors indicated that the load effect in the starting time should be considered in fault detection in this type of machine, unlike induction machines. Moreover, the results showed that only seven features from the proposed twelve features could be used for broken bar fault detection. These features are Mean, RMS, RSS, Shape factor, Skewness and Kurtosis index. Other features could not be used because of the occurred overlap between healthy and faulty trends of the current signal. In addition, the same authors [70] and [71] have analyzed the stator current envelope under broken bar condition using statistical features in time domain as a fault diagnosis method. Following up, they applied some statistical features in time domain as a fault diagnostics method.

Based on the literature review, it is evident that mathematical modelling of LSPMSM under broken bar condition has not been performed thus far. Therefore, in this work, a mathematical model of LSPMSM under broken bar fault condition is developed. The accuracy of the developed model will be tested through a comparison with the FEM JMAG® model under different loading levels. In addition, a fault diagnosis technique based artificial neural network was developed.

CHAPTER THREE

MATHEMATICAL MODELING OF LSPMSM WITH BROKEN ROTOR BARS

In order to study the effect of the broken rotor bars and to obtain a useful dataset for fault diagnosis and prediction under broken bar conditions, a dynamic model of LSPMSM was built, as discussed in this chapter. The first section will introduce the methodology used in the LSPMSM design. The detailed design and the required mathematical equations for the healthy motor model will be introduced in Section 2. Section 3 presents the modified mathematical model, to include motor fault under broken bars condition. Finally, simulation results of the built MATLAB/SIMULINK® model for both healthy and faulty motor under broken bar condition at different loading levels will be presented in Section 4. Simulation results introduced in this chapter are also compared with the numerical FEM model introduced in Chapter Four to validate the proposed mathematical model.

3.1 Introduction

LSPMSM has the characteristics of high-efficiency synchronous motors with self-starting capability when connected to a fixed frequency voltage source. The permanent magnets installed on its rotor provide the synchronous excitation. In addition, the rotor cage provides the induction torque for starting. The difference in permeability between the

magnet and the rotor core also results in significant magnetic saliency and reluctance torque at synchronous speed. At startup, the excitation and saliency of the permanent magnets will cause pulsating torque components. When the field strength of the magnet is too high, LSPMSM may fail to synchronize because of the excessive pulsating torque component from the DC excitation of the magnet [7].

Several mathematical models of healthy LSPMSM have been previously developed [7, 72]. Most of these models are built based on symmetric resistance and inductance matrices in both rotor and stator windings. Therefore, the reported designs cannot reflect any asymmetry due to stator or rotor faults. In this chapter, a mathematical model based on the winding function approach (WFA) and the coupled magnetic circuit theory in two axes reference frame is introduced. This model is proposed to include the dynamic behavior of the motor in both transient and steady state. In addition, this model was subsequently used to simulate motor characteristics in both healthy and faulty motors with broken bar condition at different loading levels.

3.2 Mathematical modelling of healthy LSPMSM

LSPMSM stator consists of three sinusoidally distributed windings displaced by 120 degrees with N_s turns. The rotor cage contains N_r bars, forming N_r loops; each loop contains two adjacent rotor bars connected by two end-rings, as shown in Figure 3.1 [73]. For modelling purposes of the LSPMSM, the rotor eddy current losses of the PM are ignored, since the ohmic resistance of the magnet material is 80 times greater than the copper losses

[72]. In addition, the rotor air-gap is assumed to be uniform and the inter-bar currents are ignored.

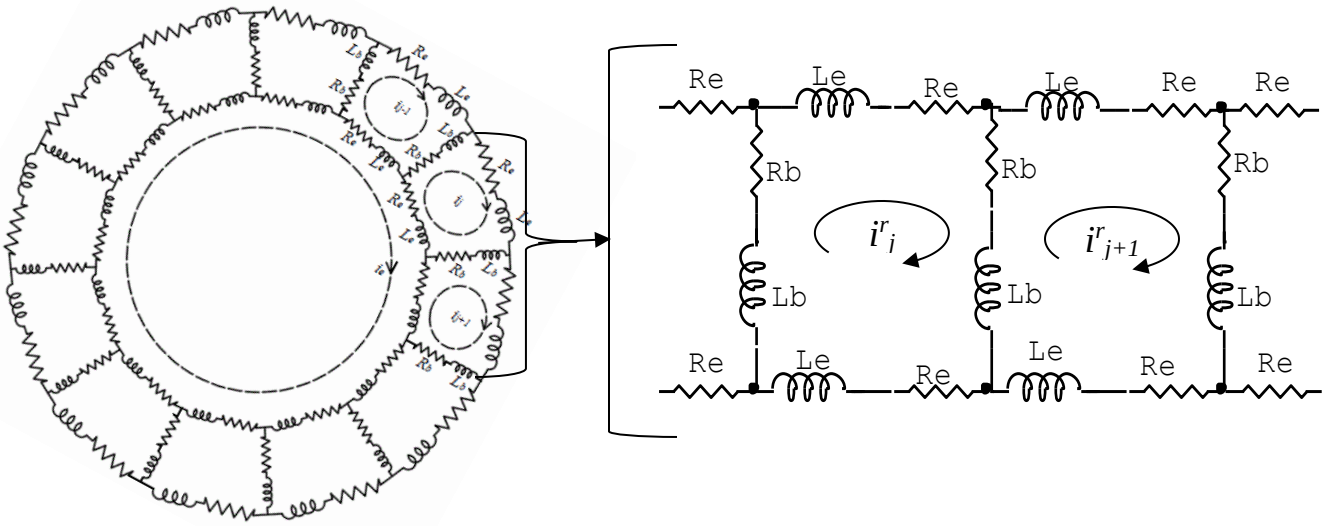

Figure 3.1: Equivalent circuit of the rotor cage

Usually, the Coupled Circuit Approach is used to describe the electromagnetic relationships of the AC machines. Since the stator and rotor circuits of such machines are magnetically coupled. Using the Coupled Circuit Approach and matrix notation, LSPMSM can be presented in terms of the first-order differential equations of the voltages in natural *abc* reference frame, as will be shown in the next sub-sections.

3.2.1 Stator equations in the *abc* and *qd* reference frames

The electric equation of the stator in the *abc* reference frame is defined as [74]:

$$\begin{bmatrix} V_{as} \\ V_{bs} \\ V_{cs} \end{bmatrix} = \begin{bmatrix} r_s & 0 & 0 \\ 0 & r_s & 0 \\ 0 & 0 & r_s \end{bmatrix} \begin{bmatrix} I_{as} \\ I_{bs} \\ I_{cs} \end{bmatrix} + \frac{d}{dt} \begin{bmatrix} \lambda_{as} \\ \lambda_{bs} \\ \lambda_{cs} \end{bmatrix} \quad \textbf{(3.1)}$$

where V_{as}, r_s, I_{as} and λ_{as} are the stator phase *a* voltage, resistance, current and flux linkage, respectively. Subscripts *a*,*b* and *c* are the stator phases. The stator flux linkage vector λ is defined as:

$$\lambda_s = L_s I_s + L_{sr} I_r + \lambda_{pm} \quad \textbf{(3.2)}$$

where L_s is the inductance matrix of the stator, L_{sr} is the mutual inductance between stator and rotor, I_r is the rotor current vector and λ_{pm} is the flux linkage vector due to the presence of the PMs on the rotor.

The inductance matrix of the stator L_s is a 3×3 symmetric matrix pertaining to stator currents only; which can be represented as follows:

$$L_s = \begin{bmatrix} L_{as} & L_{abs} & L_{acs} \\ L_{bas} & L_{bs} & L_{bcs} \\ L_{cas} & L_{cbs} & L_{cs} \end{bmatrix} \quad \textbf{(3.3)}$$

where L_{ks} is the self-inductance of the stator coils, $k \in \{a,b,c\}$. L_{ijs}, $i,j \in \{a,b,c\}$ and $i \neq j$ is the mutual inductance between the stator coils. The mutual inductance between stator coils and rotor loops L_{sr} is a $3 \times N_r$ matrix pertaining to the interaction between stator and rotor currents, as depicted in below:

$$L_{sr} = \begin{bmatrix} L_{s_a r_1} & L_{s_a r_2} & \cdots & L_{s_a r_{Nr}} \\ L_{s_b r_1} & L_{s_b r_2} & \cdots & L_{s_b r_{Nr}} \\ L_{s_c r_1} & L_{s_c r_2} & \cdots & L_{s_c r_{Nr}} \end{bmatrix} \quad \textbf{(3.4)}$$

where subscripts S_i , $i \in \{a,b,c\}$ and r_j, $j \in \{1, 2 \ldots Nr\}$ are the stator coil phases and the rotor loop numbers, respectively.

In addition, rotor current vector contains the current of each rotor bar. For N_r rotor bars, the current vector can be represented as follows:

$$I_r = \begin{bmatrix} I_{r1} \\ I_{r2} \\ \vdots \\ I_{r\,Nr} \end{bmatrix} \quad \textbf{(3.5)}$$

where each vector element represent loop current.

The flux linkage vector of the PM λ_{pm} is changes in relation to the rotor angle; and can be expressed as follows:

$$\begin{bmatrix} \lambda_{a,pm} \\ \lambda_{b,pm} \\ \lambda_{c,pm} \end{bmatrix} = \lambda'_m \begin{bmatrix} cos\left(\theta_r\right) \\ cos\left(\theta_r - 120\right) \\ cos\left(\theta_r + 120\right) \end{bmatrix} \quad \textbf{(3.6)}$$

where λ'_m is the peak flux linkage due to the PM and $\theta_r = \omega_r t$ is the rotor angular velocity.

For modelling purposes, a change in the variables is required to transform the three phases of the stator coils and N_r rotor loops to the two axes reference frame described in Chapter One. Therefore, Park's transformation (K_s) is used to transform the three stator phases into two axes synchronous reference frame, while the poly-phase to two phase transformation (K_r) is used to transform N_r rotor loops. K_s and K_r are defined as follows:

$$K_s = \sqrt{\frac{2}{3}}\begin{bmatrix} cos(\theta_r) & cos(\theta_r - \frac{2\pi}{3}) & cos(\theta_r + \frac{2\pi}{3}) \\ sin(\theta_r) & sin(\theta_r - \frac{2\pi}{3}) & sin(\theta_r + \frac{2\pi}{3}) \end{bmatrix} \quad \textbf{(3.7)}$$

$$K_r = \sqrt{\frac{2}{N_r}}\begin{bmatrix} cos\left(-\frac{p\alpha_r}{2}\right) & \dots & cos\left(-\frac{p(2j-1)\alpha_r}{2}\right) \\ sin\left(-\frac{p\alpha_r}{2}\right) & \dots & sin\left(-\frac{p(2j-1)\alpha_r}{2}\right) \end{bmatrix} \quad \textbf{(3.8)}$$

where j is the rotor loop number and α_r is the angle between two adjacent rotor loops, defined as follows:

$$\alpha_r = \frac{2\pi}{N_r} \quad \textbf{(3.9)}$$

Using K_s transformation matrix, the stator parameters in the *qd* reference frame can be expressed as follows:

$$V_{qds} = K_s R_s K_s^{-1} I_{qds} + K_s \frac{d}{dt}\left(K_s^{-1}\lambda_{qds}\right) \quad \textbf{(3.10)}$$

Therefore, the electric equations of the stator in *qd* become:

$$\begin{bmatrix} V_{qs} \\ V_{ds} \end{bmatrix} = \begin{bmatrix} r_{qs} & r_{qds} \\ r_{qds} & r_{ds} \end{bmatrix}\begin{bmatrix} i_{qs} \\ i_{ds} \end{bmatrix} + \frac{d}{dt}\begin{bmatrix} \lambda_{qs} \\ \lambda_{ds} \end{bmatrix} + \begin{bmatrix} \omega_r \lambda_{ds} \\ -\omega_r \lambda_{qs} \end{bmatrix} \quad \textbf{(3.11)}$$

Where the rotor resistances defined as follows:

$$\begin{aligned} r_{qs} &= \frac{2}{3}(R_{s2} + R_{s3}) \\ r_{ds} &= \frac{2}{3}R_{s1} + \frac{1}{6}(R_{s2} + R_{s3}) \\ r_{qds} &= \frac{2}{2\sqrt{3}}(R_{s2} - R_{s3}) \end{aligned} \quad \textbf{(3.12)}$$

Where r_{qs}, r_{ds} are the quadrature and direct axes resistances of the stator and r_{qds} is the mutual resistance between q and d axes. It is important to note that in healthy case, the following equations hold:

$r_{s1}=r_{s2}=r_{s3}$

$r_{qds}=r_{dqs}=0$

The flux linkage vector of the stator in the *qd* reference frame can be written as:

$$\lambda_{qds} = L_{qds} I_{qds} + L_{qd,sr} I_{qdr} + \lambda'_{qd,pm} \quad \textbf{(3.13)}$$

Where the stator inductances are defined as follows:

$$L_{qds} = K_s L_s K_s^{-1} = \begin{bmatrix} L_{qs} & L_{qds} \\ L_{qds} & L_{ds} \end{bmatrix} \quad \textbf{(3.14)}$$

$$L_{qd,sr} = K_s L_{sr} K_r^{-1} = \begin{bmatrix} L_{q,sr} & L_{qd,sr} \\ L_{dq,sr} & L_{d,sr} \end{bmatrix} \quad \textbf{(3.15)}$$

$$\lambda'_{qd,pm} = K_s \lambda'_{abc,m} K_s^{-1} = \begin{bmatrix} 0 \\ \lambda'_m \end{bmatrix} \quad \textbf{(3.16)}$$

Where L_{qds} is self inductance matrix of the stator. $L_{qd,sr}$ is the mutual coupling inductance between stator and rotor and $\lambda_{qd,pm}$ is the PM flux linkage. It is important to note that in healthy case, the following equations hold:

$L_{sa}=L_{sb}=L_{sc}=L_S$

$L_{qds}=L_{dqs}=0$

However, the PM inductance can be combined with the *d-axis* mutual inductance ($L_{md}= L_{d,sr}= L_{d,rs}$), in line with the LSPMSM rotor construction, shown in Figure 3.2 [7]. Therefore, the magnetizing flux of the PM is defined as:

$$\lambda'_m = L_{md} i'_m \quad \textbf{(3.17)}$$

where i'_m is the equivalent magnetizing current of the PM referred to the stator side.

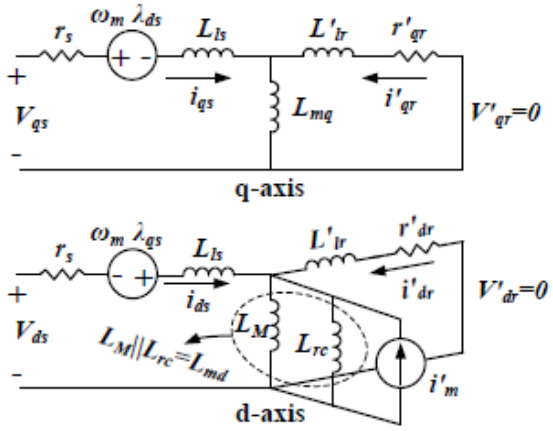

Figure 3.2: Rotor equivalent circuits of a 3-phase LSPMSM in qd reference frame

3.2.2 Rotor equations in the *abc* and *qd* reference frames:

It is documented in the pertinent literature that LSPMSM is a highly symmetrical motor; thus, any fault will cause a degree of asymmetry in its parameters. However, broken rotor bars fault will cause asymmetry in the rotor resistance and inductance matrices. In addition, such fault type will affect the mutual coupling inductance matrices between rotor and stator. In order to study the effect of the broken bar fault on the LSPMSM, this model should be modified to include the effect of each rotor bar. The rotor cage includes N_r loops, and each loop includes two bar leakage inductances, two bar resistances, two end-ring leakage inductances and two end-ring resistances. Hence, the voltage mesh equation governing the j^{th} loop shown in Figure 3.1 is defined as follows [73]:

$$0 = 2(R_b + R_e)I_j - R_b I_{(j-1)} - R_b I_{(j+1)} + \frac{d}{dt}\lambda_{rj} \qquad \textbf{(3.18)}$$

where R_b and R_e are the rotor bar and end-ring resistances, respectively, while the subscripts r,j denotes the rotor and the rotor loop number, respectively. I_j, λ_r are the rotor bar current and flux, respectively. Thus, the general rotor electric equation can be written as:

$$0 = R_r I_r + \frac{d}{dt}\lambda_r \quad \textbf{(3.19)}$$

where R_r is a $N_r \times N_r$ equivalent rotor resistance matrix, described as follows:

$$R_r = \begin{bmatrix} 2(R_b + R_e) & -R_b & \cdots & -R_b \\ -R_b & 2(R_b + R_e) & \cdots & 0 \\ \vdots & \vdots & \ddots & \vdots \\ -R_b & 0 & \cdots & 2(R_b + R_e) \end{bmatrix} \quad \textbf{(3.20)}$$

The rotor flux is a combination of the self-flux, which is coming from the rotor loops current, the mutual flux between stator coils and rotor loops and the PM flux, which can be expressed as follows:

$$\lambda_r = L_r I_r + L_{rs} I_s + \lambda_{pm}$$
$$\lambda_{rj} = \left(L_{rp} + 2(L_b + L_e)\right) I_{rj} + \sum_{\substack{k=1 \\ k \neq j}}^{N_r} M_{rr} I_k + \sum_{k=1}^{3} M_{rjsk} I_k - L_b I_{(j-1)} - L_b I_{(j+1)} + \lambda_{pm} \quad \textbf{(3.21)}$$

The total inductance of the j^{th} rotor loop is equal to the sum of its principal inductance (L_{rp}) which is the magnetizing inductance of each rotor loop, the linkage inductance of the two bars in the loop (L_b) and the linkage inductance of the two end-rings closing the loop (L_e), which can be defined as follows:

$$L_{rr} = \left(L_{rp} + 2(L_b + L_e)\right) \quad \textbf{(3.22)}$$

The mutual inductance between two adjacent meshes ($L_{rk(k-1)} = L_{rk(k+1)}$, $k \in \{1, 2 \ldots Nr\}$ can be defined as follows:

$$L_{rk(k\pm1)} = M_{rr} - L_b \quad \textbf{3.23)}$$

where M_{rr} is the mutual magnetic coupling (magnetizing inductance) between two rotor loops. Therefore, the general expression of the rotor cage inductance can be rearranged in $N_r \times N_r$ matrix, as follows:

$$Lr = \begin{bmatrix} L_{rp} + 2\,(L_b + L_e) & M_{rr} - L_b & M_{rr} & \dots & L_{1Nr} - L_b \\ M_{rr} - L_b & L_{rp} + 2\,(L_b + L_e) & M_{rr} - L_b & \dots & M_{rr} \\ \vdots & \vdots & \vdots & \ddots & \vdots \\ M_{rr} - L_b & M_{rr} & M_{rr} & \dots & L_{rp} + 2\,(L_b + L_e) \end{bmatrix} \quad \textbf{(3.24)}$$

The mutual inductance between rotor and stator is the transpose of the matrix in Equation (3.4), and is given as follows:

$$L_{rs} = \begin{bmatrix} L_{r_1 s_a} & L_{r_1 s_b} & L_{r_1 s_c} \\ L_{r_2 s_a} & L_{r_2 s_b} & L_{r_2 s_c} \\ \vdots & \vdots & \vdots \\ L_{r_{Nr} s_a} & L_{r_{Nr} s_b} & L_{r_{Nr} s_c} \end{bmatrix} \quad \textbf{(3.25)}$$

One further step is required for simulation purposes, in which rotor parameters are transformed from the *abc* to the *qd* reference frame using the K_r transformation matrix. Therefore, the rotor electrical equation in the *qd* reference frame can be written as follows:

$$V_{qdr} = [0] = K_r R_r K_r^{-1} I_{qdr} + K_r \frac{d}{dt}(K_r^{-1} \lambda_{qdr}) \quad \textbf{(3.26)}$$

$$0 = R_{qdr} I_{qdr} + \frac{d}{dt} \lambda_{qdr} \quad \textbf{(3.27)}$$

where:

$$R_{qdr} = \begin{bmatrix} r_{qr} & r_{qdr} \\ r_{dqr} & r_{dr} \end{bmatrix} \quad \textbf{(3.28)}$$

Where r_{qr}, r_{dr} are the quadrature and direct axes resistances of the rotor and r_{qdr}, r_{dqr} are the mutual resistance between *q* and *d* axes of the rotor. In addition, rotor flux equation in the *qd* reference frame can be expressed as follows:

$$\lambda_{qdr} = L_{qdr} I_{qdr} + L_{qd,rs} I_{qds} + \lambda_{qd,pm} \quad \textbf{(3.29)}$$

where:

$$L_{qdr} = K_r L_r K_r^{-1} = \begin{bmatrix} L_{qr} & L_{qdr} \\ L_{dqr} & L_{dr} \end{bmatrix} \tag{3.30}$$

Where L_{qr}, L_{dr} are the self-inductance of the rotor on the *q* and *d* axes, respectively. L_{qdr} and L_{dqr} are the mutual inductances between both *q* and *d* axes, respectively. The final stator and rotor equations for LSPMSM in the *qd* reference frame are defined as:

$$\begin{bmatrix} V_{qs} \\ V_{ds} \\ V_{qr} \\ V_{dr} \end{bmatrix} = \begin{bmatrix} r_s & 0 & 0 & 0 \\ 0 & r_s & 0 & 0 \\ 0 & 0 & r'_{qr} & 0 \\ 0 & 0 & 0 & r'_{dr} \end{bmatrix} \begin{bmatrix} I_{qs} \\ I_{ds} \\ I'_{qr} \\ I'_{dr} \end{bmatrix} + \frac{d}{dt} \begin{bmatrix} \lambda_{qs} \\ \lambda_{ds} \\ \lambda'_{qr} \\ \lambda'_{dr} \end{bmatrix} + \begin{bmatrix} \omega_r \lambda_{ds} \\ -\omega_r \lambda_{qs} \\ 0 \\ 0 \end{bmatrix} \tag{3.31}$$

$$\begin{bmatrix} \lambda_{qs} \\ \lambda_{ds} \\ \lambda'_{qr} \\ \lambda'_{dr} \end{bmatrix} = \begin{bmatrix} L_{ls}+L_{mq} & 0 & L_{mq} & 0 \\ 0 & L_{ls}+L_{md} & 0 & L_{md} \\ L_{mq} & 0 & L'_{lr}+L_{mq} & 0 \\ 0 & L_{md} & 0 & L'_{lr}+L_{md} \end{bmatrix} \begin{bmatrix} i_{qs} \\ i_{ds} \\ i'_{qr} \\ i'_{dr} \end{bmatrix} + \begin{bmatrix} 0 \\ \lambda'_m \\ 0 \\ \lambda'_m \end{bmatrix} \tag{3.32}$$

$$w_r(t) = \frac{d}{dt}\theta_r(t) = \left(\frac{P}{2J}\right)\int\left(T_{em} + T_{mech} - T_{damp}\right) dt \tag{3.33}$$

$$T_{em} = \left(\frac{3}{2}\right)\left(\frac{P}{2}\right)\left(\underbrace{L_{md} i'_{dr} i_{qs}}_{Cage-torque} + \underbrace{\lambda'_m i_{qs}}_{PM-torque} + \underbrace{(L_{md} - L_{mq}) i_{ds} i_{qs}}_{Reluctance-torque}\right) \tag{3.34}$$

where the primed quantities indicate that; the values are referred to the stator side. The subscripts *s*, *r* refer to the stator and rotor, respectively. (V_{qs}, V_{ds}), ($V_{qr,}$ V_{dr}), (I_{qs}, I_{ds}), (I'_{qr}, I'_{dr}), (λ_{qs}, λ_{ds}) and (λ'_{qr}, λ'_{dr}) are the *quadrature* and *direct* axes of the stator and rotor voltages, currents and flux linkages, respectively. r_s is the stator resistance and (r'_{qr}, r'_{dr}) are the rotor resistances in the *q* and *d* reference frames, respectively. ω_r is the angular speed and (L_{ls}, L'_{lr}) are the stator and rotor leakage inductances, respectively. In addition, (L_{mq}, L_{md}) are the mutual inductances in the *q* and *d* reference frames, respectively. (T_{em}, T_{load}, and T_{damp}) are the motor electromechanical torque, the mechanical

torque applied by the load and the damping torque in the direction opposite to the rotor rotation, respectively. Finally, J denotes the rotor inertia and P is the number of motor poles.

Equation (3.31) describes the stator and rotor electric voltages in the *qd* reference frame, while Equation (3.32) provides the stator and rotor fluxes in the *qd* reference frame. In addition, the rotor angular rotation and electromagnetic torque of the LSPMSM are given in Equations (3.33) and (3.34), respectively. Therefore, Equations (3.31) − (3.34) represent the mathematical model of the *healthy* LSPMSM.

3.2.3 Inductance Calculation of the Healthy LSPMSM

In this work, "Winding function approach (WFA)" was used to derive the inductance matrices of the stator and the rotor, i.e., L_{ss}, $L_{m(sr)}$, L_{rr} and $L_{m(rs)}$. WFA is used to describe the coils along the airgap geometrically. According to the pertinent litrature, and for uniform air-gap, the mutual inductance between any two windings x and y is given by [75]:

$$L_{xy}(\theta_r) = \frac{\mu_o l r}{g} \int_0^{2\pi} W_x(\theta_r, \gamma) W_y(\theta_r, \gamma) d\gamma \qquad \textbf{(3.35)}$$

where μ_o is the space permeability, r is the average radius of the air-gap, g is the radial air-gap length, l is the motor stack length, θ_r corresponds to the rotor angular position with respect to the stator reference frame and γ is the angle along the airgap (angular position along the stator inner surface). W_x and W_y denote the winding distribution function (Magnetomotive force distribution along the airgap for the unit current) of the x and y windings, respectively.

However, the motor utilized in the present study has a 3-phase stator, each with N_s windings. Thus, in order to obtain a smooth MMF, a sinusoidal distribution of the stator windings along the airgap should be used. The winding function of the stator phase *a* is shown in Figure 3.3 and can be described as follows [76]:

$$W_{sa}(\gamma) = \frac{N_s}{2}\cos(\gamma) \tag{3.36}$$

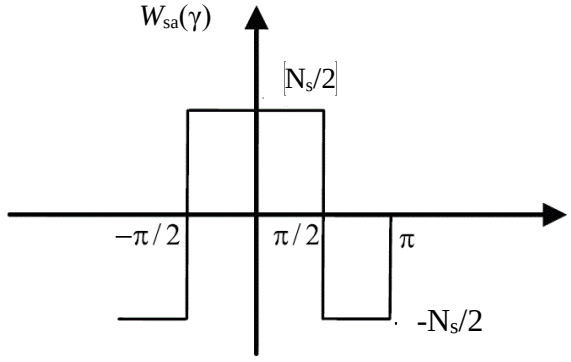

Figure 3.3: Winding distribution of each stator coil

In addition, and as mentioned previously, rotor cage is modeled as N_r magnetically coupled loops. Each two adjacent rotor loops *i* and *i+1* are separated by the angles θ_i and θ_{i+1}, respectively. The radius of each rotor loop (a_r) can be defined as follows:

$$\alpha_r = \theta_{i+1} - \theta_i = \frac{2\pi}{N_r} \tag{3.37}$$

Since the rotor bars are equidistantly placed along the rotor circumference, which is non-sinusoidal distribution, the non-sinusoidal distribution of the loop winding was used. In order to calculate the rotor cage inductances, the winding function of the i^{th} rotor loop is shown in Figure 3.4 and can be expressed as follows [73]:

$$W_{ri}(\beta)=\begin{cases}-\frac{\alpha_r}{2\pi}, 0\le\theta_r\le\theta_i\\ 1-\frac{\alpha_r}{2\pi}, \theta_i\le\theta_r\le\theta_{i+1}\\ -\frac{\alpha_r}{2\pi}, \theta_{i+1}\le\theta_r\le 2\pi\end{cases} \quad \textbf{(3.38)}$$

where W_{ri} is the rotor loop winding function and θ_i , θ_{i+1} are the positions of two adjacent rotor bars that form the rotor loop.

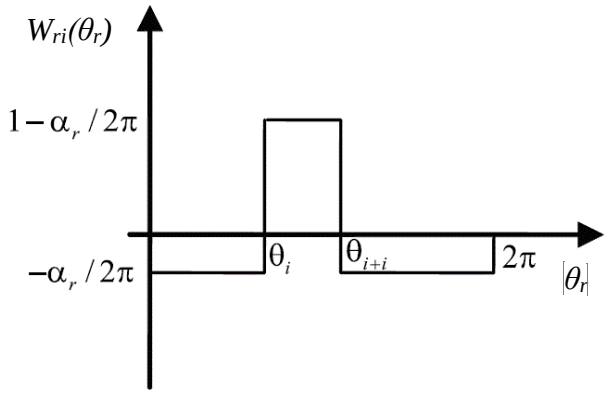

Figure 3.4: Winding distribution of each rotor loop

By applying the previous winding function definitions on the stator and rotor parameters, it is possible to calculate the stator and rotor self and mutual inductances.

A. Stator self and mutual inductances:

The stator flux linkage due to the stator current is caused by self-inductance of the stator coils, which is the sum of the stator phase leakage and the magnetizing inductances, given by:

$$L_{sa}=L_{sb}=L_{sc}=L_{ls}+L_{msi} \quad \textbf{(3.39)}$$

where L_{ls} is the stator leakage inductance, and L_{msi} , $i \in \{a,b,c\}$ is the stator phase magnetizing inductance calculated by substituting Eq. (3.36) into Eq. (3.35). For instance, the magnetizing-inductance of the phase *a* is calculated as follows [75]:

$$L_{msa} = \frac{\mu_o lr}{g}\int_0^{2\pi} W_{sa}^2 d\gamma = \int_0^{2\pi} (\frac{N_{sa}}{2}cos(\gamma))^2 d\gamma$$
$$= \frac{\mu_o lr}{g} N_{sa}^2 (\frac{\pi}{4}) \quad \textbf{(3.40)}$$

For the remaining stator phases *b* and *c*, the same steps are followed, where $L_{msa}=L_{msb}=L_{msc}$ [76]. In addition, the mutual inductance of the stator coils *i* and *j*, $i, j \in \{a,b,c\}$ and $(i \neq j)$, is given by [73]:

$$L_{sisj} = \frac{-L_{ms}}{2} \quad \textbf{(3.41)}$$

The stator flux linkage due to the rotor current results in the mutual inductance between the stator coils and the rotor loops. The mutual inductance between the stator phase $j \in \{a,b,c\}$ and the rotor loop $i \in \{1,2, \ldots Nr\}$ can be calculated by substituting Eq. (3.36) and Eq. (3.38) into Eq. (3.35), as follows:

$$L_{m(sjri)} = \frac{\mu_o lr}{g}\int_0^{2\pi} W_{si}(\gamma+\theta_r) W_{rj}(\gamma) d\gamma$$
$$= \frac{\mu_o lr}{g}(\frac{N_s}{2}) \left(\begin{array}{l} -\frac{1}{N_r}\left[sin(\gamma+0)\Big|_0^{(i-1)\alpha_r} + sin(\gamma+0)\Big|_{i\alpha_r}^{2\pi} \right] \\ +\frac{N_r-1}{N_r}\left[sin(\gamma+\theta_r)\Big|_{(i-1)\alpha_r}^{i\alpha_r} + sin(\gamma+0)\Big|_{i\alpha_r}^{2\pi} \right] \end{array} \right) \quad \textbf{(3.42)}$$
$$= \frac{\mu_o lr}{g}(\frac{N_s}{2})\left(sin(\theta_r + i\alpha_r) - sin(\theta_r + (i-1)\alpha_r) \right)$$
$$= \frac{\mu_o lr}{g} N_s \, sin\left(\frac{\alpha_r}{2}\right) cos\left(\theta_r + (2i-1)\frac{\alpha_r}{2} - (j-1)\frac{2\pi}{3}\right)$$

From Eq. (3.42), it can be noted that the mutual inductance depends on the relative position between stator and rotor, i.e. θ_r.

B. Rotor self and mutual inductances:

Rotor current contributes a flux linkage on the rotor loops, which can be represented by the loop self-inductance L_{rp}. Loop inductance can be calculated by substituting Eq. (3.38) into Eq. (3.35), as follows:

$$
\begin{aligned}
L_{rp} &= \frac{\mu_o l r}{g}\int_0^{2\pi} W_{rk}^2(\theta_r)\,d\theta_r \\
&= \frac{\mu_o l r}{g}\left(\int_0^{(k-1)\alpha_r}\frac{1}{N_r^2}d\theta_r + \int_{(k-1)\alpha_r}^{k\alpha_r}\frac{(N_r-1)^2}{N_r^2}d\theta_r + \int_{k\alpha_r}^{2\pi}\frac{1}{N_r^2}d\theta_r\right) \\
&= \frac{\mu_o l r}{g}\alpha_r\left(1-\frac{\alpha_r}{2\pi}\right)
\end{aligned}
\qquad \textbf{(3.43)}
$$

Moreover, the mutual inductance between two rotor loops *i* and *j*, $i, j \in \{1, 2, \ldots N_r\}$ *and* $(i \neq j)$ can be calculated by substituting (3.38) in (3.35), as follows:

$$
\begin{aligned}
M_{rr} = L_{rij} &= \frac{\mu_o l r}{g}\int_0^{2\pi} W_{ri}(\theta_r)W_{rj}(\theta_r)\,d\theta_r \\
&= \frac{\mu_o l r}{g}\frac{1}{N_r^2}\left(\int_0^{(i-1)\alpha_r} d\theta_r + \int_{i\alpha_r}^{(j-1)\alpha_r} d\theta_r + \int_{j\alpha_r}^{2\pi} d\theta_r\right) \\
&- \frac{\mu_o l r}{g}\frac{N_r-1}{N_r^2}\left(\int_{(i-1)\alpha_r}^{i\alpha_r} d\theta_r + \int_{(j-1)\alpha_r}^{j\alpha_r} d\theta_r\right) \\
&= \frac{\mu_o l r}{g}\alpha_r\left(1-\frac{\alpha_r}{2\pi}\right) \\
L_{rij} &= \frac{\mu_o l r}{g}\left(\frac{\alpha^2_r}{2\pi}-\frac{\alpha^2_r}{2\pi}-\frac{\alpha^2_r}{2\pi}\right) \\
&= -\frac{\mu_o l r}{g}\left(\frac{\alpha^2_r}{2\pi}\right)
\end{aligned}
\qquad \textbf{(3.44)}
$$

where $W_{r(i,j)}(\theta)$ is the winding function of the rotor *i* and *j* adjacent loops.

3.3 Mathematical modelling of LSPMSM with broken bars

LSPMSM is a highly symmetrical motor; thus, any fault will cause a degree of asymmetry in its parameters. However, a broken rotor bar fault will cause asymmetry in the rotor resistance, self-inductance and mutual coupling inductance between rotor and stator matrices, since there is no current flows through the broken rotor bar. Thus, no magnetic flux is generated around the broken bar, as illustrated in Figure 3.5. Consequently, asymmetry in the rotor parameters generates asymmetry in the rotor magnetic field by yielding a non-zero backward rotating field. It has to be noted that, for a symmetrical rotor with no broken bars, the resultant effect of the backward rotating fields is zero. This non-zero backward- rotating field induces harmonic currents in the stator windings, which are superimposed on the stator currents [77]. These superimposed harmonics are used as attributes of broken rotor bars fault in motor current signature analysis (MCSA) techniques.

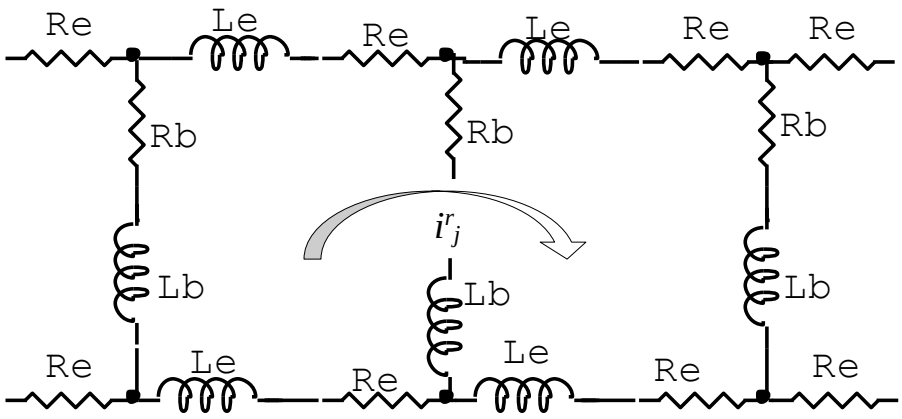

Figure 3.5: Illustration of a broken bar in the mathematical model

Different approaches can be utilized to model the broken rotor bar. In the first approach, the broken bar is represented with a very high resistance while leaving the circuit topology

unchanged. In the second approach, the circuit topology is modified by removing the broken bar from the circuit using Kirchhoff's law. The second approach is better because the high resistance method could introduce unfavorable numerical conditions and instability when the broken bar is removed. Therefore, broken bars were represented in this study by simply eliminating the faulty bar elements, i.e., resistances and inductances [78].

If the broken bar is N_r, then the fault will affect rotor current vector described in Eq. (3.5), which can be represented by removing $i_{r(Nr)}$ element. In addition, the fault will eliminate the N_r row and column from both matrices R_r and L_r described in Eq. (3.20) and (3.24), respectively. The remaining N_r-*1* branches in both equations should be re-evaluated. In addition, the effect of the fault on the mutual coupling matrix is represented by eliminating column number N_r from L_{sr} matrix described in Eq. (3.4), and the row number N_r from L_{rs} matrix described in Eq. (3.25). Re-evaluation of the remaining N_r-1 rows and columns is required. The fault will also change the separation angle (α_r) with the adjacent bar of the faulty bar N_r, i.e., it will be doubled. Therefore, the WFA used in Eq. (3.38) will be changed in the case of faulty loop to be as shown in Figure 3.6and described in equation (3.45).

$$W_{r(Nr-1)}(\beta) = \begin{cases} -\frac{\alpha_r}{\pi}, 0 \le \theta_r \le \theta_{(Nr-1)} \\ 1-\frac{\alpha_r}{\pi}, \theta_{(Nr-1)} \le \theta_r \le 2\pi \end{cases} \quad \textbf{(3.45)}$$

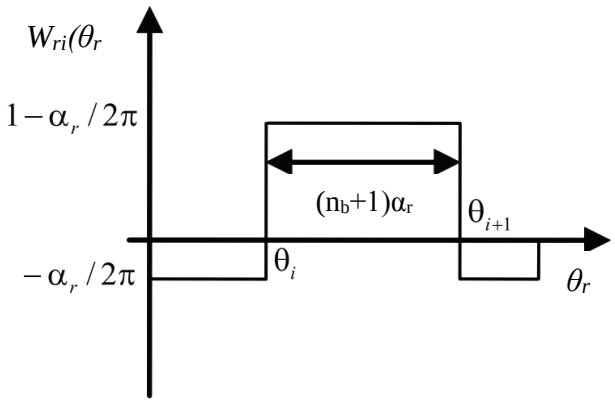

Figure 3.6: Winding distribution of n_b bars broken

According to this change in the WF, rotor self-inductance of the loop N_r *-1* will be recalculated as follows:

$$L_{rp(N_r-1)(N_r-1)} = \frac{\mu_0 lr}{g}\int_0^{2\pi} W_{r(N_r-1)}^2(\theta_r)d\theta_r$$
$$= \frac{\mu_0 lr}{g}\left(\int_0^{(N_r-2)\alpha_r}\frac{4}{N_r^2}d\theta_r + \int_{(N_r-2)\alpha_r}^{2\pi}\frac{(N_r-2)^2}{N_r^2}d\theta_r\right) \quad \textbf{(3.46)}$$
$$= \frac{\mu_0 lr}{g}2\alpha_r(1-\frac{\alpha_r}{\pi})$$

In addition, the rotor mutual inductance between the loop N_r *-1* and the other loops in the matrix will be recalculated, as follows:

$$L_{r(N_r-1)i} = \frac{\mu_0 lr}{g}\int_0^{2\pi} W_{ri}(\theta_r)W_{r(N_r-1)}(\theta_r)d\theta_r$$
$$= \frac{\mu_0 lr}{g}\frac{2}{N_r^2}\left(\int_0^{(i-1)\alpha_r} d\theta_r + \int_{i\alpha_r}^{(N_r-2)\alpha_r} d\theta_r\right)$$
$$-\frac{\mu_0 lr}{g}\left(\frac{2(N_r-1)}{N_r^2}\int_{(i-1)\alpha_r}^{i\alpha_r} d\theta_r + \frac{(N_r-2)}{N_r^2}\int_{(N_r-2)\alpha_r}^{2\pi} d\theta_r\right) \quad \textbf{(3.47)}$$
$$= \frac{\mu_0 lr}{g}\left(\frac{\alpha^2_r}{\pi} - \frac{\alpha^2_r}{\pi} - \frac{\alpha^2_r}{\pi}\right)$$
$$= -\frac{\mu_0 lr}{g}\frac{\alpha^2_r}{\pi}$$

Finally, the mutual inductance between the stator coils and the rotor loop N_r *-1* will be recalculated, as follows:

$$
\begin{aligned}
L_{m(s_i r_{N_r-1})} &= \frac{\mu_o lr}{g}\int_0^{2\pi} W_{si}(\gamma+\theta_r)W_{r_{N_r-1}}(\theta_r)d\theta_r \\
&= \frac{\mu_o lr}{g}(\frac{N_s}{2})\left(-\frac{2}{N_r}\left[sin(\gamma+\theta_r)\Big|_0^{(N_r-2)\alpha_r}\right]+\frac{N_r-2}{N_r}\left[sin(\gamma+\theta_r)\Big|_{(N_r-2)\alpha_r}^{2\pi}\right]\right) \\
&= \frac{\mu_o lr}{g}(\frac{N_s}{2})\left(sin(\theta_r)-sin(\theta_r+2\alpha_r)\right) \\
&= \frac{\mu_o lr}{g}N_s\, sin(\alpha_r)cos(\theta_r+\alpha_r-(j-1)\frac{2\pi}{3})
\end{aligned}
\qquad \textbf{(3.48)}
$$

In general, for n_b broken bars, the target parameters of n_b faulty branches will be eliminated from the rotor resistance and inductance matrices. In addition, the n_b columns and rows should be eliminated from the rotor-stator mutual coupling inductance matrix. The remaining (N_r - n_b) branch elements should be re-evaluated to include the fault effect. The results of the rotor inductance matrix and rotor-stator mutual coupling inductance matrix are calculated using MATLAB® based on the aforementioned definitions of the winding functions. The final expressions are given as follows:

$$L_{rp} = \frac{\mu_o lr}{g}\alpha_r\left((n_b+1)-(2n_b+1)\frac{\alpha_r}{2\pi}\right) \qquad \textbf{(3.49)}$$

$$M_{rr} = -\frac{\mu_o lr}{g}\left(\frac{\alpha^2{}_r}{2\pi}\right)(n_b+1) \qquad \textbf{(3.50)}$$

$$L_{m(sjri)} = \frac{\mu_o lr}{g}N_s\, sin\left((n_b+1)\frac{\alpha_r}{2}\right)cos\left(\theta_r+\frac{2i+n_b-1}{2}\alpha_r-(j-1)\frac{2\pi}{3}\right) \qquad \textbf{(3.51)}$$

It should be noted that; the previous modelling does not include the saliency effect of the interior permanent magnets (IPM) on the wound rotor, which will increase the quadrature axis inductance over the direct axis inductance, i.e., $L_q > L_d$. According to the extant literature, two methods can be employed to represent this effect. In the first one, the

saliency effect in both quadrature and direct axes is taken into consideration, allowing the airgap function to be defined for each one, i.e., g_q and g_d, respectively. However, this method will not include the fault effect in the case of asymmetric inductance matrices. Therefore, the second method, which defines the airgap profile $g(\Phi)$ was adopted in the present study, and is given by [79], [80]:

$$g\left(\Phi\right)=g-g\cos\left(\Phi-\theta_r\right) \tag{3.52}$$

In summary, Eq. (3.18), (3.20), (3.21), (3.49), (3.50), (3.51) and (3.52) describe the LSPMSM under the broken bar conditions.

3.4 Mathematical description of the LSPMSM in integral form

It is preferable to use integral equations over the differential equations described in previous sections to simulate LSPMSM in MATLAB/SIMULINK®. In addition, it is helpful to determine the dependent and independent variables of the integral equations as suggested by [7]. Using the suggested approaches, a model can presented more visually. It will be also more comprehensive and will have lower risk of errors. For this purpose, the stator and rotor flux equations can be rearranged as follows:

$$\begin{aligned}
\lambda_{qs} &= \int\left(V_{qs}-r_s i_{qs}-\omega_m\lambda_{ds}\right)dt\\
\lambda_{ds} &= \int\left(V_{ds}-r_s i_{ds}+\omega_m\lambda_{qs}\right)dt\\
\lambda'_{qr} &= \int\left(V'_{qr}-r'_{qr}i'_{qr}\right)dt=0\\
\lambda'_{dr} &= \int\left(V'_{dr}-r'_{dr}i'_{dr}\right)dt=0
\end{aligned} \tag{3.53}$$

where the current vectors i_{qs}, i_{ds}, i'_{qr} and i'_{dr} can be defined as follows:

$$
\begin{aligned}
i_{qs} &= \frac{\lambda_{qs} - L_{mq} i'_{qr}}{L_{mq} + L_{ls}} \\
i_{ds} &= \frac{\lambda_{ds} - L_{md} \left(i'_{dr} + i'_{m} \right)}{L_{md} + L_{ls}} \\
i'_{qr} &= \frac{\lambda'_{qr} - L_{mq} i_{qs}}{L_{mq} + L_{lr}} \\
i'_{dr} &= \frac{\lambda'_{dr} - L_{md} \left(i_{ds} + i'_{m} \right)}{L_{md} + L_{lr}}
\end{aligned}
\qquad \textbf{(3.54)}
$$

3.5 Modelling of LSPMSM in MATLAB/SIMULINK

MATLAB/SIMULINK® is a software package used to simulate and analyze dynamic systems. It provides a graphical representation facilitated by programming for complex mathematical descriptions. SIMULINK® editor is used to set-up the block diagrams of the described mathematical model. MATLAB® m-files scripts are used for blocks initialization and running time. In order to simulate LSPMSM using MATLAB/SIMULINK®. The simulation procedure proceeds as indicated in the flowchart shown in Figure 3.7.

3.5.1 LSPMSM SIMULINK® block diagrams

In Simulink, modules of the LSPMSM dynamic system comprise of "Function Blocks". Each function block implements one of the expressions in section 3.4. Shared variables are transferred between blocks. Any variable can be conveniently traced and saved by using the "Scope" and the "To Workspace" blocks, respectively. Some other Simulink blocks used in the model include, but not limited to, the "Clock", "Sum", "Gain", "Mux", "Integrator" and "Trigonometric Function" blocks.

The LSPMSM model contains four major modules: the "*abc* - *qd* conversion module", the "Rotor angle calculation module", the "LSPMSM in *qd* reference frame" module and the "*qd-abc* conversion module". Each module will be discussed in detail in the following subsections.

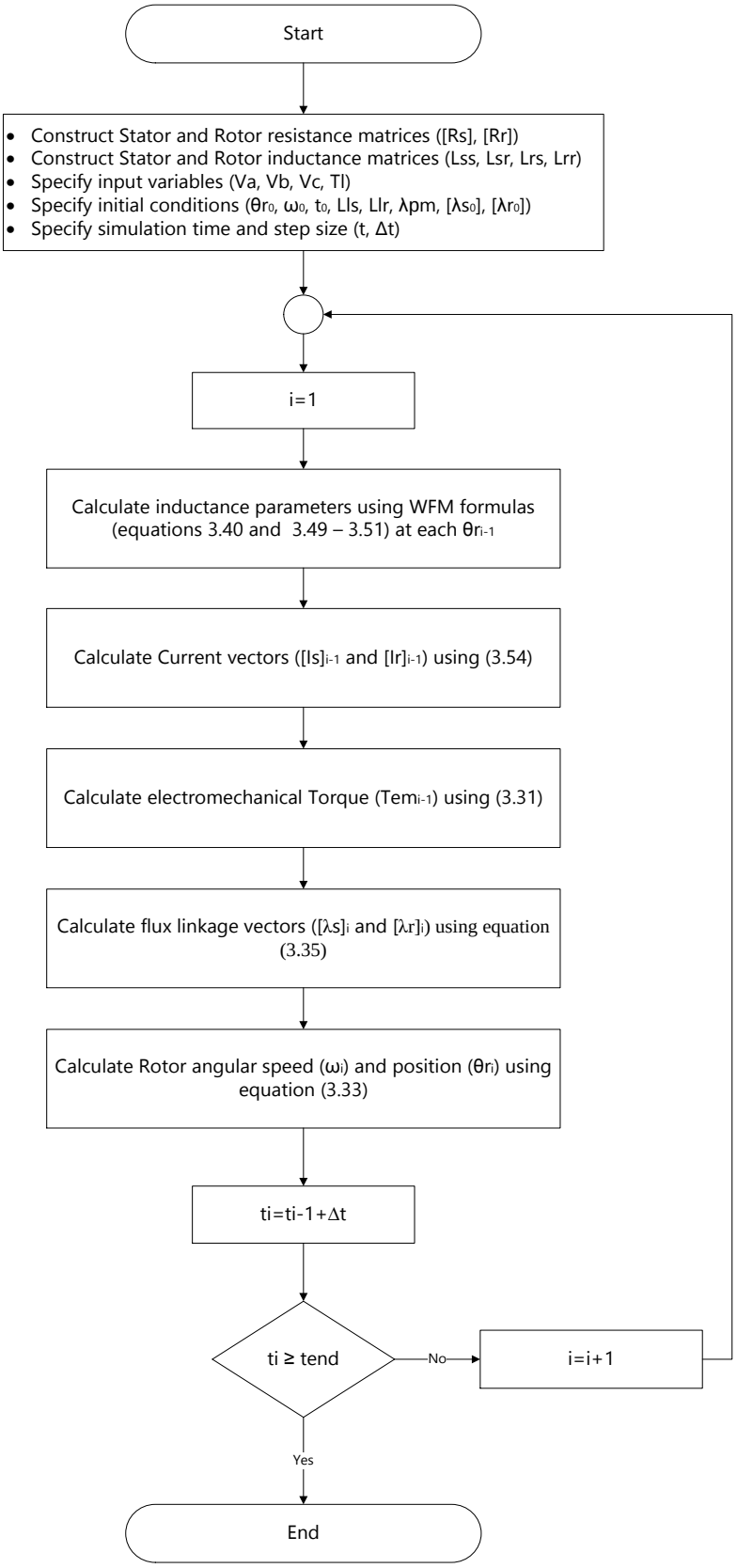

Figure 3.7: The simulation procedure flowchart

A. The *abc-qd* conversion module

This module is used to transform the LSPMSM parameters from the *abc* to the *qd* reference frame based on park's transformation described in Chapter One. Therefore, a 3-phase, 50-Hz fixed frequency stator voltage source is connected to the terminals of this SIMULINK block. As a result, the stator phase voltages are transformed from the *abc* to the *qd* reference frame. Figure 3.8 shows the built conversion module SIMULINK block diagram.

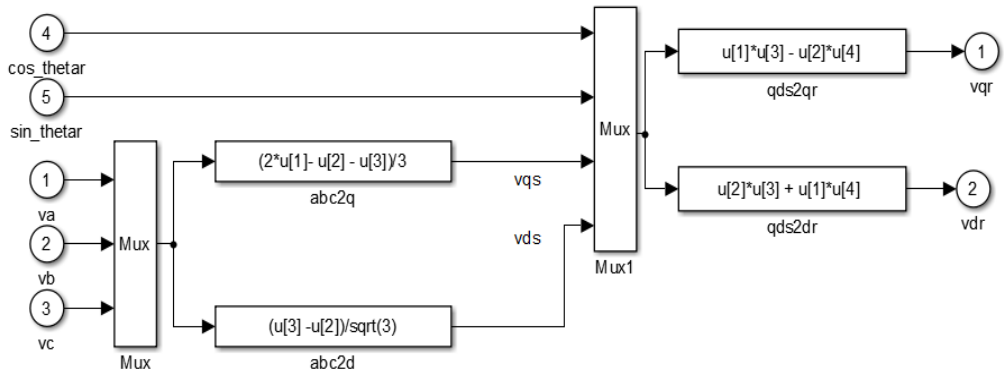

Figure 3.8: *abc-qd* SIMULINK® conversion module

B. Rotor angle calculation module

This module is built to calculate the rotor angle using rotor speed equation described in Eq. (3.33) as an input. However, the calculated rotor angle in this module, *i.e.* θ_r will be used as an input to the conversion and other modules. The output trigonometric functions $sin(\theta_r)$ and $cos(\theta_r)$ are used to calculate the stator and rotor parameters in the *qd* reference frame. Figure 3.9 shows the built LSPMSM rotor angular speed module.

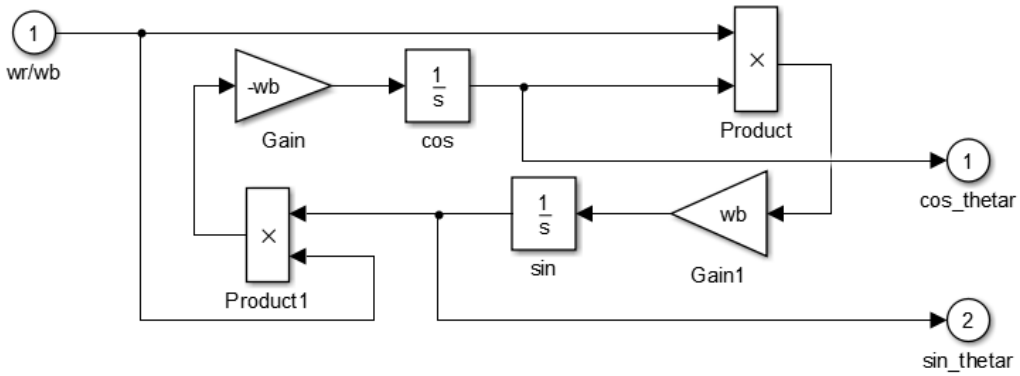

Figure 3.9: Rotor angle SIMULINK module

C. LSPMSM module

This module is the core component of the LSPMSM model. It consists of three coupled subsystem blocks: *q* and *d* modules built to calculate the motor currents and flux linkages based on Eq. (3.53) and (3.54). In addition, the rotor module has been built to calculate the motor output torque and the rotor speed based on Eq. (3.34). The built rotor modules for LSPMSM are shown in Figure 3.10.

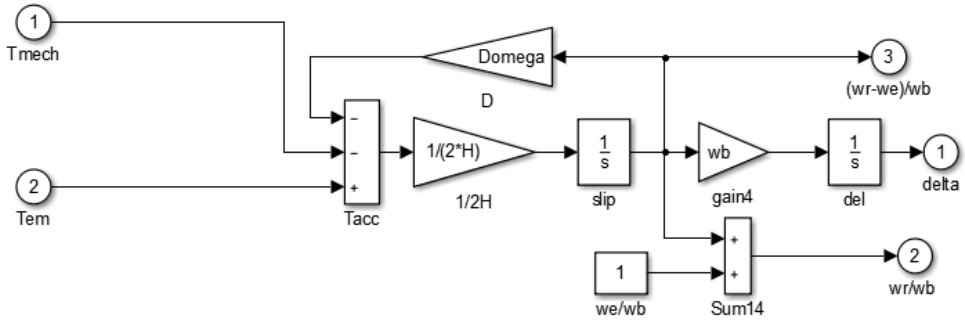

Figure 3.10: Block diagram of the rotor module

D. The *qd-abc* conversion module

This module performs the reverse operation of the *abc-qd* module based on the reverse Park's transformation described in Chapter One. The stator current in the *qd* reference frame represents the input to this module, which converts it to the natural *abc* reference frame. The output three-phase stator current is utilized in the analysis of broken rotor bar detection. Figure 3.11 shows the built LSPMSM reverse conversion module.

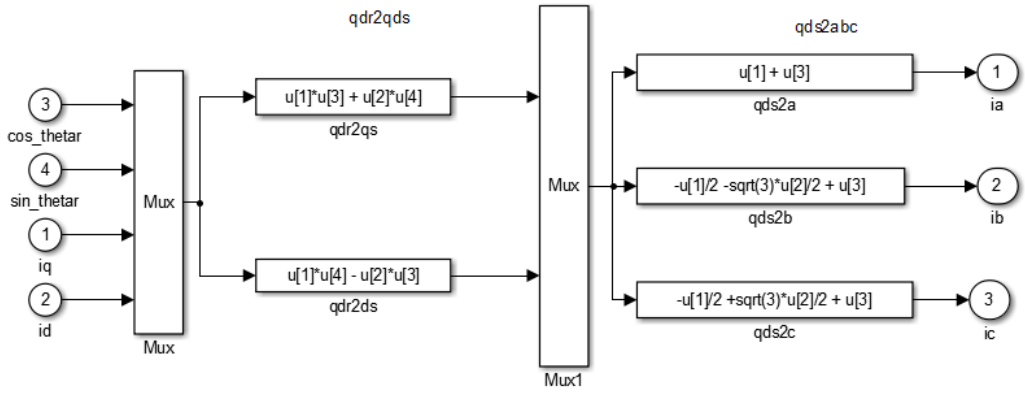

Figure 3.11: *qd-abc* reverse transformation module

CHAPTER FOUR

JMAG® BASED FEM MODELLING OF THE LSPMSM

In order to test the accuracy of the proposed mathematical model described in chapter Three and to conduct a comprehensive motor analysis, a commercial finite element based software, namely, JMAG® was used to build and simulate LSPMSM, as discussed in this chapter.

4.1 Introduction

The Finite Element Method (FEM) is a powerful numerical technique used to find approximate solutions for partial differential equations or boundary value problems. It is based on dividing a large problem into simple problems called "finite elements". The use of FEM is helpful in the design of AC machines. FEM is relatively easy to use because of its ability to import machine's geometry from the external CAD programs. In addition, the FEM has become automated to the point of being useful in modern machine design. FEM software offers flexibility in the machine geometry, boundary conditions and material properties. In order to test the accuracy of the proposed mathematical model discussed in the previous chapter, an advanced design tool based on FEM with a high level of accuracy is required [81]. In this work, a finite element based software, namely, JMAG® was used. JMAG® was originally released in 1983 as a highly competitive electromagnetic design software superior to other alternatives such as Magsoft®, Infolytica® and ANSYS®

Maxwell [82]. It is based on converting the conceptual design to a comprehensive analysis with a high accuracy in evaluating complex physical phenomena. In addition, it contains an extensive material database with more than 700 data items, including electromagnetic steel sheet, soft magnetic composite, permanent magnets and any other user-defined items. Moreover, JMAG package includes a set of applications that can be used in design and analysis [83]. Figure 4.1 shows the product structure and the different uses that could rely upon the development and analysis process.

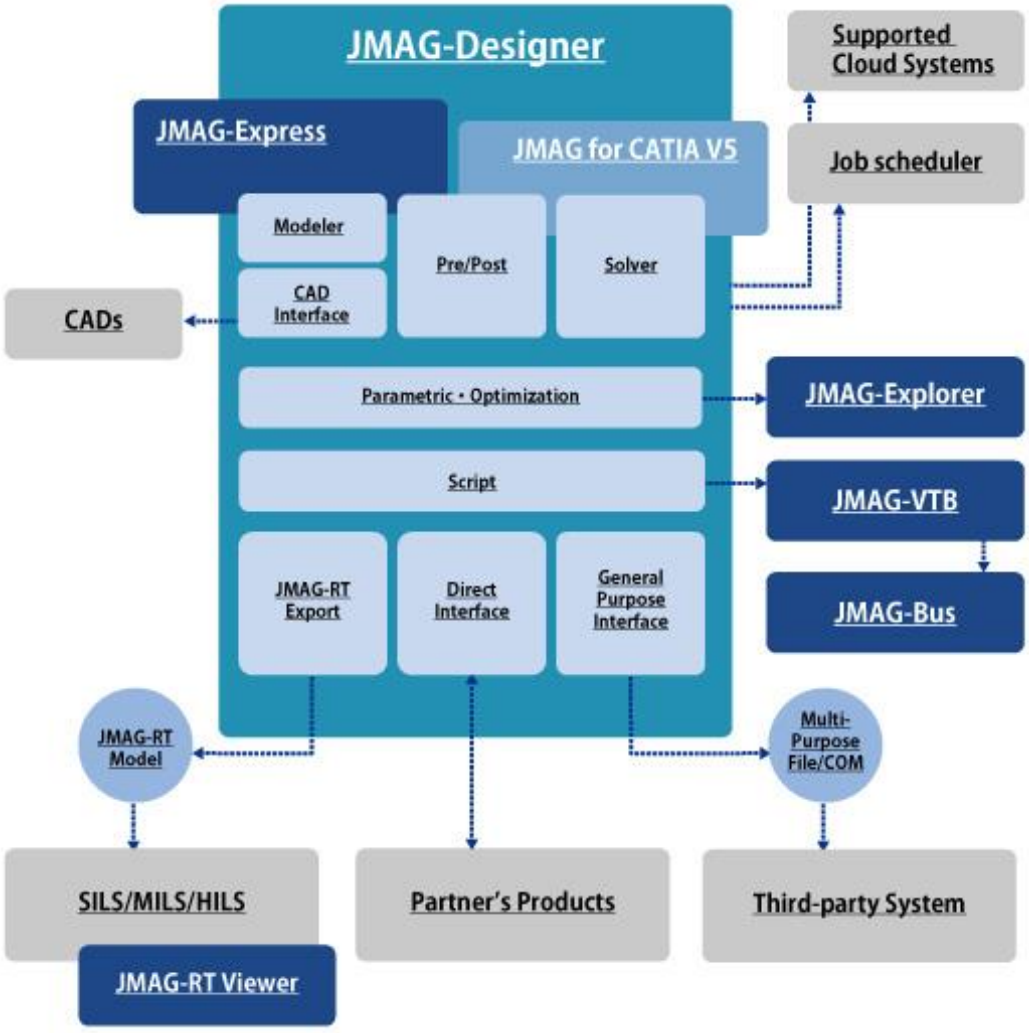

Figure 4.1: JMAG package structure [82]

4.2 FEM model of three-phase LSPMSM

In order to model LSPMSM using JMAG software, there are some steps to follow as shown in Figure 4.2.

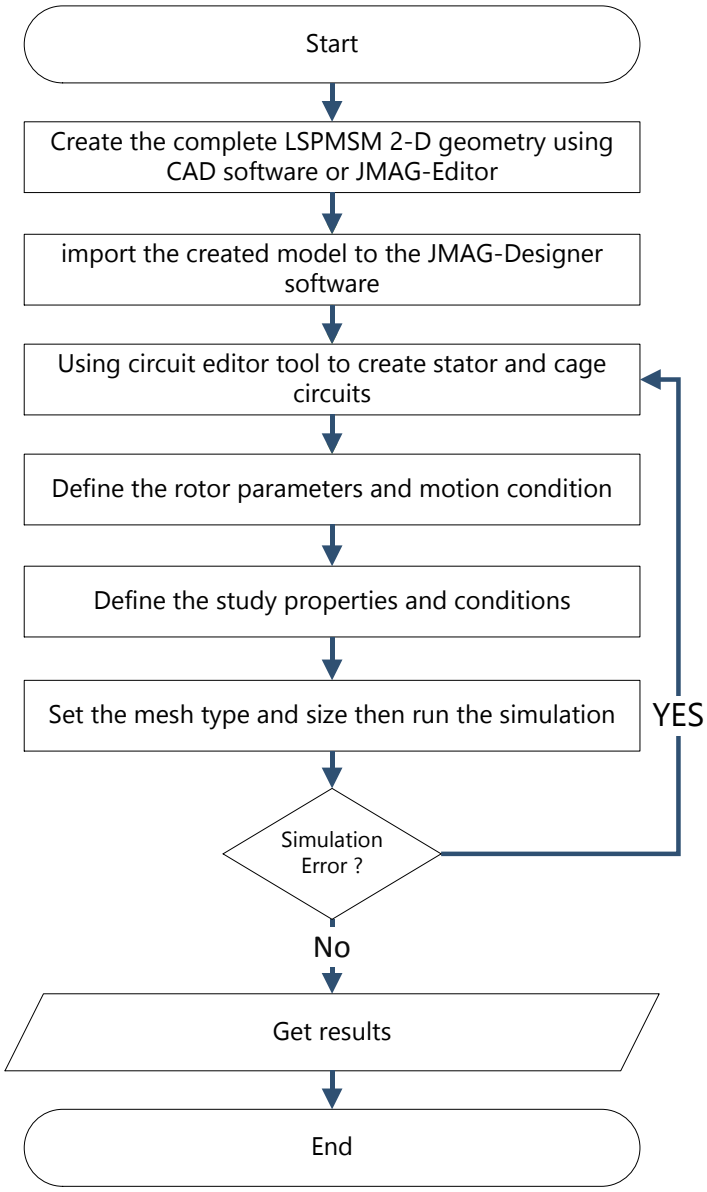

Figure 4.2: Design methodology using JMAG software

When designing LSPMSM based on JMAG® or any other FEM software, a complete 2-D structure of the motor, known as a motor geometry, should be created first. JMAG® software used in the present study provides multiple options for specifying the motor geometry, in addition to performing detailed calculations based on the finite element approach. The JMAG® functionality also allows the user to import geometry files from multiple third-party CAD software tools, such as SolidWorks®, CATIA® and AutoCAD®, or by using the built-in editor [84]. Figure 4.3 shows the 2-D structure of the present LSPMSM, generated using AutoCAD® software.

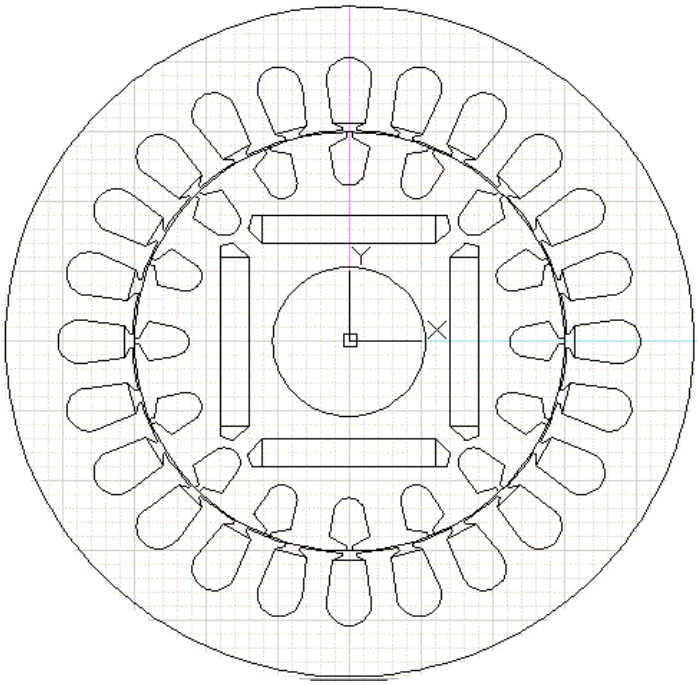

Figure 4.3: 2D - structure of the present LSPMSM

After exporting the 2-D geometry of the motor to the JMAG® designer, the materials for the permanent magnets, rotor and stator cores are selected from the available categories, namely electrical steel, soft magnetic materials and isotropic materials. The "*B-H*" curve

is determined for the selected magnetic materials, including the steel magnetic material for PMs and the rotor shaft. Non-magnetic materials are also assigned for the coils, that is, copper for all three-phase stator coils, and aluminum for the rotor cage (bars and end rings). The properties of the other mechanical and electrical materials employed in the design, such as the electric permittivity and conductivity, material density, thermal conductivity and specific heat, are also defined.

In order to create the electrical circuits for the stator and rotor cage, the built-in circuit editor tool is used. Circuit editor allows the user to set the connections of the windings, supplying the stator windings by a three-phase power source, as well as specify number of turns and layers, and the resistance for each phase coil [85, 86]. Figure 4.4 shows the LSPMSM electrical circuit designed and implemented as a part of the present study.

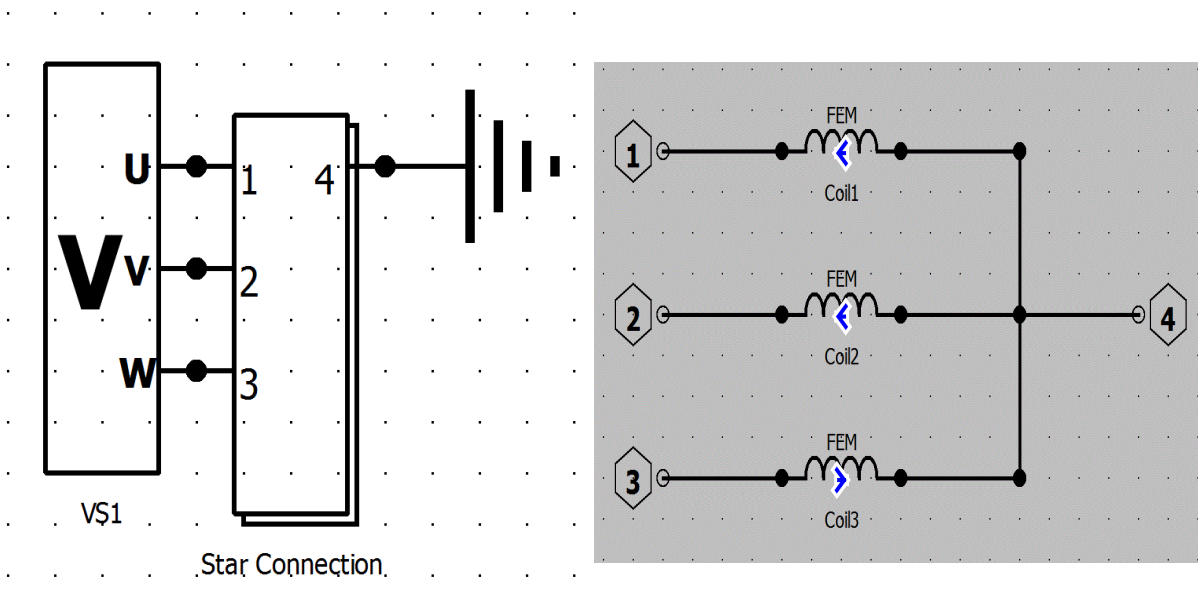

Figure 4.4: LSPMSM electrical circuit

In the next step, the geometry conditions for each motor part are determined. More specifically, the condition of rotation is specified for all rotor elements, such as the shaft, rotor magnetic core and the cage bars. The boundary condition of the periodic rotation are applied with 180 periodic angle degrees. Moreover, the torque exerted on the rotor core required specifying the rotation axis and the nodal force condition. Moreover, the geometry graphics of the stator windings and rotor bars should be linked to the corresponding electrical circuits created in the previous step, in addition to determining the current directions. This allows the FEM conductor condition to be created for the rotor bars, specifying the number of the bars arranged around the rotor in the full circle (360 degrees).

In the final step of the modeling process using JMAG®, the case studies are created, along with specifying their properties, such as the number of simulation steps and precision, FEA calculation method and the maximum number of iterations. Before starting the analysis in JMAG® designer, a mesh is generated by setting the element size, faces, skin depth, mesh type (slide mesh for motion), air region scale and symmetry boundary conditions.

However, JMAG® designer allows the user to expand the study and analysis, as an unlimited number of case studies can be created [87] . For broken bars fault analysis, a study must be created each time the number of broken bars is changed, while the software permits inclusion of multiple loads in the same study. The generated results include phase resistances, inductances, torque, current, speed, efficiency, copper losses, iron losses and torque constant. The final model of the LSPMSM developed as a part of the present study and the mesh utilized for further analysis are shown in Figure 4.5 (a) and (b), respectively.

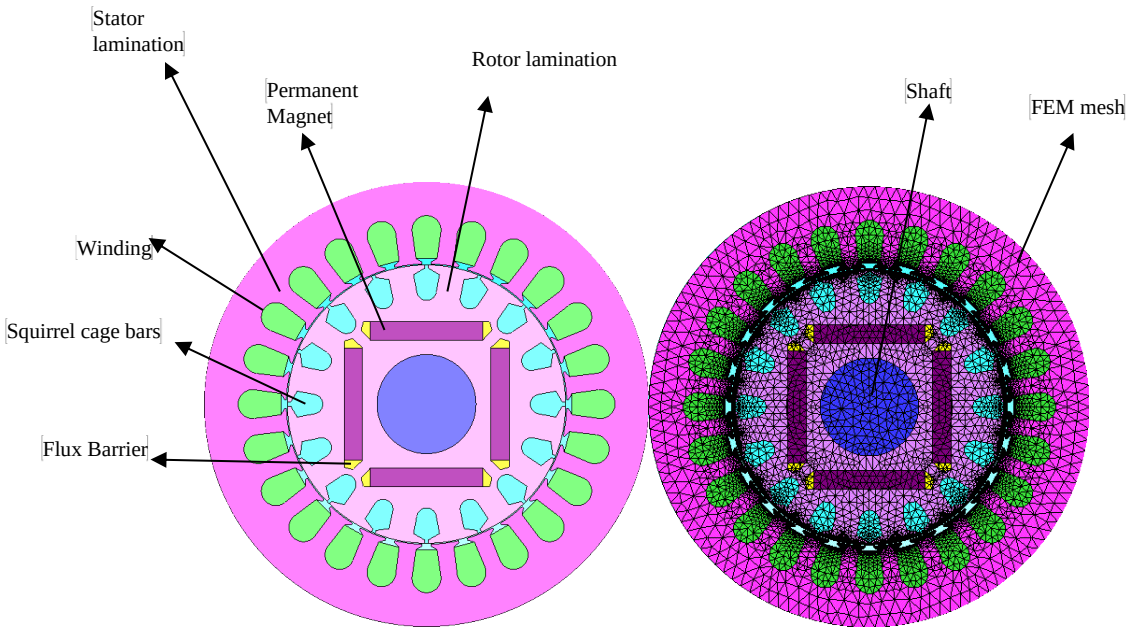

Figure 4.5: LSPMSM model using JMAG software

a) 2-D structure of the motor **b) FEM mesh used for analysis**

In order to include the effect of the fault arising due to broken bars in the rotor design, the cage circuit should be edited by eliminating the affected bars from the rotor cage. Figure 4.6 shows the cage circuit with three broken bars.

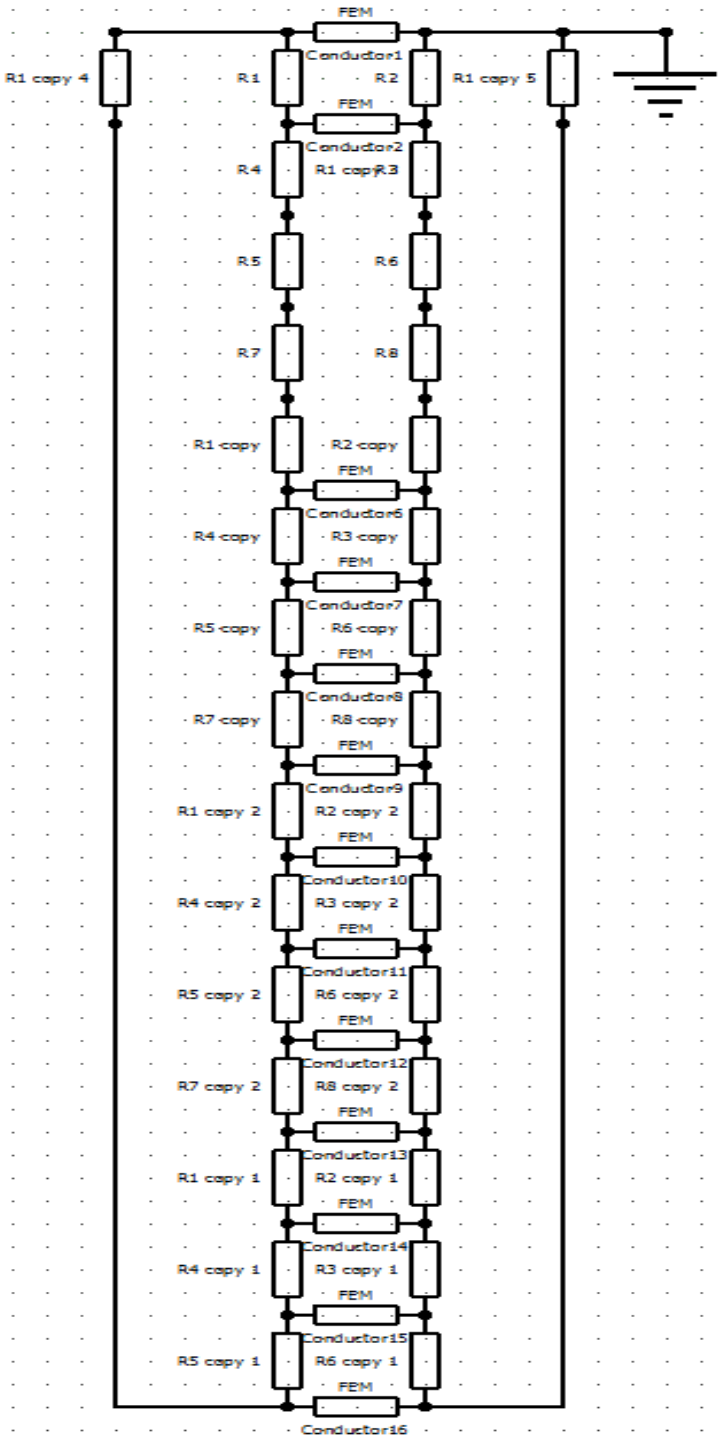

Figure 4.6: LSPMSM cage circuit with 3 broken bars

4.3 JMAG® and MATLAB® Simulation results

To simulate LSPMSM in Simulink, all parameters are initialized, and all simulation conditions are set up using MATLAB® m-file scripts. The inputs to the LSPMSM model are the three phase supply voltage, the load torque and the number of broken bars, where zero broken bar means that the motor is working in healthy state. The outputs are the three-phase stator currents, the motor rotating speed and the resulting electromechanical torque. However, both the number of broken bars and the machine load can be easily changed to any desired values. To investigate the effectiveness of the developed mathematical model, a 415V, 4-hp, 4-pole, 50Hz, 3-phase LSPMSM has been used. The motor's data are given in Table 4.1.

Table 4.1: LSPMSM electromagnetic design

Parameter	Value
Rated Power (W)	750
Rated Voltage (V)	415
Stator phase resistance (Ω)	19.15
Number of poles	4
Frequency (Hz)	50
Air-gap length (mm)	0.3
Outer/inner stator diameter (mm)	120/75
Number of stator slots	24
Number of rotor bars	16
Axial length of stator core (mm)	75
Number of turns per slot	139
Height of stator yoke (mm)	45
Height of stator/rotor slots (mm)	13/9.5
Remnant of magnet (T)	1.02

On the other hand, Once the JMAG analysis is completed, the calculation folder will be available and various graphs can be displayed, such as the magnetic flux produced by the coils, rotational velocity, torque, current and electric power. Simulation of an LSPMSM under healthy and broken bar conditions will be discussed using the proposed mathematical model and JMAG® model. Figure 4.7− Figure 4.12 show a comparison of the stator phase current, torque and rotor speed of the healthy motor under no load and 1.5 NM loading levels, respectively. As it can be seen from the graphs, the time required to achieve synchronism is ~ 0.3 s and 0.4 s, at no load and 1.5 NM load, respectively. The same trend can be noted at higher loading levels, where the synchronous time increases with the loading level, until motor synchronism ceases beyond a particular rating load, as shown in Figure 4.13.

Simulations for the healthy and faulty motor under different loading levels indicate a very good agreement between SIMULINK® and JMAG® models. The difference between the results yielded by the two models arises due to the assumptions used in each one. For example, in the SIMULINK® model, the current of the broken bar is assumed to be zero, while some current paths through laminations between adjacent bars are assumed to exist in the JMAG® model. In addition, it is difficult to obtain the exact value of the resistance, mutual inductance and self inductance of the aluminum conductors used in JMAG® to represent the rotor bars in MATLAB®. These differences may also occur due to the mathematical operations, as the SIMULINK® and JMAG® simulations employ different solvers.

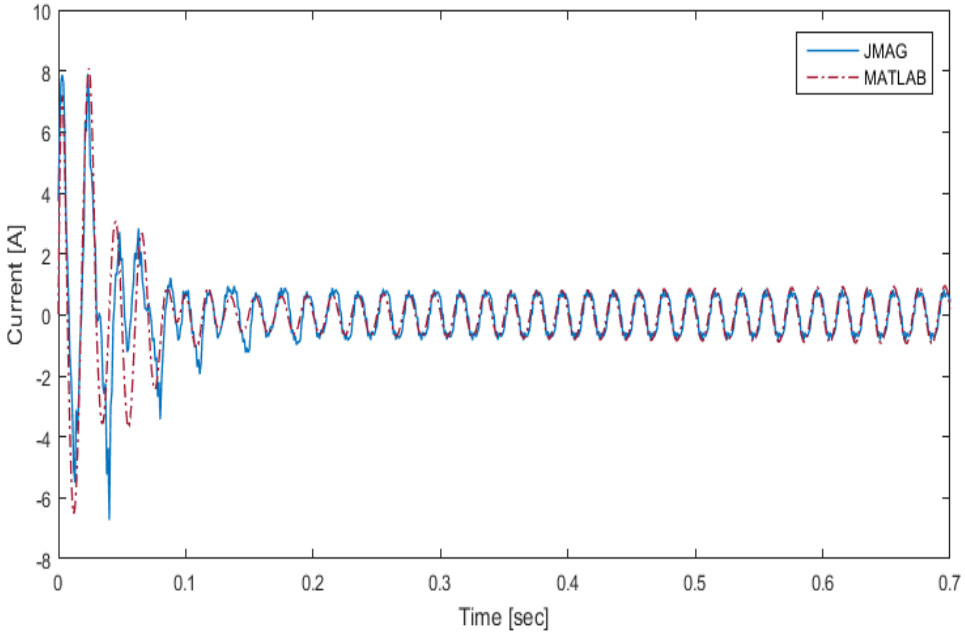

Figure 4.7: MATLAB and JMAG simulations of a healthy LSPMSM stator current at no load

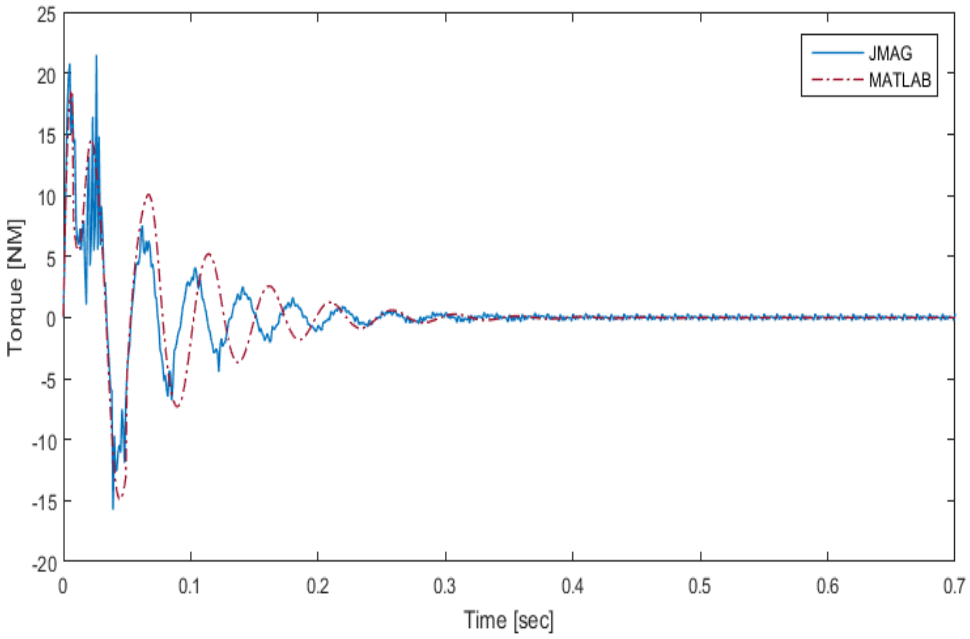

Figure 4.8: MATLAB and JMAG simulations of a healthy LSPMSM torque at no load

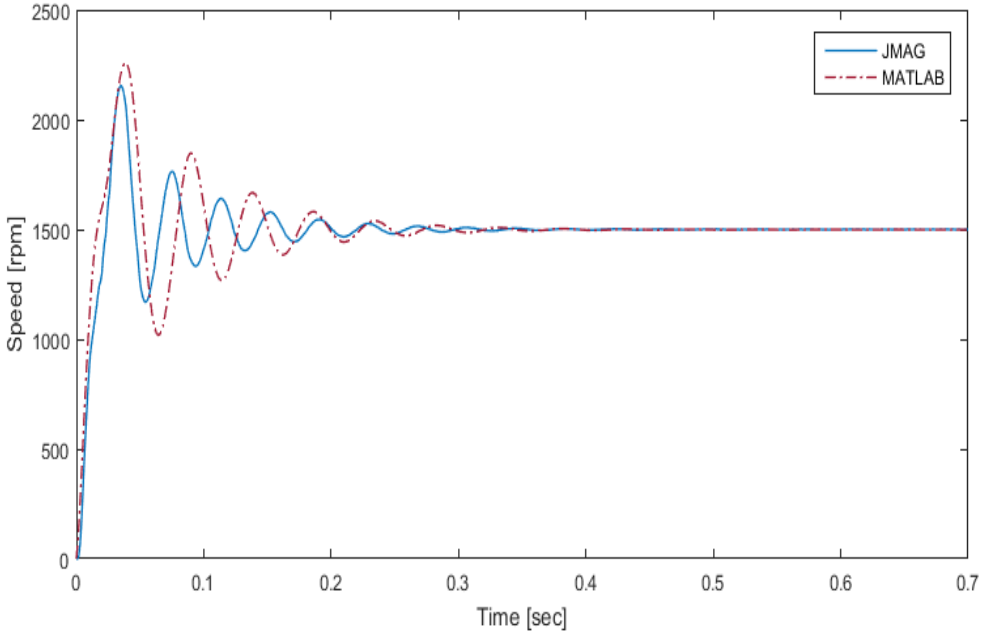

Figure 4.9: : MATLAB and JMAG simulations of a healthy LSPMSM rotor speed at no load

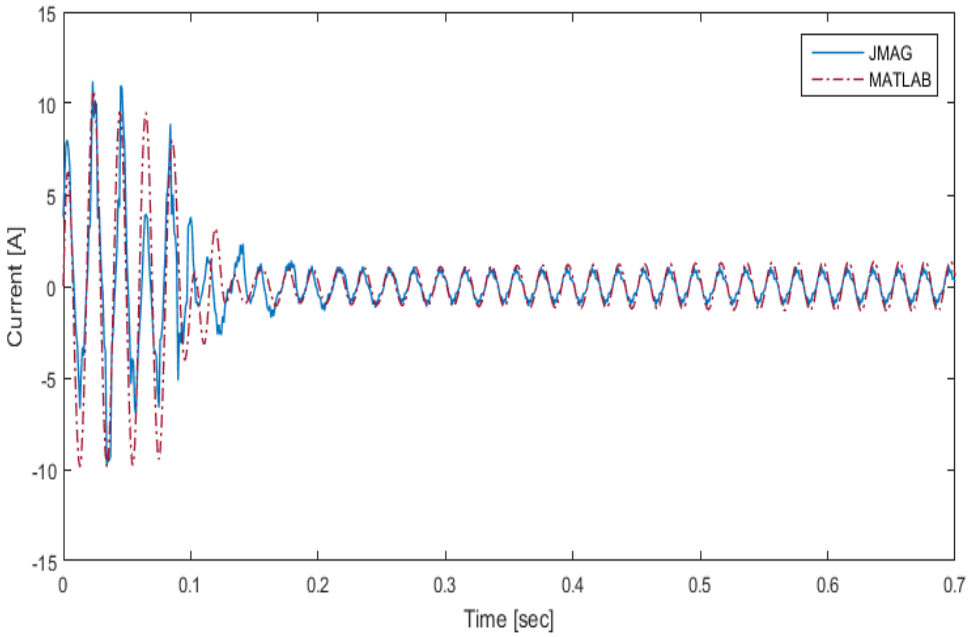

Figure 4.10: MATLAB and JMAG simulations of a healthy LSPMSM stator current at 1.5NM load

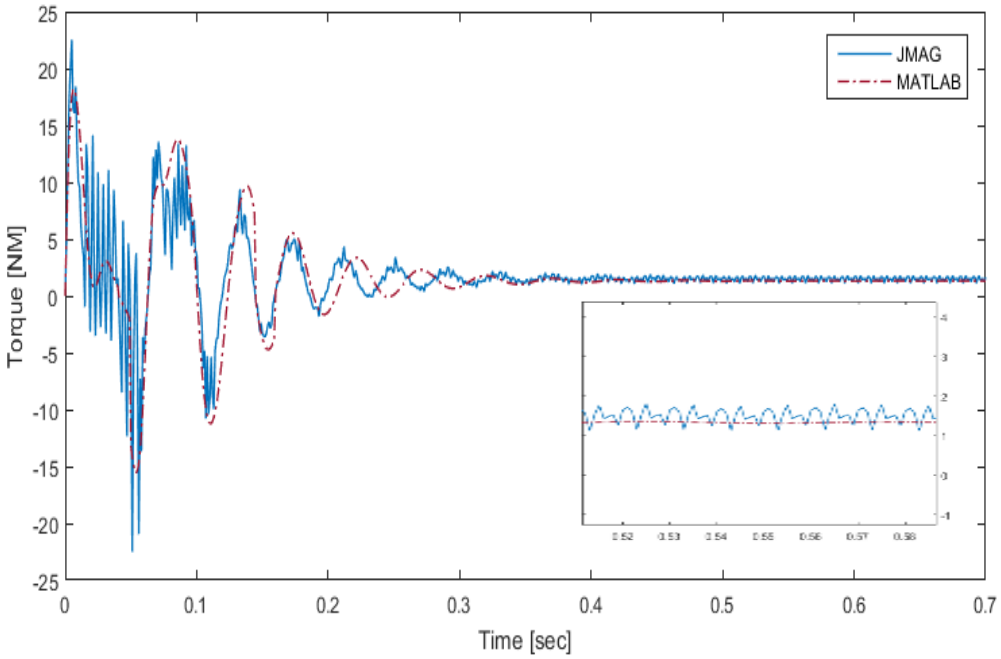

Figure 4.11: MATLAB and JMAG simulations of a healthy LSPMSM torque at 1.5 NM load

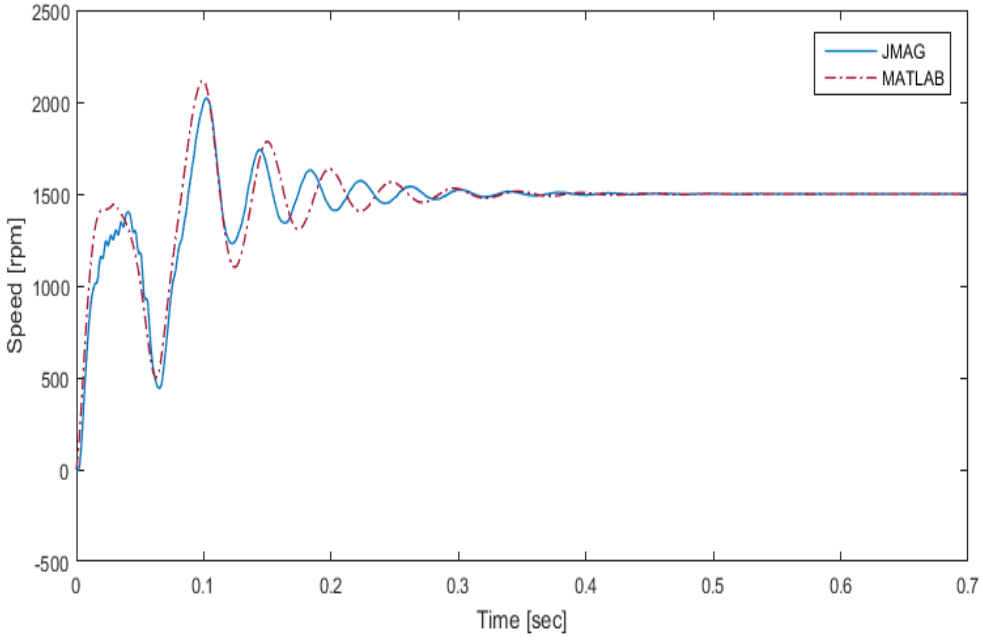

Figure 4.12: MATLAB and JMAG simulations of a healthy LSPMSM rotor speed at 1.5 NM

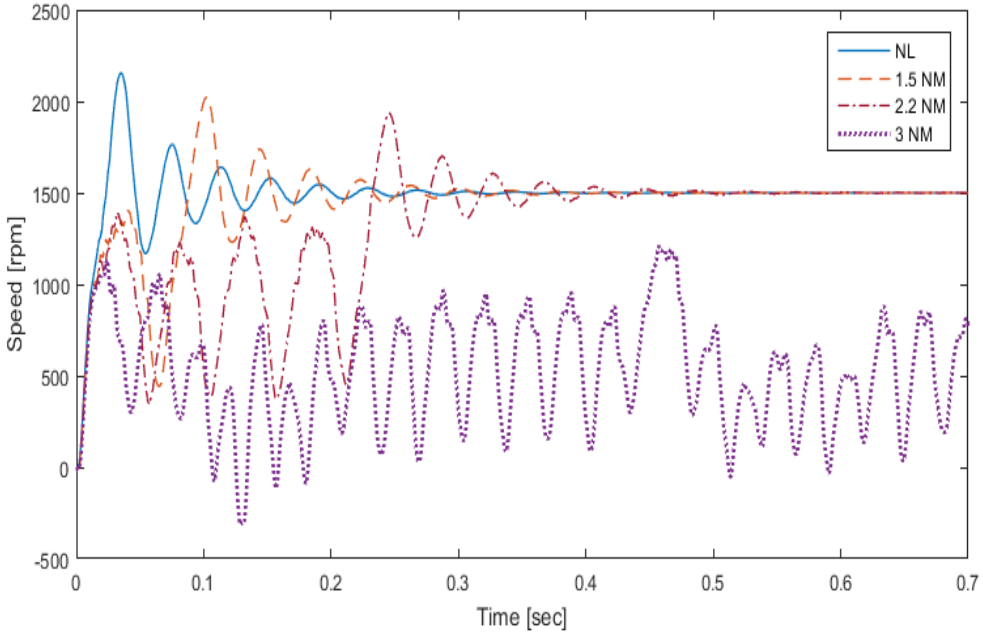

Figure 4.13: Simulation results of healthy LSPMSM rotor speed under different loading levels

The effect of the broken bar conditions on the motor performance has been investigated. Figure 4.14 to Figure 4.16 show the stator current, torque and rotor speed for the case of three broken bars at 1.5 NM loading level, where time required to achieve synchronism increases to 0.45 s, as compared to 0.4 s for the healthy motor. However, a proportional relation between the number of broken bars and the transient time can be noted, as will be discussed later in this chapter.

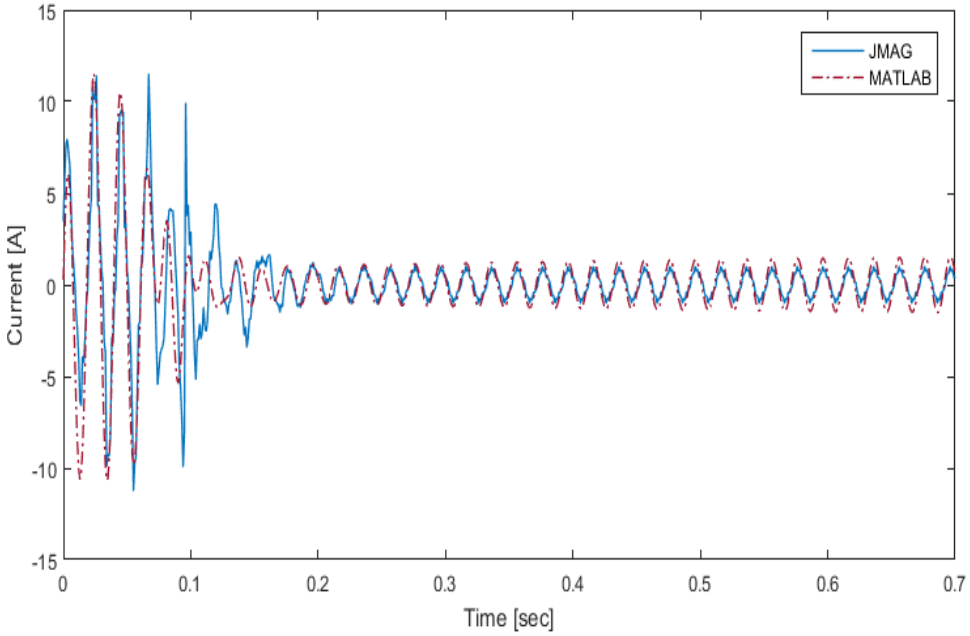

Figure 4.14: MATLAB and JMAG simulations of a faulty with 3 broken bars LSPMSM stator current at 1.5 NM load

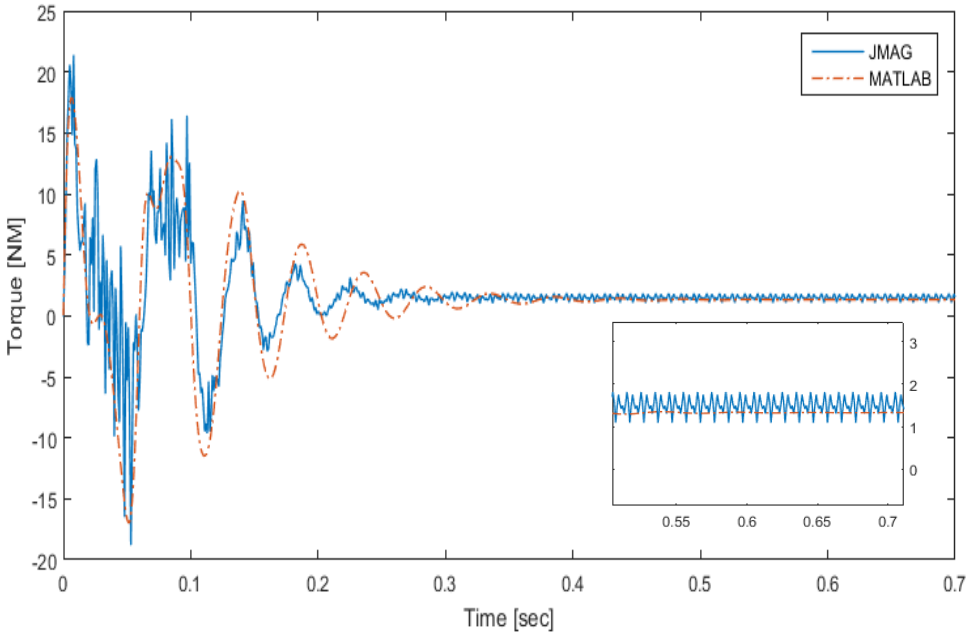

Figure 4.15: MATLAB and JMAG simulations of a faulty with 3 broken bars LSPMSM torque at 1.5 NM load

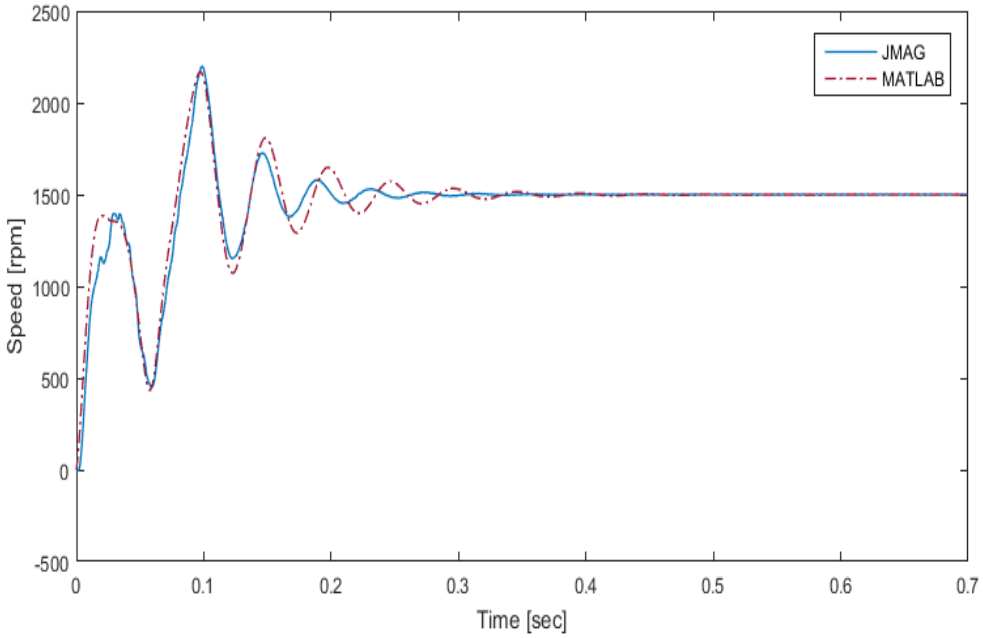

Figure 4.16: MATLAB and JMAG simulations of a faulty with 3 broken bars LSPMSM rotor speed at 1.5 NM load

However, the results show a very good agreement between the proposed model and the JMAG® simulations. In order to verify the accuracy of the proposed model, results of two error measurements are shown in Table 4.2. Root mean square error (RMSE) and percentage of the normalized mean square error (%NMSE) are used to measure the error in the simulated stator current signal coming from the proposed model and JMAG model under different loading values and broken bar numbers. As can be seen from the findings presented in Table 4.2, the average error value of the calculated RMSE and the percentage of the NMSE are 1.78 and 3.7%, respectively. The error measurement tools that used in this work can be defined as follows:

$$RMSE = \sqrt{\frac{\sum_{i=1}^{N}(x_i - y_i)^2}{N}}$$

$$\%NMSE = \frac{\sum_{i=1}^{N}\left(\left(\frac{x_i}{max(x)}\right) - \left(\frac{y_i}{max(y)}\right)\right)^2}{N} \times 100\% \quad \textbf{(4.1)}$$

where x_i, y_i are the values of the JMAG® and MATLAB® simulation points, respectively, while m*ax(x), max(y)* are the maximum points in both JMAG® and MATLAB® data vectors, respectively. *N* is the number of simulation points in data vectors.

Table 4.2: Three accuracy and error measurements of JMAG® and mathematical models

Case No.	Case		Current	
	Load (NM)	No. of BRB	RMSE	%NMSE
1	0	0	1.1475	2.01014
2		1	0.9491	1.2558
3		3	1.0354	1.8216
4		5	1.2084	1.6504
5	0.5	0	1.7877	3.7296
6		1	1.0376	1.4216
7		3	1.0151	1.7238
8		5	3.1487	9.3429
9	1.5	0	0.2936	1.8363
10		1	1.3949	1.6047
11		3	1.4676	1.6223
12		5	3.4308	6.8855
13	2	0	1.2791	1.3751
14		1	1.6313	1.7881
15		3	4.1231	9.4179
16		5	3.6541	12.1881
Average			1.7878	3.7296

In addition, Figure 4.17 to Figure 4.20 show the effect of varying the number of broken bars on the torque and speed performance under no load and 1.5 NM loading. Under the no load condition, the results clearly show that, as the number of broken bars increases, so does the synchronization time, which is conserved even with five broken bars. On the other hand, under 1.5 NM loading, the synchronism is lost at five broken bars, which is approximatyely 1/3 of the total number of rotor bars. This confirms the findings reported in the literature [73].

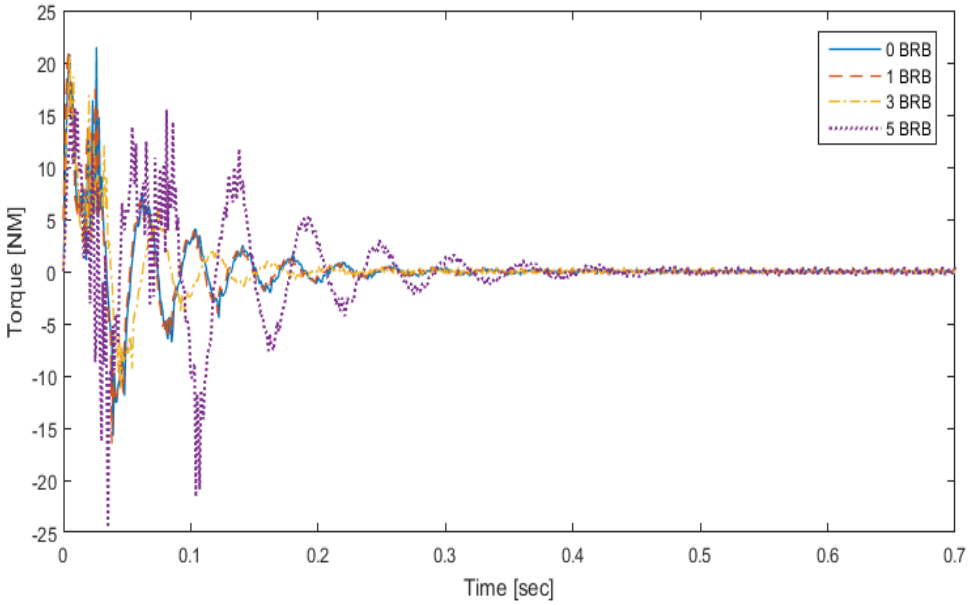

Figure 4.17: torque simulation results of a faulty LSPMSM with 0, 1, 3, and 5 broken at no load

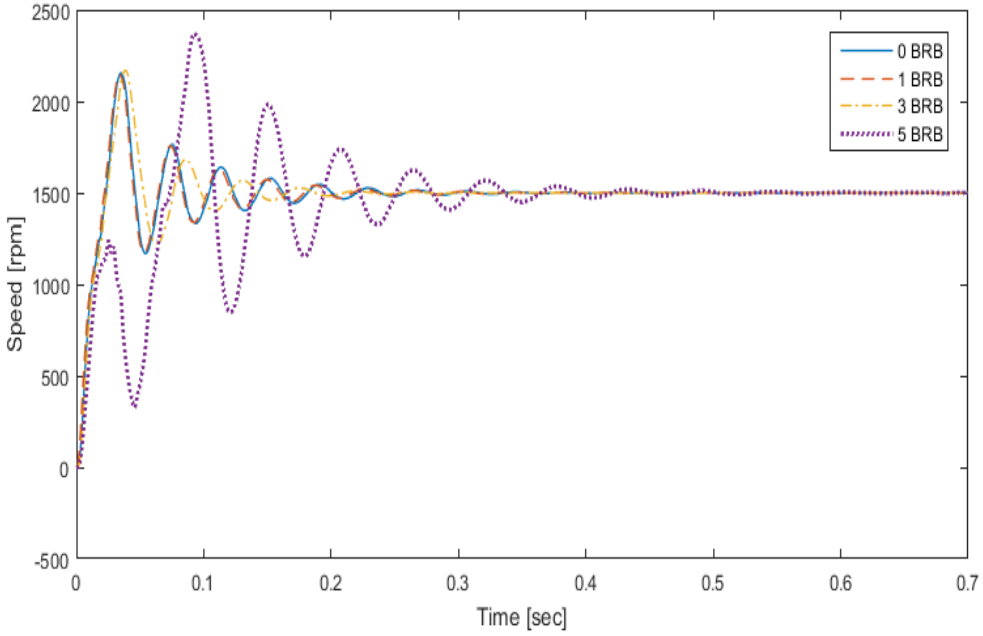

Figure 4.18: rotor speed simulation results of a faulty LSPMSM with 0, 1, 3, and 5 broken at no load

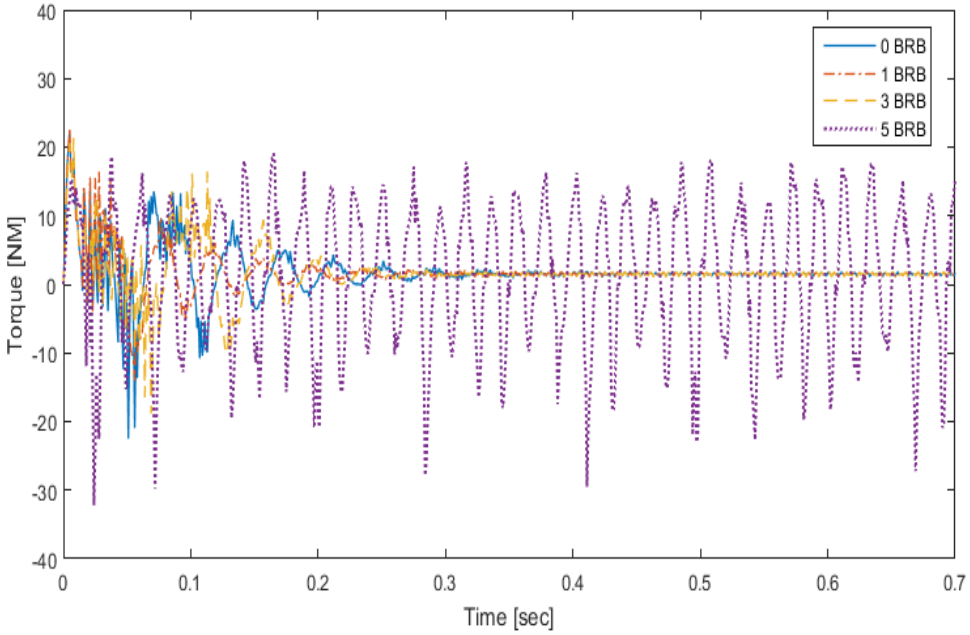

Figure 4.19: torque simulation results of a faulty LSPMSM with 0, 1, 3, and 5 broken at 1.5 NM load

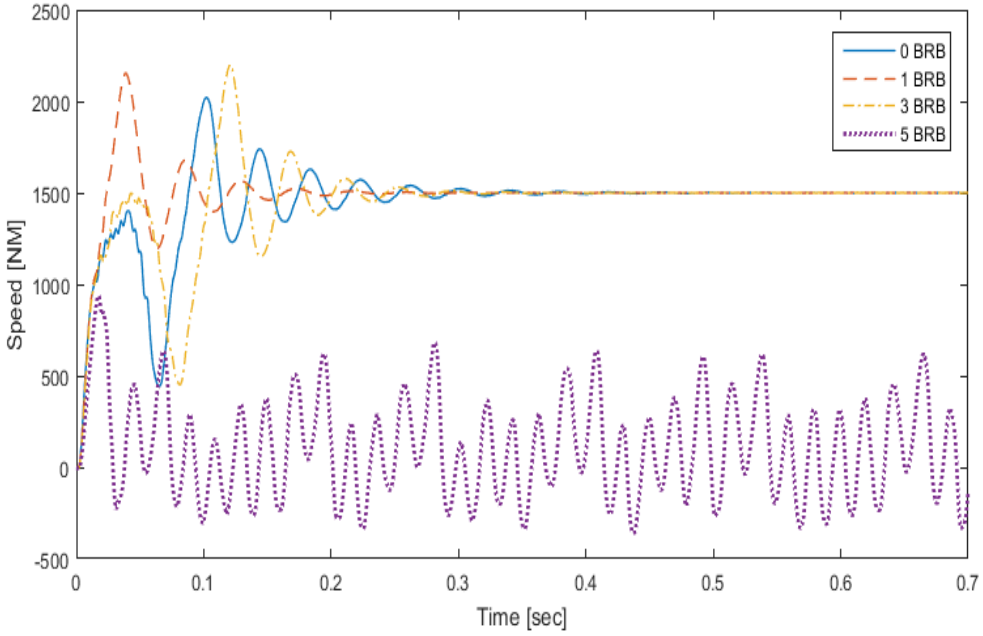

Figure 4.20: Rotor speed simulation results of a faulty LSPMSM with 0, 1, 3, and 5 broken at 1.5 NM load

Figure 4.21 shows the rotor speed at different loading levels under two broken bars condition, where the motor lost its synchronization at the 2.4 NM loading level. In order to determine at what loading level the synchronization will be lost for each number of broken bars, different simulations have been performed. The results are depicted in Figure 4.22.

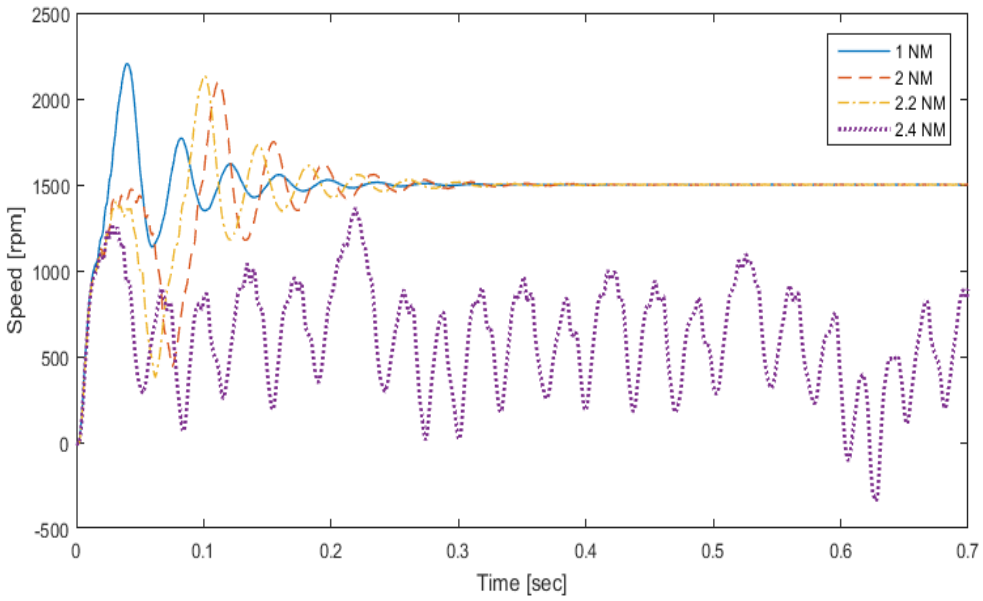

Figure 4.21: Simulation results of faulty LSPMSM with 2BRB under different loading levels

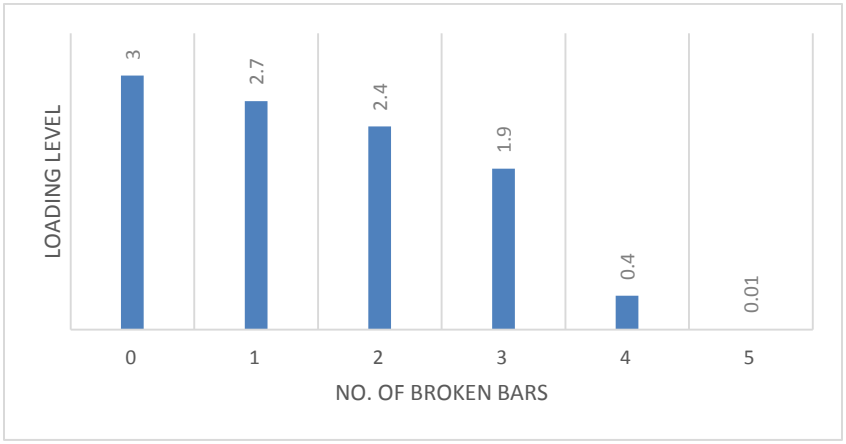

Figure 4.22: Relation between the number of broken bars and corresponding loading value that makes the motor lose synchronism

CHAPTER FIVE

PROPOSED BROKEN BAR FAULT DIAGNOSTICS ALGORITHM

In order to monitor and diagnose the occurrence of the broken bars fault in LSPMSM, a practical contribution for an automated diagnostics system using artificial neural network was built, and will be discussed in this chapter, before demonstrating its application to the designed LSPMSM.

5.1 Introduction

Diagnostics techniques for the motor failures have become a major concern and a fertile environment for scientific research. Monitoring of the motor faults is a technique used to check the health of the motor by analyzing the data collected from the running motor. Accurate monitoring and diagnosis techniques result in downtime reduction.

Artificial neural networks (ANNs) are electronic models designed based on the brain's natural structure. Neurons are the fundamental processing units of the ANNs. In biology, a neuron receives inputs from different sources, combines them in some way, performs non-linear processes on these inputs and then outputs the results [88]. Figure 5.1 shows the simple biological neuron operations, known as "nerve cell".

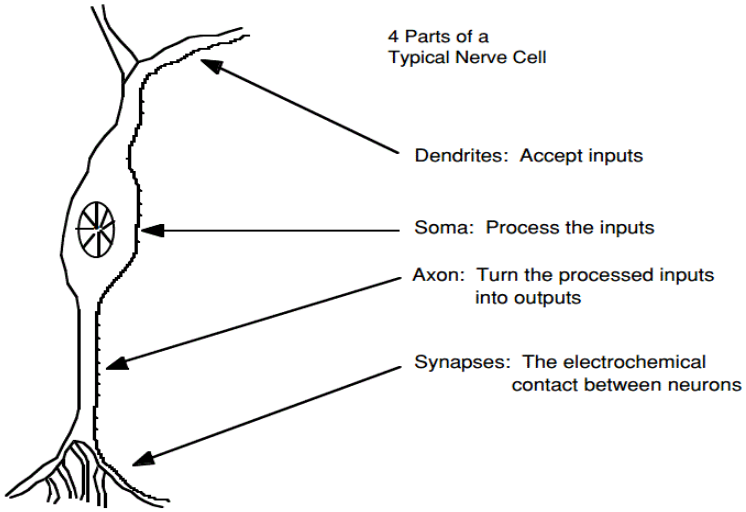

Figure 5.1: Simple biological neuron functions

Artificial neuron, also known as "processing element" simulates the basic functions of the natural neuron. Figure 5.2 shows the basic representation of the artificial neurons.

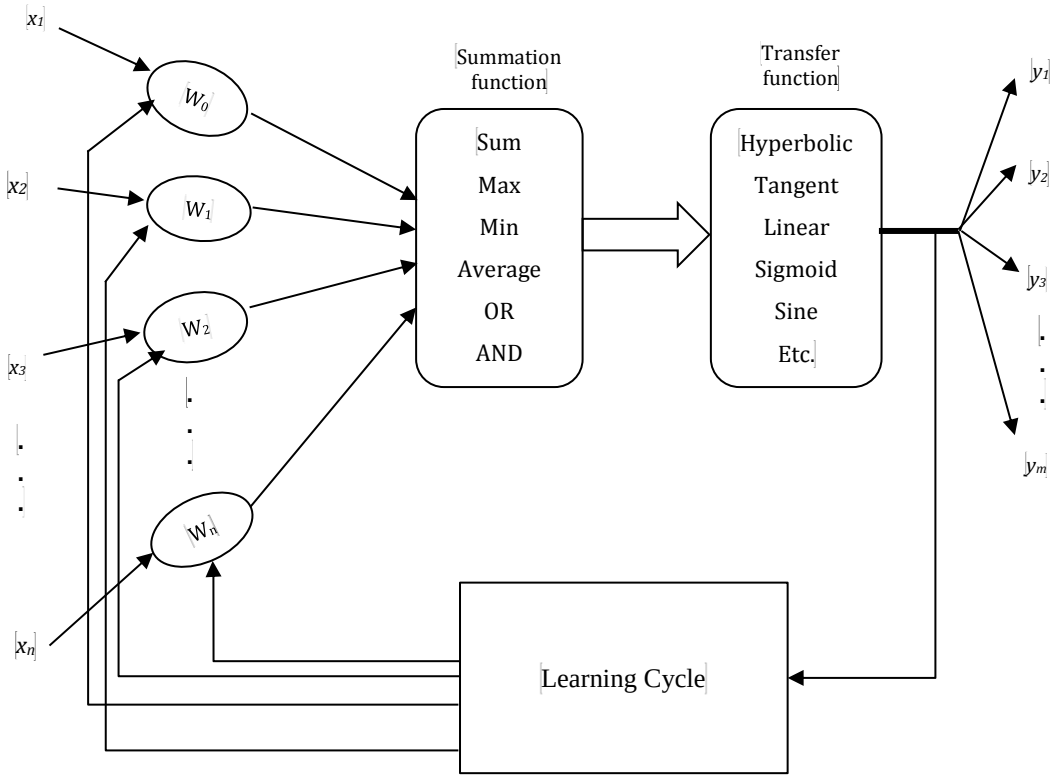

Figure 5.2: Fundamental representation of the artificial neurons

where x_i represent the inputs to the neurons. Each one of the inputs is multiplied by the connection weight w_i representing the connection strength (positive or negative). The modified inputs are forwarded to the summation function, which sums different inputs or perfors other operations such as ORing, ANDing, averaging, smallest, largest, etc. The results of the summing function are sent to the transfer function, which applies different non-linear algorithms to the incoming values to transform them into real outputs. Several transfer functions are currently used, such as sine, sigmoid, tangent, hyperbolic, etc. Finally, the artificial neuron is ready to output the results of the transfer function or input them into another level of processing elements according to the neural network structure. As ANNs represent a non-linear mapping between the inputs and outputs, the learning cycle adjusts the input weights to obtain the desired mapping. ANNs consist of a large number of interconnected processing units that are grouped at one or several levels called "hidden layers".

With the advancement in the ANNs theory, a wide range of neural networks became available, including the "Multi-layer Feed-forward Neural Network (MFNN)", "Radial Basis Function Neural Network (RBFNN)", "Support Vector Machines (SVM)", etc. The MFNN is the most commonly used neural networks with many applications in engineering and other fields. Therefore, MFNN is the neural network utilized in this study.

MFNN is formed by connecting different nodes in parallel and series to formulate a multi-layer neural network, as shown in Figure 5.3.

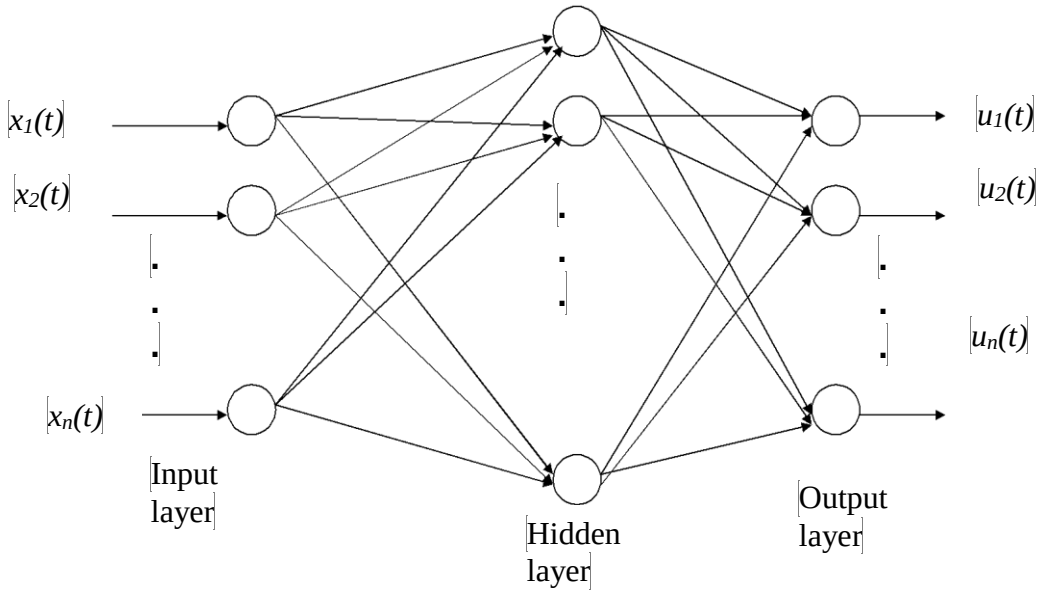

Figure 5.3: Multi-layer feed forward NN

Finally, the MFNN is trained using "back-propagation" algorithm, which aims to find the best biases that relate the optimum solution mapping inputs to the desired outputs along the negative gradient of the cost function *J* described in the next section.

5.2 Artificial neural network training

Once the ANN has been structured, that network should be trained for a particular application. The weights are chosen randomly before commencing the training process. Supervised and unsupervised training are two commonly utilized training approaches. Supervised training requires providing the network with the desired outputs before and during the training process. The network compares the hidden layers outputs with the provided outputs and adjusts the weights through the feedback circuit. The system terminates at the desired accuracy point. However, sometimes NNs fail to converge since

the input does not contain enough data to enable a complete learning process. During the learning process, feedback algorithms known as “backward error propagation” are working to adjust the input weights. In unsupervised or adaptive learning, the network is provided with the inputs but not with the desired outputs. The system has the ability to determine adaptively the suitable features that should be used to group the input data. This process is known as “self-organization” or “self-adaption”. Presently, this type of training is not well understood, and thus generally reserved for robot design, where it helps the robots understand new environments [88]. Therefore, a supervised learning approach was used in this thesis.

The NN learning rate depends on several factors, such as the used learning algorithm. Moreover, there is a trade-off between the learning time and the accuracy of the output results. A slower training rate achieves better accuracy than the faster training rate, but requires dedicating more time to the learning process. However, in most of the simulation tools, the learning rate ranges from zero to one. If the learning rate is greater than one, it is easy for the training algorithm to adjust the weights, but the network will oscillate. Generally, it is better to choose a positive small step-sized learning rate to obtain more accurate results, even if this mandates longer simulation time. In order to train the network, the initial weights are randomly chosen. Then, the back propagation algorithm is applied to update and adjust the hidden layers weights iteratively. The error between the desired output and the network output is limited. However, Mean Square Error (MSE) is always used in ANNs, which can be defined as follows [88]:

$$MSE = \frac{1}{K}\sum_{i=1}^{K}\left(t_i - a_i\right)^2 \qquad \textbf{(5.1)}$$

where K is the number of output points, t_i is the desired output and a_i is the network output.

5.3 Effects of rotor asymmetry on the LSPMSM

Under normal operating conditions, the positive sequence of 3-phase balanced stator current produces a non-zero forward-rotating field in the air gap of the motor. This forward-rotating field induces currents in the rotor bars and end connectors. These induced rotor currents then produce forward and backward rotating fields in the air gap of the motor. For a symmetrical rotor, the resultant of the backward-rotating fields is zero, while the resultant of the forward-rotating field is non-zero. However, under any abnormal condition that destroys the symmetry of the rotor, a different scenario with regard to the backward-rotating fields arises. In this case, the resultant of the backward-rotating fields is no longer zero. It is the ultimate identification of the effects of this non-zero backward-rotating field that forms the basis for most motor current signature analysis monitoring techniques. In other words, when a rotor bar is broken, no current flows in that bar. The resulting asymmetry in the rotor results in a non-zero backward-rotating field that rotates at a speed with respect to the rotor. This non-zero backward-rotating field induces harmonic currents in the stator winding which are superimposed on the stator winding currents [60, 24]. Consequently, stator current signature is considered as a distinguishing primitive attribute or characteristic of the faulty motor under broken bar condition. Many methods can be applied on the stator current signature to obtain a Milestone that highlights the differences between current signatures under different number of broken bars and at different loading levels. Such methods consist of statistical features such as Sum and Mean, and linear algebra based features such as singular value decomposition (SVD). However, since the

broken bars fault affects the current signals over time, then it is preferable to deal with the stator phase current signature in time domain. In this thesis, Sum, Mean and SVD methods will be applied on the stator phase current in order to get the sub-optimal distinguishing milestones of the broken bars fault effect.

5.4 Effects of the feature type, number of neurons, window size and training algorithm on the NN performance

In order to achieve the best NN performance for diagnosing the broken bars fault condition, different NN algorithms and number of neurons as well as window sizes and types of features were tested.

5.4.1 The effect of the feature type and window size

Different distinguishing attributes were applied on the stator current signatures to obtain the best feature for broken bar fault diagnosis. Such attributes are the sum, mean and SVD of the current windows.

A. Sum and mean of the matrices

The Sum/Mean of the matrices in MATLAB® returns a column vector containing the sum/mean of each row, as shown in Figure 5.4 .

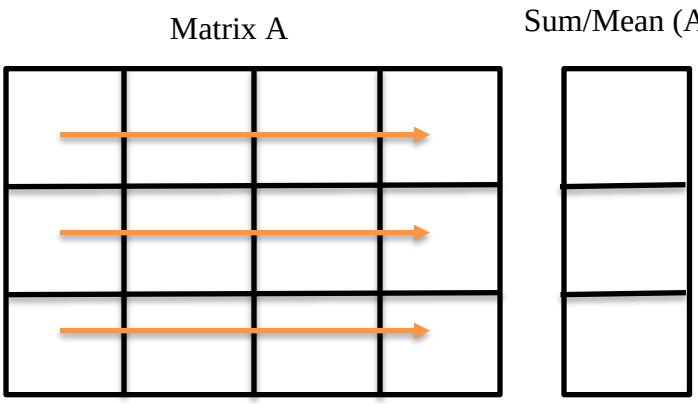

Figure 5.4: Representation of Sum/Mean of matrices in MATLAB®

B. Singular Value Decomposition (SVD)

Singular value decomposition (SVD) is one of the important mathematical tools in linear algebra, which can be used to factorize a matrix into a multiplication of three different matrices, one of which is a diagonal matrix D and the other two are unitary orthogonal vectors U and V. Therefore, SVD can be applied on the current signatures matrix in order to obtain some useful features by factorizing the whole matrix into three matrices, each with specific properties. The singular value decomposition of the current signatures matrix *Y* can be described as follows:

$$Y = UDV^T \quad \textbf{(5.2)}$$

where Y is $m \times n$ rectangular matrix, and U and V are $m \times m$ and $n \times n$ orthogonal matrices, respectively. D is $m \times n$ diagonal matrix, where the diagonal entries are the singular values of the matrix Y. These singular values are arranged on the diagonal in descending order ($\sigma_1 \geq \sigma_2 \geq \sigma_3 \geq \ldots \geq \sigma_n$), where σ_i denotes the diagonal entries, $i \in \{1, 2, 3 \ldots \text{smaller } (m,n)\}$. Therefore, using the SVD concept, matrix Y can be written as follows:

$$\begin{bmatrix} y_{11} & \cdots & y_{1n} \\ \vdots & \ddots & \vdots \\ y_{m1} & \cdots & y_{mn} \end{bmatrix} = \begin{bmatrix} u_1 & u_2 & \cdots & u_m \end{bmatrix} \begin{bmatrix} \sigma_1 & 0 & \cdots & 0 \\ 0 & \sigma_2 & 0 & 0 \\ \vdots & 0 & \ddots & \vdots \\ 0 & 0 & \cdots & \sigma_n \end{bmatrix} \begin{bmatrix} v_1^T \\ v_2^T \\ \vdots \\ v_n^T \end{bmatrix} \quad \textbf{(5.3)}$$

The Eigenvalues of the matrix Y are unique and can be calculated by taking the square root of $YY^T = Y^T Y$. The matrices U and V are not unique and can be assigned as an Eigenvector of YY^T and $Y^T Y$, respectively. In addition, the rank of the matrix Y is equal to the number of the non-zero Eigenvalues.

The current window size also affects the network accuracy. Table 5.1 shows different trials aiming to obtain the sub-optimal feature at different window sizes and with different numbers of neurons using a fixed training algorithm (Bayesian algorithm). The best network accuracy was obtained at five windows for each stator current with 2500 data points for each, and with 11 hidden layer neurons using the SVD feature.

Table 5.1: NN training using three types of features

Case No.	Features extraction method	(Window size, No. of points/window)	No. of neurons	Testing samples MSE	Testing samples Regression
1	Sum	(5,2500)	5	3.76500	0.46328
2			9	6.55271	-0.636698
3			11	4.22735	-0.709506
4			12	4.40155	-0.558440
5			15	1.77605	0.490217
6			20	6.20473	-0.524491
7		(10,1250)	5	2.39131	0.807816
8			9	3.24900	0.490255
9			11	3.64945	-0.200092
10			12	7.32567	-0.229587
11			15	2.78593	-0.713948
12			20	1.69498	-0.114133
13		(20,625)	5	4.17294	-0.627644
14			9	3.84050	-0.157548

15			11	3.57191	-0.384294
16			12	4.99474	-0.272242
17			15	1.55964	0.932602
18			20	2.52811	0.313968
19		(25,500)	5	1.82510	-0.587290
20			9	5.65821	0.626550
21			11	0.383621	0.883548
22			12	2.97749	-0.906125
23			15	1.02792	0.927045
24			20	1.27937	0.874362
25	Mean	(5,2500)	5	3.26885	-0.479942
26			9	2.99073	0.756430
27			11	6.35119	-0.669424
28			12	3.28986	-0.829401
29			15	3.32332	0.181476
30			20	0.948546	0.477511
31		(10,1250)	5	4.89721	-0.699306
23			9	0.898294	0.711394
33			11	4.41087	-0.409144
34			12	3.19980	-0.703091
35			15	4.15857	-0.484717
36			20	3.86593	0.426759
37		(20,625)	5	4.07961	-0.520319
38			9	2.101075	0.2567766
39			11	5.94870	-0.757072
40			12	4.01130	0.0110814
41			15	4.16682	0.187040
42			20	4.83346	-0.556993
43		(25,500)	5	1.77371	0.668976
44			9	1.94631	0.433167
45			11	5.06980	-0.640934
46			12	4.11245	-0.907704
47			15	1.55670	0.750623
48			20	3.31612	0.883376
49	SVD	(5,2500)	5	8.17577e-2	0.984566
50			9	0.530589	0.967486
51			11	4.58467e-3	0.99266
52			12	0.846713	0.900062
53			15	0.600628	0.926761

54		(10,1250)	5	1.40555	0.755602
55			9	0.113877	0.992901
56			11	0.842064	0.854919
57			12	0.243494	0.982903
58			15	0.827255	0.850975
59		(20,625)	5	0.572729	0.968345
60			9	0.493744	0.953185
61			11	0.964008	0.866366
62			12	0.532925	0.928532
63			15	0.719404	0.896085
64		(25,500)	5	0.738655	0.894466
65			9	0.977169	0.751925
66			11	0.390965	0.992607
67			12	0.79253	0.822196
68			15	0.963993	0.828237
69		(50,250)	5	0.320680	0.959092
70			9	0.643199	0.596024
71			11	1.30952	0.978504
72			12	0.702070	0.922750
73			15	0.540342	0.900495
74		(100,125)	5	4.37762	0.299078
75			9	7.24313	-0.231649
76			11	6.12528	0.795691
77			12	3.62068	0.564662
78			15	1.62543	0.721844

5.4.2 The effect of the training algorithm and number of neurons

MATLAB NN toolbox presents three types of training algorithms: Levenberg-Marquardt, Bayesian Regularization and Scaled Conjugate Gradient. Levenberg-Marquardt algorithm typically requires more memory but less time. Training automatically stops when generalization stops improving, as indicated by an increase in the mean square error of the validation samples. Bayesian Regularization typically requires more time, but can result in good generalization for difficult, small or noisy datasets. Training stops according to

adaptive weight minimization (regularization). The third algorithm is the Scaled Conjugate Gradient algorithm, which requires less memory. Training automatically stops when generalization stops improving, as indicated by an increase in the mean square error of the validation samples. Table 5.2 shows the MSE and regression obtained using the three algorithms for NN training with different numbers of neurons and a fixed window size. It is evident that the NN exhibits the best performance when using Bayesian algorithm with 11 neurons. Therefore, Bayesian algorithm will be used for NN training with 11 neurons.

Table 5.2: The effect of training algorithm on the NN performance

Case No.	Used Algorithm	No. of neurons	Testing samples MSE	Testing samples Regression
1	Levenberg-Marquardt	2	2.09785	0.626813
2		5	1.6266	0.976664
3		7	0.893722	0.846778
4		9	0.75342	0.84581
5		10	0.427154	0.958723
6		11	0.104874	0.98823
7		12	1.28624	0.792055
8		15	0.658078	0.903213
9		17	3.84497	-0.167069
10		20	0.104874	0.98823
11		25	1.87696	0.699264
12		30	0.654845	0.910816
13	Bayesian Regularization	2	1.73211	0.852492
14		5	1.539434	0.818052
15		7	0.729192	0.925733
16		9	7.32756e-2	0.983494
17		10	9.64469e-2	0.978297
18		11	4.58467e-3	0.99266
19		12	0.124710	0.988456
20		15	1.69543	0.434623
21		17	1.34332	0.935624
22		20	0.748392	0.858596
23		25	0.853030	0.879769
24		30	3.64849	0.591054

25	Scaled conjugate Gradient	2	0.709130	0.915576
26		5	0.302373	0.971618
27		7	2.68453	0.521451
28		9	0.416194	0.984492
29		10	0.340863	0.970376
30		11	0.200330	0.976306
31		12	0.635342	0.957161
32		15	2.79162	0.771812
33		17	0.261919	0.991968
34		20	0.363748	0.974512
35		25	0.851280	0.947751
36		30	0.285872	0.893380

The final structure of the NN is shown in Figure 5.5.

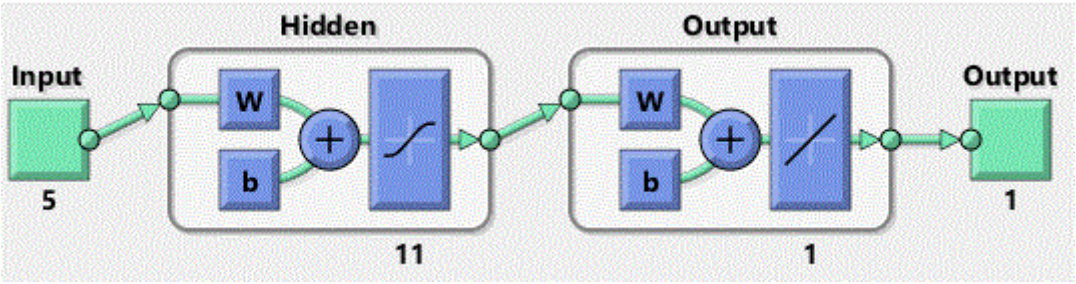

Figure 5.5: Structure of the built Neural Network using MATLAB toolbox

The flowchart presented in Figure 5.6 shows the steps followed in the broken rotor bar fault detection based on the NN technique.

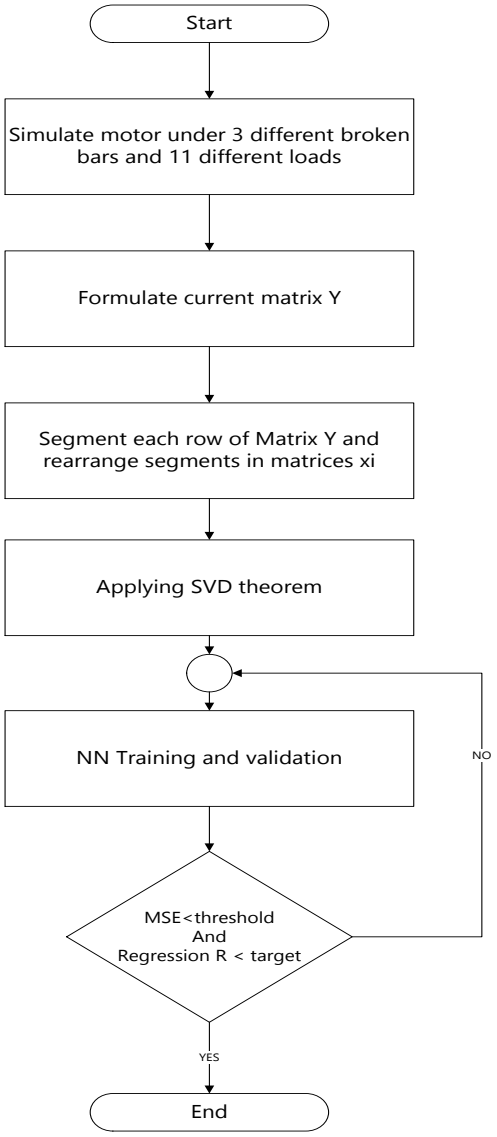

Figure 5.6: The followed steps in broken rotor bar detection

5.5 Combined ANN –SVD method for broken bar diagnosis

5.5.1 Applying the SVD theorem on the LSPMSM stator current

In order to apply the SVD theorem in broken bar fault diagnostics, current signatures were obtained by simulating the motor described in Section 3.5 (750W) under different numbers of broken bars and at different loading levels for of simulation time equal to 5 s. Each current signature was arranged in one row of the matrix Y. However, in the work described in this section, current matrix Y contains the current signatures obtained through motor simulation under 11 different loads and 3 different numbers of broken bars. Hence, the current matrix Y will contain all probabilities of simulation cases, which are represented in 33 current rows, where each row pertains to a stator current vector with 12500 points at fixed step-size with fundamental sampling time (1/2500). The load vector (in per unit) and the broken bars vector can be represented as follows:

$$L = \begin{bmatrix} 0 & 0.1 & 0.2 & 0.3 & 0.4 & 0.5 & 0.6 & 0.7 & 0.8 & 0.9 & 1 \end{bmatrix}$$
$$BRB = \begin{bmatrix} 0 & 2 & 4 \end{bmatrix} \quad \textbf{(5.4)}$$

where L denotes the loading level vector in *pu* and *BRB* is the broken bars vector. The entire current matrix Y will be of size $33 \times 12{,}500$.

Each current row of the matrix Y is divided into segments in order to obtain a distinguishing attribute from each segment. Tests were performed with different numbers of segments, each with different number of points. The findings indicated that; five current segments with 2,500 data points in each represent the sub-optimal current segmentation that will yield the best NN performance. More details will be given at the end of this chapter. These segments were rearranged in separate matrices x_i , $i \in \{1, 2, \ldots, 33\}$, where each matrix

represents one row of the whole current matrix Y and consists of 5 rows and 2,500 columns. Singular value decomposition approach was applied on each matrix with the help of MATLAB® SVD toolbox. This process returned SVD matrix with 33 vectors of singular values, whereby each vector represents the Eigenvector for each simulation case of the previously described 33 cases.

According to the SVD properties, the high impact singular values are concentrated at the beginning of the vector in descending order, i.e. there is no need to take all of the SVD vector values. In this work, the first five singular values were sufficient to demonstrate the differences between the SVD vectors. However, the formulated SVD vectors will be used later on as an input to the multi-layer neural network. Figure 5.7 illustrates the previously described steps that have been followed to formulate the NN input data.

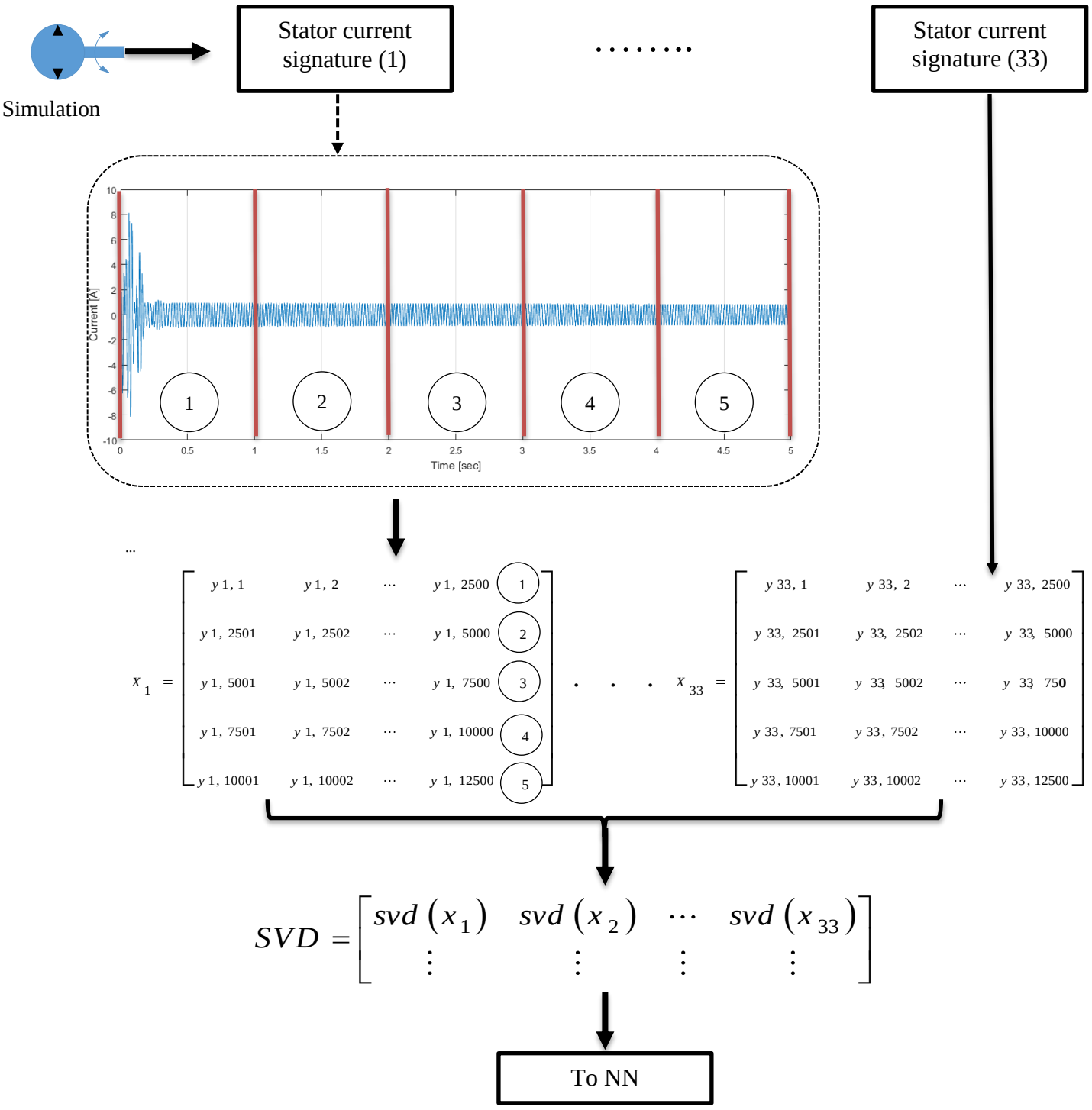

Figure 5.7: Methodology of formulating NN input data

5.5.2 Using the formulated SVD matrix in MFNN training

As previously mentioned, MFNN was used in order to diagnose and monitor the occurrence and the size of the broken bars fault in LSPMSM. The inputs to the network are the singular vectors of the stator current matrix and the outputs are the number of broken bars. In order to design and test the neural network, the extracted SVD matrix of 33 singular values, discussed in the preceding subsection, was forwarded to the neural network. Using MATLAB® neural network toolbox, the MFNN design requires determining the input training matrix, the target training vector (desired outputs) and the number of neurons in the hidden layer by trial and error [89].

During training process, three kinds of samples can be used for validation and testing the input data in the MATLAB® neural network toolbox. Training samples, which were presented to the network during the training, are used to adjust the network according to its error value. Validation samples are used to measure the network generalization and to halt training when generalization stops improving. In addition, testing samples, which have no effect on the training process but provide an independent measure of network performance during and after training, are also utilized. However, in the testing presented in this section, 70% (23 samples) of the 33 input samples were used for training, 15% (5 samples) were used for validation and 15% (5 samples) were used for testing.

The next step is to determine the network architecture by setting the number of neurons in the hidden layer. The optimal number of neurons are determined based on trial and error. However, 11 neurons is the sub-optimal number of nodes resulting in the best performance of the NN. The Bayesian Regularization algorithm was used in the work presented in this

section; because of its beneficial properties, while the parameters used for ANN training are summarized in Table 5.3.

Table 5.3: ANN learning parameters

No.	Parameter	Value
1	Input training	SVD vectors [8x33].
2	Target training	[0 2 4]
3	No. of hidden neurons	11
4	No. of Epochs	1000
5	Learning rate	0.018
6	Training algorithm	Bayesian Regularization algorithm

In order to measure the accuracy of the built network during the trial and error step, two measurement tools were used, one of which is Mean Square Error (MSE); that measures the average squared difference between outputs and targets, where lower values are better and zero denotes absence of errors. In addition, Regression (R) values were used to measure the correlation between outputs and targets. R-value of 1 means a close relationship and 0 indicates no or random relationship. The MSE and regression of the trained neural network are presented in Table 5.4.

Table 5.4: MSE and regression of the trained NN

Parameter	No. of samples	MSE	R
Training	23	4.78563×10^{-15}	1
Testing	5	4.58467×10^{-3}	0.99266

5.6 Simulation results

Based on the built neural network, different simulations were performed to diagnose the broken bar fault occurrence under different loading levels. The first test has simulated different broken bars that are not trained, while all used loads are trained. The results show indicate about 97% success rate, as only one case was wrongly estimated, as shown in Table 5.5 . In the second test, different loads were applied none of which were trained, while all broken bars were trained. The success rate was 94.7%, due to three incorrectly estimated cases, as shown in Table 5.6. In the last scenario, which was the worst case, non of the presented loads or broken bars were trained. The 92.98% success rate indicated that the network was unable to detect four cases properly, as shown in Table 5.7.

Table 5.5: NN testing - First test (All input loads are trained and all No. of input broken bars are NOT trained)

No.	Loading level (pu)	Detected No. of BRB	Actual No. of BRB	Status	%NMSE
1	0	0.71995	1	Correct	0.464319938
2		2.7399	3	Correct	0.964065028
3		5.0395	5	Correct	0.593125662
4	0.1	1.2208	1	Correct	0.0556476
5		2.9327	3	Correct	0.39533232
6		5.3139	5	Correct	0.07160035
7	0.2	0.87234	1	Correct	0.161851479
8		2.9546	3	Correct	0.346502569
9		5.4590	5	Correct	$3.3544\ x10^{-06}$
10	0.3	$2.9834x10^{-02}$	1	**Incorrect**	3.784421539
11		2.8418	3	Correct	0.632403628
12		5.2899	5	Correct	0.097056213

13	0.4	0.56499	1	Correct	0.931649224
14		3.1973	3	Correct	0.020776107
15		4.7598	5	Correct	1.644594856
16	0.5	0.92849	1	Correct	0.089681601
17		3.0091	3	Correct	0.238952656
18		4.8877	5	Correct	1.098657201
19	0.6	0.74805	1	Correct	0.396830772
20		3.0635	3	Correct	0.151472078
21		4.7788	5	Correct	1.556553288
22	0.7	0.73143	1	Correct	0.43610784
23		3.0838	3	Correct	0.123914315
24		4.7163	5	Correct	1.85528348
25	0.8	0.69073	1	Correct	0.540117313
26		3.1322	3	Correct	0.069363738
27		4.5783	5	Correct	2.60769261
28	0.9	0.66423	1	Correct	0.613811982
29		3.1864	3	Correct	0.026929652
30		4.5354	5	Correct	2.867625891
31	1	0.54143	1	Correct	1.016809983
32		3.2751	3	Correct	2.71706E-06
33		4.5193	5	Correct	2.968362953

Statistics:
%NMSE=0.4064%
No. Wrongs = 1
No. Corrects = 32
% Success = (65/66)*100% = 96.97%

Table 5.6: NN testing - Second test (All input loads are NOT trained and all No. of input broken bars are trained)

No.	Loading level (pu)	Detected No. of BRB	Actual No. of BRB	Status	%NMSE
1	0.52	$1.3323\ x10^{-15}$	0	Correct	$9.16226\ x10^{-30}$
2		2.0000	2	Correct	0.208022205
3		4.0000	4	Correct	0.83208882
4	0.14	$6.8704\ x10^{-04}$	0	Correct	$2.43648\ x10^{-06}$
5		1.8492	2	Correct	0.637929656
6		3.8104	4	Correct	1.803518104
7	0.33	0.3891	0	Correct	0.781485725
8		0.87315	2	**Incorrect**	9.097730655
9		4.2234	4	Correct	0.163729308
10	0.57	$5.3268\ x10^{-03}$	0	Correct	0.000146464
11		1.9643	2	Correct	0.288587306
12		4.0263	4	Correct	0.726648275
13	0.62	$4.4251\ x10^{-03}$	0	Correct	0.000101075
14		2.0112	2	Correct	0.185458253
15		3.9889	4	Correct	0.8787332
16	0.85	0.17568	0	Correct	0.159310072
17		2.4919	2	Incorrect	0.437554522
18		4.2073	4	Correct	0.194669108
19	0.93	0.59987	0	**Incorrect**	1.857431788
20		2.0804	2	Correct	0.074763698
21		4.0016	4	Correct	0.825470193
22	0.22	0.13337	0	Correct	0.091815265
23		2.3344	2	Correct	0.092201187
24		4.4015	4	Correct	0
25	0.41	0.10917	0	Correct	0.061518425
26		2.1196	2	Correct	0.033991915
27		3.9648	4	Correct	0.984384964
28	0.64	$1.5501\ x10^{-02}$	0	Correct	0.001240275
29		2.0103	2	Correct	0.187223578
30		3.9889	4	Correct	0.8787332

31	0.74	$1.5979\ x10^{-02}$	0	Correct	0.001317947
32		1.9527	2	Correct	0.317597482
33		3.9303	4	Correct	1.14606474
34	0.99	0.12217	0	Correct	0.077042033
35		3.101	2	**Incorrect**	4.183356226
36		4.3822	4	Correct	0.001922707
37	0.44	0.17464	0	Correct	0.15742947
38		1.8491	2	Correct	0.638292632
39		4.0557	4	Correct	0.617232187
40	0.53	0.07050	0	Correct	0.025655284
41		1.897	2	Correct	0.476245802
42		4.1954	4	Correct	0.219257557
43	0.67	0.048248	0	Correct	0.012015925
44		2.1636	2	Correct	0.007123874
45		4.2598	4	Correct	0.103642597
46	0.18	0.043976	0	Correct	0.009982287
47		1.9644	2	Correct	0.288343258
48		3.9067	4	Correct	1.263740691
49	0.13	0.067706	0	Correct	0.023662079
50		1.9747	2	Correct	0.263759196
51		4.0143	4	Correct	0.77387227
52	0.71	$5.6419\ x10^{-03}$	0	Correct	0.000164304
53		2.3178	2	Correct	0.070719865
54		4.3270	4	Correct	0.02864911

Statistics:
%NMSE=0.5961%
No. Wrongs = 3
No. Corrects = 54
% Success = (54/57)*100% = 94.7%

Table 5.7: NN testing - Third test (All input loads and all No. of input broken bars are NOT trained)

No.	Loading level (pu)	Detected No. of BRB	Actual No. of BRB	Status	%NMSE
1	0.52	0.92849	1	Correct	0.04230333
2		3.0091	3	Correct	0.034174895
3		4.8877	5	Correct	0.307402594
4	0.14	0.95146	1	Correct	0.026013764
5		2.8202	3	Correct	0.302408599
6		4.9972	5	Correct	0.117531333
7	0.22	1.1969	1	Correct	0.097987171
8		3.3459	3	Correct	0.217162556
9		5.1746	5	Correct	0
10	0.41	0.55860	1	Correct	0.847313384
11		3.1871	3	Correct	0.02532026
12		4.7432	5	Correct	0.695035061
13	0.57	0.72552	1	Correct	0.357509059
14		3.0615	3	Correct	0.006989071
15		4.8262	5	Correct	0.45331775
16	0.64	0.78815	1	Correct	0.227421308
17		3.0583	3	Correct	0.008061296
18		4.7532	5	Correct	0.663186221
19	0.77	1.3813	1	Correct	0.448076376
20		3.4364	3	Incorrect	0.410752528
21		5.01945	5	Correct	0.089897992
22	0.85	0.75798	1	Correct	0.286429541
23		3.6953	3	**Incorrect**	1.30240205
24		4.8401	5	Correct	0.417867578
25	0.97	1.4600	1	Incorrect	0.674819736
26		4.2336	3	**Incorrect**	4.758950766
27		5.0495	5	Correct	0.058446842
28	0.62	$7.7452\ x10^{-01}$	1	Correct	0.253237718
29		3.0589	3	Correct	0.007854427
30		4.7604	5	Correct	0.640717551

31	0.93	1.8181	1	**Incorrect**	2.290707345
32		3.1836	3	Incorrect	0.023213449
33		4.9688	5	Correct	0.158174756
34	0.44	0.8377	1	Correct	0.14526077
35		3.001669	3	Correct	0.039690625
36		4.89945	5	Correct	0.282738836
37	0.67	1.13892	1	Correct	0.040393651
38		3.25519	3	Correct	0.084511409
39		5.04671	5	Correct	0.061082894
40	0.18	0.908867	1	Correct	0.059340719
41		2.9879	3	Correct	0.051000942
42		4.7429	5	Correct	0.696002066
43	0.71	1.24619	1	Correct	0.166694817
44		3.3863	3	Correct	0.29602381
45		5.0355	5	Correct	0.072260455
46	0.82	1.301	1	Correct	0.26440575
47		3.7031	3	**Incorrect**	1.337034168
48		4.9261	5	Correct	0.230621195
49	0.18	0.9088	1	Correct	0.059403818
50		2.9879	3	Correct	0.051000942
51		4.7429	5	Correct	0.696002066
52	0.75	1.360957	1	Correct	0.396990586
53		3.4648	3	Correct	0.48411433
54		5.03359	5	Correct	0.074258514
Statistics: **%NMSE=0.4044%** **No. Wrongs = 3** **No. Corrects = 63** **% Success = (53/57*100% = 92.98%**					

These simulation results indicate that the neural network based fault detection scheme is capable of detecting the broken rotor bars. However, the training results are sub-optimal, as all were obtained after many trials using different training algorithms and different numbers of hidden layer neurons.

CHAPTER SIX

CONCLUSIONS AND FUTURE WORK

6.1 Conclusions

The purpose of this work was to develop a complete mathematical model of the LSPMSM to include the broken bar effects, in addition to developing a monitoring method capable of detecting the broken bar faults in the motor based on Artificial Neural Network. As such, the main achievements of this thesis can be summarized in the following points:

- A comprehensive literature survey on the LSPMSM, its steady state analysis, transient analysis and the various methods used in the motor design have been accomplished.

- A dynamic model of the healthy LSPMSM has been built and the effect of the broken bars fault was related to the rotor resistance and inductance matrices. In addition, the detailed design and the required mathematical equations for a healthy motor and a motor with different number of broken bars have been introduced. The developed model was simulated using MATLAB/SIMULINK® software. Simulation results of the built model for both healthy and faulty motor under broken bar condition and at different loading levels were presented.

- The accuracy of the proposed mathematical model was tested based on JMAG® finite element results. The results show a very good agreement between the

proposed model and the JMAG® results, where the accuracy of the proposed model was tested using three error measurements. Root mean square error (RMSE) and normalized mean square error (%NMSE) were used to measure the error in the simulated stator current signal coming from the proposed model and JMAG model under different loading values and broken bar numbers:

  - The average error value of the calculated RMSE and the percentage of the NMSE were 1.78 and 3.7%, respectively. That indicating a high degree of similarity between the proposed model and the FEM model.

- Detailed comparisons and discussions of the obtained results from both models have also been presented. It can be concluded that:

  - The presence of broken bars in the LSPMSM rotor caused changes in the air gap flux and the current distribution among the rotor bars during acceleration from standstill to rated speed.

  - Investigation of the broken rotor bar fault showed that such fault will change the motor performance during startup. This situation is critical for broken rotor bar fault detection.

- A practical contribution for an automated diagnostic system using artificial neural network was built. This method successfully classified the fault size based on the extracted features from the stator phase current using singular value decomposition method. In addition, this method was successfully applied to the designed LSPMSM. Three different tests were performed to assess the reliability of the built diagnosis system:

- The first test has simulated different broken bars that were not trained, while all used loads were trained, achieving 97% accuracy, with only one wrongly estimated case.
- In the second test, different loads were applied, none of which were trained, while all broken bars were trained. The 94.7% success rate revealed three incorrectly estimated cases.
- In the last scenario, which was the worst case, none of the presented loads or broken bars were trained. The percentage of success was around 92.98%, due to the network failing to detect four cases properly.

6.2 Future work

- The proposed model has been verified using 2D geometry. It would be more accurate to build a 3D model of the LSPMSM to include the effect of the end-rings.
- In the developed diagnostic tool, the sub-optimal solutions were obtained based on trial and error. It would thus be beneficial to use optimization algorithms to achieve the optimum solutions, such as Genetic algorithm.
- Developing other monitoring techniques based on stator current frequency components would also be a fruitful path to pursue in future research.
- Future studies could focus on enhancing the built monitoring techniques by combining both the proposed model and that FEM data as the input to the neural network.

NOMENCLATURE

g: the radial air-gap length
I'dr: direct axis of the rotor current
i'_m : equivalent magnetizing current of the PM referred to the stator side
I'qr: quadrature axis of the rotor current
Ias: stator phase *a* current
Ids: direct axis of the stator current
I_j: the rotor bar current
Iqs: quadrature axis of the stator current
Ir: rotor current vector
J: the rotor inertia
K_r :Poly-phase to Two phase transformation matrix
K_s: Park's transformation matrix
l: the motor stack length
L'lr: rotor leakage inductance
Lmq: mutual inductances in the q reference frame
L_{ijs}: mutual inductance between the stator coils.
L_{ks}: self-inductance of the stator coils
Lls: stator leakage inductance
Lmd: mutual inductances in the d reference frame
Ls: inductance matrix of the stator.
Lsr: mutual inductance between stator and rotor.
M_{rr} : mutual magnetic coupling between two rotor loops
nb: the number of broken bars
Nr: No. of rotor cage loops
P: the number of motor poles.
r: the average radius of the air-gap
r'dr: direct axis of the rotor resistance
r'qr: quadrature axis of the rotor resistance
R_b: rotor bar and resistance
R_e: end-ring resistances
rs: stator phase resistance
Tdamp: the damping torque in the direction opposite to the rotor rotation
Tem: the motor electromechanical torque
Tload: the mechanical torque applied by the load
Vas: stator phase *a* voltage.
Vdr: direct axis of the rotor voltage
Vds: direct axis of the stator voltage
Vqr: quadrature axis of the rotor voltage

Vqs: quadrature axis of the stator voltage
Wx: the winding distribution along the airgap of the x windings
Wy: the winding distribution along the airgap of the y windings
α_r: angle between two adjacent rotor loops
γ: the angle along the airgap (angular position along the stator inner surface)
θr: the rotor angular position with respect to the stator reference frame
λ'dr: direct axis of the rotor flux linkage
λ'_m: peak flux linkage due to the PM
λ'qr: quadrature axis of the rotor flux linkage
λas: stator phase a flux linkage.
λds: direct axis of the stator flux linkage
λpm: flux linkage vector due to the presence of the PMs.
λqs: quadrature axis of the stator flux linkage
λ_r: the rotor bar flux
Mo: the space permeability
ωr: the rotor angular speed

References

[1] N. Taylor, "Network effects of line start permanent magnet synchronous motors as replacements for induction motors," Department of Electrical Power Engineering, Royal Institute of Technology, Stockholm, 2001.

[2] A. Bonnett and G. Soukup, "Failures in three-phase squirrel-cage induction motors," *IEEE Trans. Industry Applications,* vol. 28, no. 4, July, 1992.

[3] U. Herslöf, "Design, Analysis and Verification of a Line Start Permanent Magnet Synchronous Motor," Royal Institute of Technology, Sweden, Stockholm, 1996.

[4] A. H. Isfahani and S. Vaez-Zadeh, "Effects of magnetizing inductance on start-up and synchronization of line start permanent-magnet synchronous motors," *IEEE Transaction Magazine,* vol. 47, pp. 823-829, 2011.

[5] B. Lee and B. Hong, "Optimum Desgin criteria for maximum torque and efficiency of line start permanent magnet synchrounous motor using response surface methology and finite element method," *IEEE Transaction Magazine,* vol. 48, no. 2, pp. 863-866, 2012.

[6] T. Modeer, "Modeling and Testing of Line Start Permanent Magnet Motors," KTH Vetenskap OCH Konst, Stockholm, Sweden, 2007.

[7] C. M. Ong, Dynamic simulation of electric machinery using MATLAB/SIMULINK, USA, New Jersey: Prentice Hall, 1997.

[8] J. Douglas, "Hydro generator failure," *IEEE Power Engineering Review*, vol. 8, no. 11, pp. 4-6, 1988.

[9] G. Stone and J. Kapler, "Stator winding monitoring," *IEEE Industry Applications Magazine,* vol. 4, pp. 15-20, 1998.

[10] T. Miller, "Methods for testing permanent magnet polyphase motors," in *IEEE, IAS Conf. Rec*, 23(D):494–499, 1981.

[11] A. Bonnett and C. Young, "Surveys can't answer all of your motor failure questions, but a thorough root cause analysis can help fill in the gaps," *Electrical Construction & Maintenance (EC&M) magazine,* October, 2004.

[12] T. Miller, "Synchronization of line-start permanent-magnet ac motors," in *Transactions IEEE, PAS, 103:1822–1828,* July, 1984.

[13] G. Kliman, Handbook of electric motors, 2nd edition, Boca Raton: CRC press, 2004.

[14] J. Pyrhönen, T. Jokinen and V. Hrabovcova, "Design of rotating electrical machines, 1st edition," Wiley Online Library, New York, 2008.

[15] S. Lee, D. Hyun, T. Kang, C. Yang, S. Shin and H. Kim, "Identification of false rotor fault indications produced by on-line MCSA for medium voltage induction machines," in *IEEE pulp and paper industry conference (PPIC-2015),* Milwaukee, Wisconsin, 2015.

[16] J. Lonen, J. Kamarainen, T. Lindh and J. Ahola, "Diagnosis tool for motor condition monitoring," *IEEE Trans. Ind. Appl.*, vol. 41, no. 4, pp. 963-971, 2005.

[17] S. Ferkolj, "Application of finite element method to predict damaged induction motor performance," *IEEE Trans. Magn.*, vol. 37, no. 5, p. 3635–3639, 2001.

[18] A. Bellini, F. Filippetti, C. Tassoni and G. Capolino, "Advances in diagnostic techniques for induction machines," *IEEE Trans. Ind. Electron.*, vol. 55, no. 12, p. 4109–4126, 2008.

[19] W. Finley, M. Hodowanec and W. Holter, "Analytical approach to solving motor vibration problems," *IEEE Trans. Ind. appl.*, vol. 36, no. 5, p. 1467–1480, 2000.

[20] P. Zhang and T. Habetler, "A survey of condition monitoring and protection methods for medium-voltage induction motors," *IEEE Trans. Ind. Appl.*, vol. 47, no. 1, pp. 34-46, 2011.

[21] Z. HM, "Design analysis of line-start interior permanent magnet synchronous motor," M.Sc. Thesis, Memorial University of Newfoundland, http://sunzi.lib.hku.hk/ER/detail/hkul/, 2011.

[22] I. Culbert and W. Rhodes, "Using current signature analysis technology to reliably detect cagewinding defects in Squirrel-Cage induction motors," *IEEE Trans. Ind. Appl.*, vol. 43, no. 2, p. 422–428, 2007.

[23] B. Mirafzal, "Incipient fault diagnosis in Squirrel-Cage induction motors," Marquette University, Milwaukee, 2005.

[24] H. A. Toliyat, S. Nandi, S. Choi and H. Meshgin-kelk, Electric machines Modeling, Condition Monitoring, and Fault Diagnosis.

[25] F. Merrill, "Permanent magnet excited synchronous motors," *AIEE*, vol. 74, no. 3, pp. 1754-1760, 1955.

[26] J. Douglas, "Current loci of permanent magnet synchronous motors," *AIEE,* vol. 78, no. 3, pp. 76-78, 1959.

[27] D. Cahill and B. Adkins, "The permanent magnet synchronous motor," *Proc. of IEE,* vol. 109, no. 48, pp. 483-491, 1962.

[28] W. Volkrodt, "Synchronous machines with ferrite magnets," in *Siemens Rev.*, 248-254, 1976.

[29] B. Chalmers, S. Hamed and G. Baines, "Parameters and performance of a high-field permanent magnet synchronous motor for variable-frequency operation," *Proc. IEE,* vol. 132, no. 3, pp. 117-124, 1985.

[30] D. Rodger, H. Lai, H.-C. R.J., P. Coles and F. Robinson, "new high efficiency line start motor with high starting torque," in *3rd IET Int. Conf. on Power Electronics, machines and Drives, PEMD 2006*, 551-555, 2006.

[31] K. Miyashita, S. Yamashita, S. Tanabe, T. Shimazu and H. Sento, "Development of a high speed 2-pole permanent magnet synchronous motor," *IEEE Trans. Power App. Syst,* vol. 99, no. 6, pp. 2175-2182, 1980.

[32] A. Ishizaki, T. Tabako and K. Saitoh, "Prediction and improvement on synchronous performance of AC permanent magnet motor," in *IEEE IAS Meeting*, 1985.

[33] T. Reneyuan, "Research and development of rare earth permanent magnet machines," in *5th IEEE Int. Conf. on Electrical Machines and Systems, ICEMS-2001*, vol. 1, pp. 28–34, 2001.

[34] A. Knight and J. Salmon, "Modeling the dynamic behaviour of single phase line start permanent magnet motors," in *34th IEEE Ind. Appl. Conf. Annual Meeting*, vol. 4, pp. 2582–2588, 1999.

[35] A. Knight and C. McClay, "The design of high efficiency line start motors," *IEEE Trans. Ind. Appl.,* vol. 36, no. 6, p. 1555–1562, 2000.

[36] K. Kurihara and M. Rahman, "High-efficiency line start interior permanent magnet synchronous motors," *IEEE Trans. Ind. Appl.,* vol. 40, no. 3, p. 789–796, 2004.

[37] E. Peralta-Sanchez, A. Smith and J. Rodriguez-Rivas, "Steady state analysis of a canned line start PM motor," *IEEE Trans. Magn,* vol. 40, no. 3, pp. 4080-4083, 2011.

[38] S. K. Beak and K. B. B., "Practical optimum design baesd on magnetic balance and copper loss minimization for a single-phase line start PM motor," *IEEE Trans. Magn.,* vol. 47, no. 10, p. 3008–3011, 2011.

[39] A. Isfahani and S. Vaez-Zadeh, "Line start permanent magnet synchronous motors: challenges and opportunities," in *J. Energy*, pp. 1755–1763, 2009.

[40] T. Marcic, A short review of energy-efficient line start motor design, pp. 119–122: TECES, Res. Development Centre for Electr. , ISSN 0033–2097 , 1. March 2011.

[41] M. Rahman, A. Osheiba, K. Kurihara, M. Jabbar and H. Ping, "Advances on single phase line-start high efficiency interior permanent magnet motors," *IEEE Trans. Ind. Electron*, vol. 59, no. 3, p. 1333–1345, 2012.

[42] A. Aliabad and M. Mirsalim, "Analytical modelling and dynamic analysis of pole-changing line-start permanent magnet motors," *IET Electr. Power Appl.*, vol. 6, no. 3, pp. 149-155, 2012.

[43] V. Honsinger, "Performance of polyphase permanent magnet," *IEEE Trans. Power App. Syst*, vol. 99, no. 4, pp. 1510-1518, 1980.

[44] K. Binns and M. Jabbar, "High field self-starting permanent magnet synchronous motor," *Proc. IEE*, vol. 128, no. 3, pp. 157 - 160, 1981.

[45] B. Chalmers, S. Hamed and G. Baines, "Parameters and performance of a high-field permanent magnet synchronous motor for variable-frequency operation," *Proc. IEE,*, vol. 132, no. 3, pp. 117-124, 1985.

[46] T. Marcic, Stumberger, B. and G. Stumberger, "Comparison of induction motor and line-start IPM synchronous motor performance in a variable-speed drive," *IEEE Trans. Ind. Appl.*, vol. 48, no. 6, p. 2341–2352, 2012.

[47] Sorgdrager, A. Grobler and R.-J. Wang, "Design Procedure of a Line-Start Magnet Synchronous Machine," in *Proceedings of the 22nd South African Universities Power Engineering Conference* , South African , 2014.

[48] Q. Lu and Ye.Y, "Design and analysis of large capacity line start permanent magnet motor," *IEEE Trans. Magn.*, vol. 44, no. 11, pp. 4417-4420, 2008.

[49] T. Ding, N. Takorabet and F. W. X. Sargos, "Design and analysis of different line start PM synchronous motors for oil-pump applications," *IEEE Trans. Magn.*, vol. 45, no. 3, pp. 1816-1819, 2009.

[50] W. Fei, P. Luk, J. Ma, J. Shen and G. Yang, "A high performance line start permanent magnet synchronous motor amended from a small industrial three phase induction motor," *IEEE Trans. Magn.*, vol. 45, no. 10, pp. 4724-4727, 2009.

[51] A. Aliabad, M. Mirsalim and N. Ershad, "Line-start permanent magnet motors: Significant improvements in starting torque, synchronization, and steady state performance," *IEEE Trans. Magn.*, vol. 46, no. 12, pp. 4066-4072, 2010.

[52] S. Peralta, E. Smith and R. Rodriguez, "Steady state analysis of a canned line start PM motor," *IEEE Trans. Magn.*, vol. 40, no. 3, pp. 4080-4083, 2011.

[53] T. Marcic, B. Stumberger and G. Stumberger, "Comparison of induction motor and line-start IPM synchronous motor performance in a variable-speed drive," *IEEE Trans. Ind. Appl.*, vol. 46, no. 12, pp. 2341-2352, 2012.

[54] N. Taylor, "Network effects of line start permanent magnet synchronous motors as replacements for induction motors," MSc Thesis, Department of Electrical Power Engineering Royal Institute of Technology , Stockholm, 2001.

[55] A. D. Aliabad, M. Mirsalim and N. F. Ershad, "Line-start permanent-magnet motors: Significant improvements in starting torque, synchronization, and steady-state performance," *IEEE Transactions on Magnetics*, vol. 46, no. 12, pp. 4066-4072, 2010.

[56] T. Miller, "Synchronization of line-start permanent-magnet AC motors," *IEEE Trans. Power App. Syst*, pp. 822-1828, 1984.

[57] M. Popescu, T. Miller, M. McGilp, G. Strappazzon, N. Trivillin and R. Santarossa, "Line start permanent magnet motor: single-phase starting performance analysis," in *Conference Record of the 2002 IEEE Industry Applications Conference. 37th IAS Annual Meeting (Cat. No.02CH37344)*, 2002 .

[58] D. Hwang, W. Young, J. Sun and Y. Kim, "Robust Diagnosis Algorithm for Identifying Broken Rotor Bar Faults in Induction Motors," *Journal of Electrical Engineering and Technology*, vol. 8, no. 12, pp. 742-749, 2014.

[59] C. Pezzani, P. Donolo, G. Bossio, M. Donolo, A. Guzmán and S. E. Zocholl, "Detecting Broken Rotor Bars With Zero-Setting Protection," *IEEE Transactions on Industry Applications*, vol. 50, no. 2, pp. 1373-1384, 2014.

[60] J. Zarei, M. A. Tajeddini and R. Hamid, "Fault diagnosis of induction motors broken rotor bars by pattern recognition based on noise cancelation," in *2014 IEEE 23rd International Symposium on Industrial Electronics, ISIE 2014 A4 - Bogazici University; IEEE Industrial Electronics Society (IES); The Institute of Electrical and Electronics Engineers (IEEE)*, pages: 2451-2456, 2014.

[61] Z. Guo-liang, W. Yun-bing and C. Gang, "Rotor break-bar fault diagnosis of Asynchronous motor Based on Empirical mode decomposition," in *IEEE industry applications conference*, pages: 2-5, 2012.

[62] I. Aydin, M. Karakose and E. Akin, "A new method for early fault detection and diagnosis of broken rotor bars," *Energy Conversion and Management*, vol. 52, no. 4, pp. 1790-1799, 2011.

[63] J. Wang, R. X. Gao and a. R. Yan, "Broken-Rotor-Bar Diagnosis for Induction Motors," *Journal of Physics: Conference Series*, vol. 305, p. 120, 2011.

[64] S. Chen, "Induction machine broken rotor bar diagnostics using prony analysis," Master thesis submitted to the school of electrical and electronics engineering, university of Adelaide, pages: 1-127, 2008.

[65] S. Shashidhara and S. Raju, "Tradeoff Analysis of Wavelet Transform Techniques for the Detection of Broken Rotor Bars in Induction Motors," *Advance in Electronic and Electric Engineering*, vol. 3, no. 8, pp. 1019-1030, 2013.

[66] Z. PuShi, V. Chen and Z. Zouaoui, "Optimal Wavelets for Broken Rotor Bars Fault Diagnosis," in *013 9th IEEE International Symposium on Diagnostics for Electric Machines, Power Electronics and Drives, SDEMPED 2013 A4 - 'Generalitat Valenciana-Conselleria d'Educacio, Cultura i Esport'; IEEE Power Electronics Society (PELS); SIEMENS; Universitat Pol*, pages: 49-56, 2013.

[67] K. M. Siddiqui and V. Giri, "Broken Rotor Bar Fault Detection in Induction Motors Using Wavelet Transform," in *2012 International Conference on Computing, Electronics and Electrical Technologies (ICCEET)*, pages: 1-6, 2012.

[68] M. R. Mehrjou, N. Mariun, M. Norhisam and M. A. M. Radzi, "Broken rotor bar detection in LS-PMSMs based on statistical features analysis of startup current envelope," in *IEEE International Conference on Smart Instrumentation, Measurement and Applications (ICSIMA)*, Putrajaya, Malaysia, November, 2015.

[69] M. R. Mehrjou, N. Mariun, M. Karami, N. Misron and M. A. Mohd, "Performance analysis of line-start permanent magnet synchronous motor in presence of Rotor fault," in *IEEE Student Conference on Research and Development*, 2014.

[70] M. R. Mehrjou, N. Mariun, M. Karami, N. Misron and M. A. M. Radzi, "Broken Rotor Bar Detection in LS-PMSMs Based on Statistical Features Analysis of Start-up Current Envelope," in *Proc. of the 2015 IEEE 3rd international conference on smart instrumentation, measurements and applications (ICSIMA 2015)*, Malysia, Nov. 2015.

[71] M. R. Mehrjou, N. Mariun, N. Misron and M. A. M. Radzi, "Analysis of statistical features based on start-up current envelope for broken rotor bar fault detection in line start permanent magnet synchronous motor," *Springer-Verlag Berlin Heidelberg, Electr Eng*, pp. DOI 10.1007/s00202-016-0404-3, 2016.

[72] M. Hosseinzadeh and A. Sadoughi, "Conceptual comparison of LSPMS and induction machines for line-fed of different conditions," *Journal of world's Electrical Engineering and technology JWEET,* vol. Tech. 3(1), pp. 26-36, 2014.

[73] S. Hamdani, O. Touhami and R. Ibtiouen, "A generalized two-axis model of a squirrel cage induction motor for rotor fault diagnosis," *Serbian Journal of Electrical Engineering,* vol. 5, no. 1, pp. 155-170, May, 2008.

[74] S. Kulkarni and A. Thosar, "Mathematical Modeling and Simulation of Permanent Magnet Synchronous Machine," *International Journal of Electronics and Electrical Engineering,* vol. 1, no. 2, pp. 66-71, 2013.

[75] T. Lipo and A. Garcia, "Complex vector model of the squirrel cage induction machine including instantanous rotor bar currents," in *IEEE for industrial applications,* 1998.

[76] K. Drobnic, H. LAvric, V. Ambrozic and R. Fiser, "Flux linkages in squirrel-cage motor," 2015.

[77] F. Bangura and N. Demerdash, "Characterization of Effects of Broken Bars and connectors in Squirrel-cage induction motors by a time-stepping coupling finite element state space modeling approach," *IEEE Trans. Energy Conversion,* vol. 14, no. 6, pp. 1167-1176, 1999.

[78] H. A. Tpliyat and S. Nandi, Electric machines modelling, condition monitoring and fault diagnosis, London: Taylor and Francis group, LLC, 2013.

[79] N. Sriram, "Design optimization of an interior permanent magnet motor," Master of Engineering (Hons.) thesis, School of Electrical, Computer and Telecommunications Engineering, University of Wollongong, 1997.

[80] S. Lim and K. Tseng, "Dynamic model of interior pemanent magnet motor with skewed stator slots," in *IEEE conference of industrial applications*, Nanyang Avenue, Singapore, 1999.

[81] V. V. Kuptsov, A. S. Sarvarov and M. Y. Petushkov, "A new approach to analysis of induction motors with rotor faults during startup based on the FEM," *Progress In Electromagnetics Research,* vol. 45, pp. 269-290, 2012.

[82] J. company, "JMAG main page," [Online]. Available: https://www.jmag-international.com/. [Accessed 01 December 2016].

[83] S. B. Said, "Design study of hybrid excitation flux switching motor for electric vehicles," Universiti Tun Hussein Onn Malaysia, July 2014.

[84] R. Trifa, C. Martis, K. Biro and F. Surdu, "Modeling and simulation of permanent magnet synchronous motor for brake-by-wire technology in automative applications," in *25th European Conference on Modelling and Simulation (ECMS)*, Joanna, 2014.

[85] Y. Liao, "Analysis of fault conditions in permanent-magnet in-wheel motors," KTH Electrical engineering, Stockholm, Sweden , 2011.

[86] S. R. Pérez, "Analysis of a light permanent magnet in-wheel motor for an electric vehicle with autonomous corner modules," KTH Electrical engineering, Stockholm, Sweden , 2011.

[87] M. b. Shadmand, "A design oriented framework to determine the parasitic paramenters of high frequency magnetics in switching power supplies using FE analysis techniques," Texas A&M University, Texas, May, 2012.

[88] J. K. Basu, D. Bhattacharyya and T. Kim, "Use of Artificial Neural Network in Pattern Recognition," *International Journal of Software Engineering and Its Applications*, vol. 4, no. 2, pp. 23-34, 2010.

[89] M. Moradian, M. Ebrahimi, M. Danesh and M. bayat, "Detection of Broken Bars in Induction Motors Using a Neural Network," *Journal of Power Electronics*, vol. 6, no. 3, pp. 245-252, July, 2006.

Vitae

Name :KHALID IBRAHIM BARAD'IEH

Nationality:JORDANIAN

Date of Birth:2/23/1990

Email :khalid.baradia@outlook.com

Address:West Bank - Hebron

Education

09/2014 – 12/2016 **Master of Science in Electrical Engineering**, KSA, King Fahd University Of Petroleum and Minerals (KFUPM)

- Master Degree in Electrical Engineering with GPA 3.75/4. My defense title is " A Linear Algebraic Based Diagnosis Method using ANN for broken Rotor Bars of Line Start permanent Magnet Motors"
- Researcher in power systems, AC machines and signal processing fields. Did projects in Renewable energy power planets, fiber optics and adaptive filters.
- Publications: Two journal papers In progress.

09/2008 – 06/2013 **Bachelor degree in Electrical, Electronics and Telecommunications Engineering**, Palestine, Palestine Polytechnic university (PPU)

- Bachelor degree in Electrical Engineering, minor Communications and Electronics Engineering with GPA 90% (Excellent with first honor degree).
- Recipient of PPU "honored student" Scholarship.
- My Graduation project "Intelligent traffic with automatic violation system" got the highest degree in electrical Engineering department with a grade of 95%.

09/2007 – 06/2008 **High School Certificate - scientific branch**, Palestine, Sourif Secondary School

- High School certificate scientific branch with grade of 95.2%.

WORK EXPERIENCE (ENGINEERING WORK)

09/2014 – 12/2016 **Center for Energy and Geo-Processing Coordinator,** King Fahd University Of Petroleum and Minerals (KFUPM)

- Manage the collaboration between KFUPM and Georgia-tech University.
- Preparation for the annual CeGP workshop.
- Audio-Visual System Coordinator.
- Wrote protocols, qualification documents, test plans and test reports for quality assurance purposes.
- Continually improved methods and procedures for processes, measurement, documenting and workflow techniques.

07/2013 – 08/2014 **Electrical Engineer and Tenders department responsible,** National Computer and Software (NCSPal Co.Ltd.)

- Working as a Design engineer and cost estimator of the electrical, electronics, and networking projects.
- Designing electrical and communication solutions for a wide range of foundations and companies.
- importing, installation and operations to consistently meet rigorous customer requirements.

01/2014 – 08/2014 **Technical Support Engineer (night shift),** Hadara ISP Company

- Responded to technical support needs of customers regarding internet problems.
- Provided base level IT support to non-technical personnel within the business.
- Installed software, modified and repaired hardware and resolved technical issues.
- Identified and solved technical issues with a variety of diagnostic tools.
- Built and provided basic end-user troubleshooting and desktop support on Windows, Linux and Mac systems.
- Provided on-call support for critical issues.

01/2013 – 05/2013 **Maintenance engineer of electrical equipment,** Al-jebrini company for dairy and food products

- Maintained and repaired boilers, chillers, air handlers, heating and cooling systems.
- Designed, installed and maintained the company's telephony and internet network.
- Applying ISO 9001:2000 TQM system by producing and managing the required department documents.

WORK EXPERIENCE (ACADEMIC WORK)

09/2013 – 12/2016

Works as Trainer and instructor for the following courses:

- Trainer at SABIC Summer program (2016).
- Trainer at ARAMCO gifted program (2016).
- Instructor for ISO 9001: TQM and health & safety courses at King Abdu-Aziz Medical City, Riyadh (2015).
- Instructor for Electric Circuits, Electronics, Renewable energy, Electromagnetics, Telecommunications, Digital communications, Digital signal processing and Transmission lines courses at PPU and KFUPM.
- Trainer for Android Programming course at Engineers association, Palestine.
- Power system Analysis course at Electricity Company, Palestine
- Did a voluntary supervision work at a lab for C++ programming course at PPU.

TRAINING AND CERTIFICATIONS

09/2013 – 12/2016

- Cisco Certification Network Associate (CCNA).
- Lab view Program.
- MS Project Program.
- Mobile Maintenance course.
- Training course in Linux operating system.
- Android and Java programming language course at Lacasa Training center.
- 90 Hours concentrated training program at Jawwal company.
- Youth Entrepreneurship Development Program – PPU: Leadership, Business Eng, Language, Job Search, CV writing & Interview Skills ,Time management, Labor Law, Presentation skills and introduction to Entrepreneurship.
- 90 Hours concentrated training program at Paltel Company.

Cisco Academy , Palestine and Jordan (02/2014 – 04/2014):

- SMB Specialization for Engineers (Cisco 700-501 Version 5.1) course and exam.
- SMB Specialization for Account Managers (Version: 4.3 Cisco 700-505) course and exam.
- Cisco Sales Essentials (CSE), by Fast Lane academy (UAE), in Cisco center – Jordan.

HP Learning Center, Palestine (02/2014 – 04/2014):

- HP2-B110 Selling HP Imaging and Printing course and exam.
- HP2-B91 HP Imaging and Printing Supplies - Sales course and exam.
- HP2-B109 Selling HP Printing Personal system course and Exam.
- HP2-H25 Selling HP Personal Systems course and exam

QUALIFICATIONS

- Strong interpersonal skills and aptitude to work under pressure with people at many different levels or groups.
- Ability to perform required computerized tasks to include any combination of word processing, e-mail, internet, or web-based applications.
- Excellent and effective oral and written communication skills and abilities with all levels of the organization.
- Ability to develop and maintain effective working relationships with internal and external customers at all levels of the organization.

COMPUTER SKILLS

MATLAB/ ETAP / Arduino/NetBeans JAVA IDE / Eclipse Java / HP product Bulletin / Packet Tracer / Basic Graphical web design / Photoshop / Switchmax / Microsoft Windows / Microsoft Office package / Bisan Accounting Program/ JMAG FEM software/C++/ Android programming/ 8085Assembly/ PIC Microcontroller.